

REVIEW ARTICLE



Cite this: *Chem. Soc. Rev.*, 2018, 47, 8804

A critical review of cathodes for rechargeable Mg batteries

Minglei Mao,^{ab} Tao Gao,^{*a} Singyuk Hou^a and Chunsheng Wang^{ID} ^{*a}

Benefiting from a higher volumetric capacity (3833 mA h cm⁻³ for Mg vs. 2046 mA h cm⁻³ for Li) and dendrite-free Mg metal anode, reversible Mg batteries (RMBs) are a promising chemistry for applications beyond Li ion batteries. However, RMBs are still severely restricted by the absence of high performance cathodes for any practical application. In this review, we provide a critical and rigorous review of Mg battery cathode materials, mainly reported since 2013, focusing on the impact of structure and composition on magnesiation kinetics. We discuss cathode materials, including intercalation compounds, conversion materials (O₂, S, organic compounds), water co-intercalation cathodes (V₂O₅, MnO₂ etc.), as well as hybrid systems using Mg metal anode. Among them, intercalation cathodes are further categorized by 3D (Chevrel phase, spinel structure etc.), 2D (layered structure), and 1D materials (polyanion: phosphate and silicate), according to the diffusion pathway of Mg²⁺ in the framework. Instead of discussing every published work in detail, this review selects the most representative works and highlights the merits and challenges of each class of cathodes. Advances in theoretical analysis are also reviewed and compared with experimental results. This critical review will provide comprehensive knowledge of Mg cathodes and guidelines for exploring new cathodes for rechargeable magnesium batteries.

Received 21st June 2018

DOI: 10.1039/c8cs00319j

rsc.li/chem-soc-rev

1. Introduction

Since their invention in 1991, Li-ion batteries (LIBs) have gradually become the dominant mobile power source for various applications, especially consumer electronics. With over two

decades of innovation and engineering in materials and cell design, the energy density of LIBs has reached 240 W h kg⁻¹ and 670 W h L⁻¹ at the cell level.^{1,2} However, a ceiling in capacity and energy density is expected when LIBs approach the theoretical limits of intercalation chemistry.¹⁻³ Rechargeable metal batteries, which pair metal anodes with various cathode materials, offer great promise for further improving battery energy density because metal anodes provide much higher capacity and lower reduction potential than intercalation anodes (Fig. 1a). Among all metal anodes, the high capacity

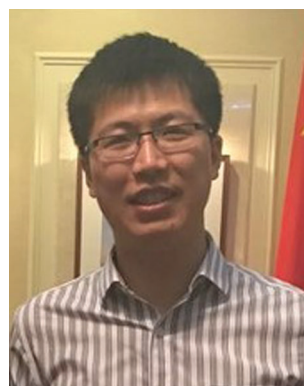
^a Department of Chemical and Biomolecular Engineering, University of Maryland, College Park, Maryland 20742, USA. E-mail: taogao@umd.edu, cswang@umd.edu

^b College of Chemistry and Chemical Engineering, Hunan University, Changsha 410082, China



Minglei Mao

Minglei Mao is currently a PhD candidate at the College of Chemistry and Chemical Engineering, Hunan University. He received his bachelor's degree from the College of Materials Science and Engineering, Hunan University. His research focuses on the development of cathode materials for multivalent metal batteries.



Tao Gao

Dr Tao Gao is currently a post-doctoral research associate at the Chemical Engineering Department, Massachusetts Institute of Technology. He received his bachelor's degree in Automotive Engineering and MS degree in Mechanical Engineering both from Tsinghua University, and PhD degree in Chemical Engineering from the University of Maryland. His research interest is chemistry and system innovation for next-generation batteries and electro-chemical methods.

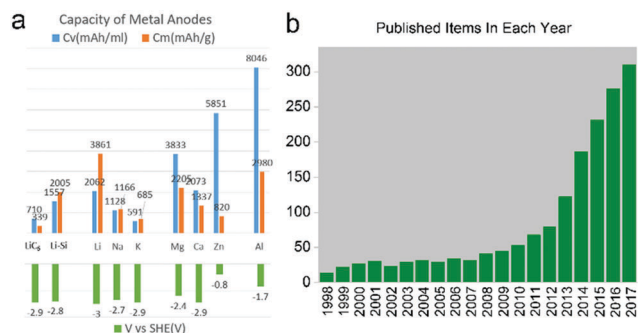


Fig. 1 (a) Capacity and redox potential of various metal anodes; (b) number of publications in the past two decades on the topic of "magnesium batteries".

(especially volumetric capacity of $3833 \text{ mA h cm}^{-3}$ for Mg vs. $2046 \text{ mA h cm}^{-3}$ for Li), low reduction potential (-2.4 V vs. SHE) and most importantly, dendrite-free deposition with 100% coulombic efficiency in some electrolytes make Mg metal an ideal anode.⁴ For this reason, there has been a growing interest in developing rechargeable Mg batteries in the past decade, especially after 2013 (Fig. 1b).

Due to its bivalent nature, the diffusion of Mg^{2+} in solid state cathode materials is much more sluggish than monovalent cations like Li^+ , which leads to large voltage hysteresis and low magnesiation degree for most materials.^{5–7} For this reason, finding cathode materials with acceptable kinetics has become the major challenge for the development of rechargeable Mg batteries. In this review, we will survey efforts in this field, especially those made after 2013, with a special emphasis on the influence of structure and composition on magnesiation kinetics.

This review is organized as follows: major attention will be focused on intercalation materials, followed by conversion

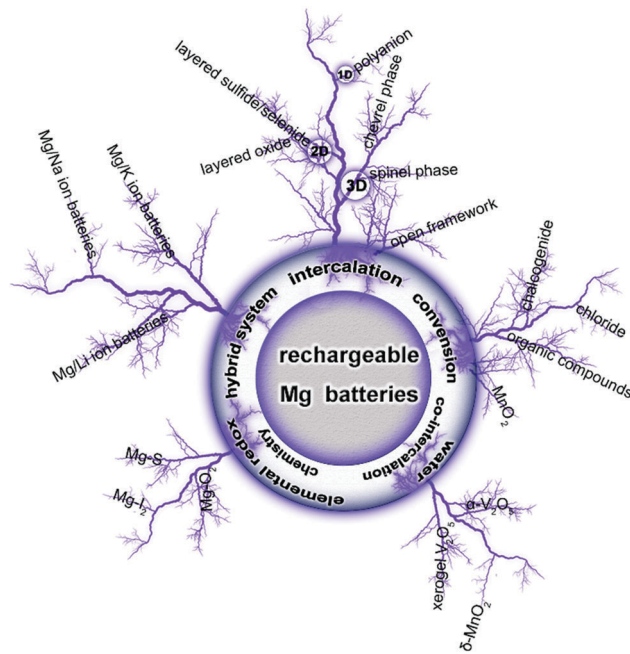


Fig. 2 An overview of cathodes for rechargeable Mg batteries.

materials. Elemental redox chemistries will be discussed in some detail due to their unique advantages of either high capacity or fast kinetics, while promising organic cathode materials, water co-intercalation cathode materials and hybrid battery systems are also briefly reviewed (Fig. 2). We will not elaborate on every individual cathode material, but emphasize the most representative cathodes. The theoretical and experimental results will be compared to highlight the merits and challenges of each class of cathode materials. We hope this review can provide insights on the frontier of this emerging but not fully exploited field.



Singyuk Hou

Singyuk Hou is a graduate student in the Department of Chemical and Biomolecular Engineering, University of Maryland. She received her bachelor's degree (2012) in Chemistry from Wuhan University, China, and MS degree (2015) in Chemistry from University of Massachusetts, Amherst. Her research interests include magnesium and lithium metal battery and transport kinetics in electrodes.



Chunsheng Wang

Prof. Chunsheng Wang is a full professor at the University of Maryland College Park (UMCP) and a co-founder and Director of the Centre for Research in Extreme Batteries (a joint battery center of the US Army Research Lab and University of Maryland). He was educated in materials science and trained in electrochemistry, and obtained his PhD degree from Zhejiang University. His work has been cited more than 11 500 times, with an H-index of

57 (ISI). His work on lithium batteries has been featured in NASA Tech Brief, EFR/DoE newsletter, C&EN etc. Dr Wang is the recipient of the A. James Clark School of Engineering Junior Faculty Outstanding Research Award in the University of Maryland in 2013, and he is the winner of UMD's Invention of the Year for 2015.

2. Intercalation

Intercalation compounds are the only commercialized cathode materials for rechargeable LIBs because the topotactic intercalation reaction maintains their structure during discharge/charge, guaranteeing good cycling stability and fast Li-ion diffusion.^{2,8,9} These compounds are also the most investigated for rechargeable magnesium batteries (RMBs).

The kinetics of Mg intercalation are intrinsically dependent on the ion mobility in these materials. In general, ion mobility is mainly determined by three structural factors: (1) connectivity between sites; (2) sizes of the diffusion channel/cavity and intercalant; (3) and interaction strength between the intercalant and host structure. The site connectivity divides cathode materials into 3D, 2D or 1D intercalation topology, which in turn affects the diffusion behavior of a material dramatically, as in principle, a well-distributed diffusion network should facilitate mobility by providing improved tolerance towards defects and changes in lattice parameters.^{10,11} Moreover, the channel size should be large enough to accommodate the intercalant. Finally, high mobility is facilitated by weak interaction between the intercalant and host anion lattice.

Ab initio quantum calculation also confirms that multivalent cation diffusion is firstly dependent on structure,¹² which determines the diffusion pathway, then on its chemistry, which determines the interactions between the intercalant and the host anion lattice.^{7,13} In different structures, the coordination preference of the multivalent cation dictates the energy level change during migration along the possible diffusion pathways, so that structures where the intercalants occupy the non-preferred coordination can reduce the migration energy barrier to ~ 525 – 650 meV, a value necessary for acceptable migration kinetics at room temperature.

In the section below, we will discuss how the structure affects the mobility and intercalation kinetics of Mg^{2+} based

on current experimental and theoretical understanding, especially in spinel, layered, and olivine cathodes. We will expand our discussion starting from structures with 3D diffusion channels (Chevrel phase, spinel), and then structures with 2D diffusion channels (layered structure), and finally, to structures with the 1D diffusion channel (polyanion compounds).

2.1 Chevrel phase

Chevrel phase (CP) (Mo_6S_8) is the first intercalation cathode that shows reversible Mg storage capability.^{14–17} It has a unique structure where six Mo atoms reside on the faces of a cube, forming an octahedron (Mo_6), and eight S anions (S_8) occupying the corners of the cube (Fig. 3a).^{18–20} Therefore, its structure possesses a quasi-simple-cubic packing of the Mo_6S_8 superanions, in which 3a and 9b sites form 3D channels that are available for Mg^{2+} transport.¹⁹ The unique metallic electronic structure of CP allows the easy accommodation of electrons because within Mo_6 , the electronic bonding is non-directional and orbitals are highly delocalized. The neutralizing electrons do not reside entirely (nor predominantly) on the Mo_6 clusters, but instead on the anions (S_8 clusters). The charge carried by Mg^{2+} is mostly balanced by the S atoms, resulting in a screening cloud that can effectively shield its $2+$ charge.²¹ In short, the highly delocalized orbitals and a screening cloud contribute to realizing the fast diffusion of Mg^{2+} at room temperature.

Generally, a migration barrier of ~ 525 meV corresponds to ionic diffusivity of $\sim 10^{-12} \text{ cm}^2 \text{ s}^{-1}$ at room temperature, representing the low limit for reasonable charge and discharge time (~ 2 h in micron-size active particles). An increase/decrease of 60 meV in the migration energy corresponds to an order of magnitude decrease/increase in the diffusion. Since diffusion time scales to the square of length, larger barriers can be tolerated with smaller particle size: every order of magnitude

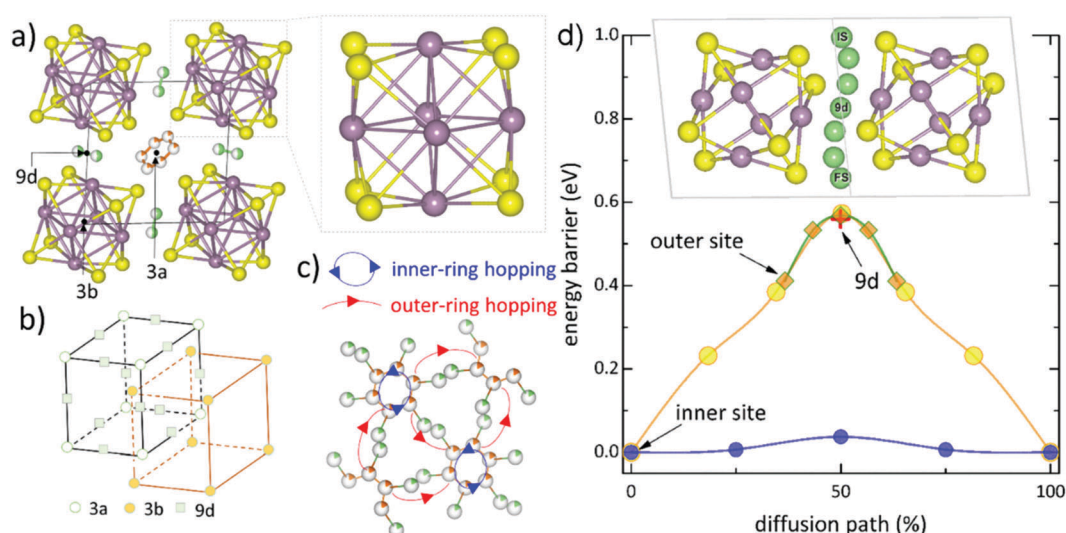


Fig. 3 Crystalline structure and sublattices in Chevrel phase Mo_6S_8 . (a) Mo_6S_8 superanion and positions of highly symmetric 3a, 3b, and 9d sites (viewed along the [211] direction). (b) Sublattice of 3a and 3b sites. (c) Outer-ring and inner-ring hopping between partially occupied inner and outer sites. (d) NEB path for the hopping in Chevrel phase Mo_6S_8 at dilute Mg concentrations. Reproduced from ref. 18 with permission from American Chemical Society, Copyright 2017.

in size reduction allows for two orders of magnitude smaller diffusion constant.¹³ Meanwhile, an increase in temperature reduces the diffusion barrier.^{22–24} Based on nudged elastic band (NEB) calculation, the inner-ring and outer-ring diffusion energy barriers of CP are estimated to be 40 meV and 570 meV, respectively, at dilute Mg concentration (Fig. 3d),¹⁸ which explains the fast diffusion of Mg in CP.

Besides fast Mg^{2+} diffusion, the special structure of CP also facilitates charge transfer at the interface by aiding the desolvation process.²⁵ In a typical Mg electrolyte based on transmetalation reaction between a Grignard reagent and a Lewis acid like AlCl_3 , Mg exists in the electrolyte in the form of a complex cation, *e.g.* Mg_2Cl_3^+ . The intercalation of Mg cation requires first peeling Mg^{2+} from the complex cation. Mo atoms on the CP surface act as a catalyst to reduce the required energy from 3000 meV to 200 meV, which facilitates the breaking of Mg–Cl bond. Once Mg is intercalated, it leaves the counter ion (Cl^-) on the surface, bound to Mo (Fig. 4).²⁵ The chlorinated surface continues to interact with incoming MgCl^+ species and form the neutral MgCl_2 unit, which may be released from these surface adsorbates to reopen Mo sites on the surface and permit continuous Mg–Cl bond breaking.

Benefiting from the high mobility of Mg^{2+} and fast interfacial charge transfer, Mo_6S_8 has been the most successful cathode material at room temperature to date, exhibiting excellent intercalation kinetics and reversibility with a capacity of 120 mA h g^{-1} at 1.2 V.⁴

As mentioned, reducing particle size will result in shorter Mg^{2+} diffusion length, thus improving the intercalation kinetics. To investigate this, the electrochemical performance of nanosized and microsized Mo_6S_8 was compared.²⁶ During the first discharge process, the overpotential for nanoparticles to initiate the first Mg^{2+} intercalation was noticeably lower than for microparticles. During the charge, more Mg^{2+} ions were extracted, and the trapping effect for nanoparticles was reduced. In addition, the kinetics of the stabilized electrochemical reaction for nanoparticles was better.

A mathematical model was developed to investigate the performance limiting factors of Mg/ Mo_6S_8 battery systems.²⁷

Limitation analysis indicates that the solid diffusion and kinetics in the higher voltage plateau limit the capacity and increase the overpotential in the thin ($20 \mu\text{m}$) electrodes. The polarization loss on charge is higher than that on discharge because of the differences in the kinetics and solid diffusion between the two reactions of the Chevrel phase. Also, the model reveals that the performance of the cells with practical electrode thickness ($80 \mu\text{m}$) would be subject to electrolyte-phase limitations.

In short, the low voltage and capacity of Mo_6S_8 remain a major limitation, encouraging extensive efforts on other high voltage or capacity intercalation materials. Among them, spinel structures have received particular attention.

2.2 Spinel: from oxide to sulfide

In the close-packed oxygen (or sulfur) structures (face-centered cubic fcc for spinel and layered, and hexagonal close-packed hcp for olivine), the diffusion path for Mg alternates through tetrahedral and octahedral sites along zigzag-shaped paths, leading to diffusion topologies that are either tet \rightarrow oct \rightarrow tet (Fig. 5a) or oct \rightarrow tet \rightarrow oct (Fig. 5b) (tri-vacancy hops), depending on which site is stable.¹² In a normal spinel, the intercalating Mg^{2+} initially resides in the stable tetrahedral site (with energy E_s), then migrates through a three-coordinated oxygen face (with energy E_a) shared with the adjacent intermediate octahedral site (with energy E_i), and finally follows a symmetric path to the next equivalent stable site (Fig. 5a). In the layered and olivine structures, diffusion proceeds in a similar fashion but between stable octahedral sites through an intermediate tetrahedral site (Fig. 5b). Spinel compounds belong to space group $Fd\bar{3}m$ with the general formula MgT_2X_4 . The anion X can be O, S, or Se. The cation T is octahedrally coordinated by X, and these edge-sharing octahedra extend in space and create 3D diffusion channels (Fig. 5a and 6).¹² The Mg diffusion energy barriers in spinel structures with different transitional metals ($T = \text{Ti, V, Cr, Mn, Fe, Co, Ni}$) were calculated and compared.¹³ Results show that the transition metal chemistry does not significantly affect the Mg^{2+} diffusion

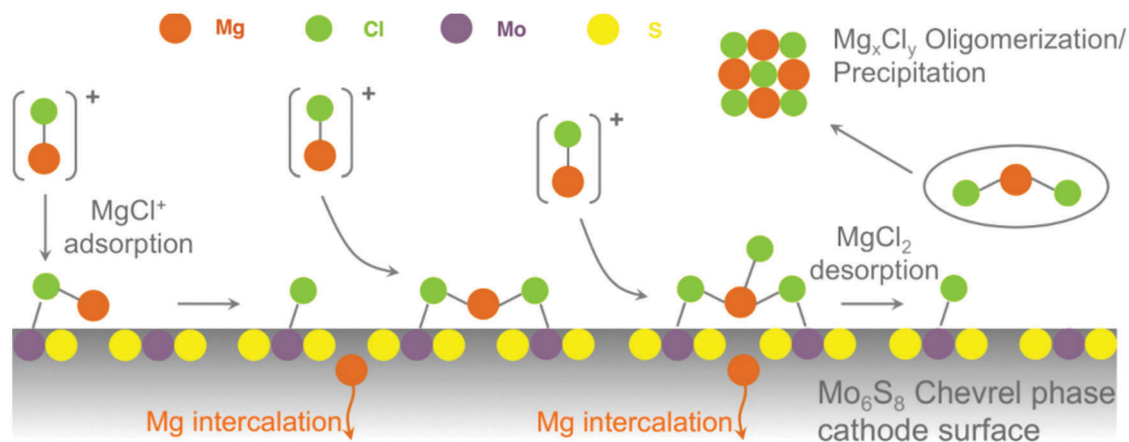


Fig. 4 Mg desolvation and absorption in Mo_6S_8 from Cl^- -containing electrolyte. Reproduced from ref. 25 with permission from American Chemical Society, Copyright 2015.

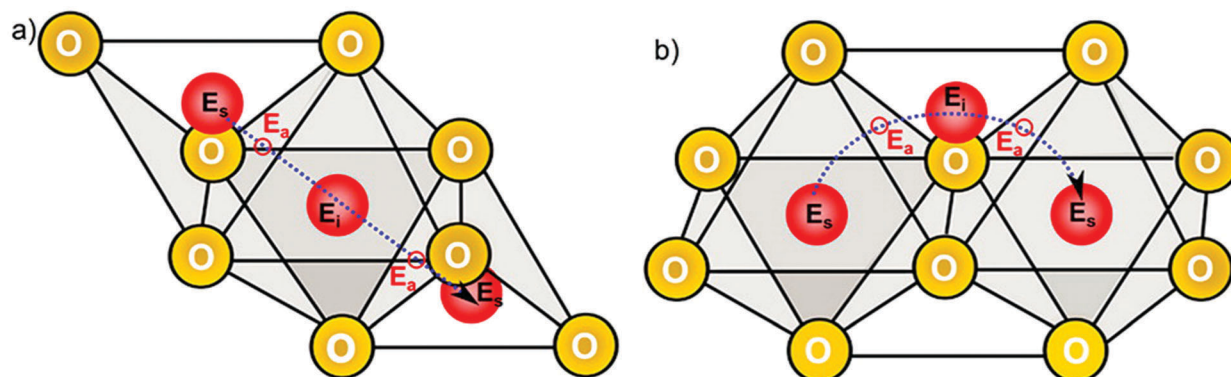


Fig. 5 Low-energy ion migration paths in close-packed oxides adopt either (a) tet → oct → tet or (b) oct → tet → oct diffusion topologies: stable insertion sites (E_s), active sites (E_a), and intermediate site (E_i). Reproduced from ref. 12 with permission from American Chemical Society, Copyright 2015.

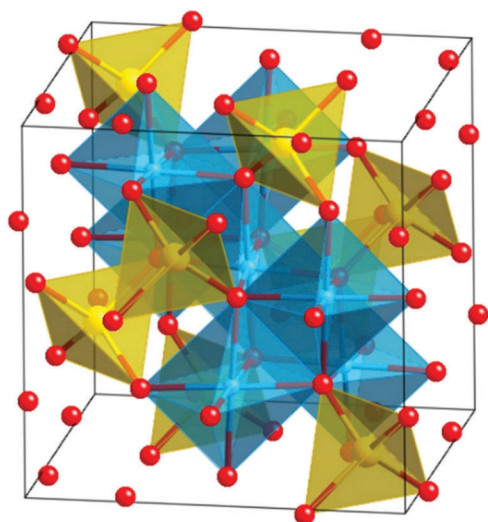


Fig. 6 Crystal structure of spinel MgT_2X_4 . The Mg atoms sit within the yellow tetrahedral, and the T atoms sit within the blue octahedral. The T atoms can be Ti, V, Cr, Mn, Fe, Co, and Ni, and the anion X can be O, S, or Se.

barriers, which all lie within ~ 600 to 800 meV in the empty lattice limit, higher than the ~ 525 meV threshold. Therefore, Mg^{2+} intercalation into those spinel oxides is not likely unless the temperature is elevated and/or nanosized particles are used. Despite Cr_2O_4 , Ni_2O_4 , and Co_2O_4 having slightly smaller diffusion barriers, spinel Mn_2O_4 (Fig. 7a) is considered a better spinel oxide cathode when thermodynamic properties are also considered, since it has a high voltage and volumetric capacity and acceptable volume change (less than 15%), and more importantly, both its charged and discharged states are thermodynamically stable.¹³

Based on the calculated results, various sizes and morphologies of spinel Mn_2O_4 (λ - MnO_2) with have been investigated in non-aqueous electrolytes.^{28–30} The nanoflakes of λ - MnO_2 (~ 50 nm in thickness and several hundred nanometers in diameter) show quite a low degree of Mg^{2+} intercalation (< 3 at% Mg per Mn_2O_4) and extremely high voltage hysteresis in $\text{Mg}(\text{TFSI})_2$ -diglyme or propylene carbonate (PC) electrolyte at

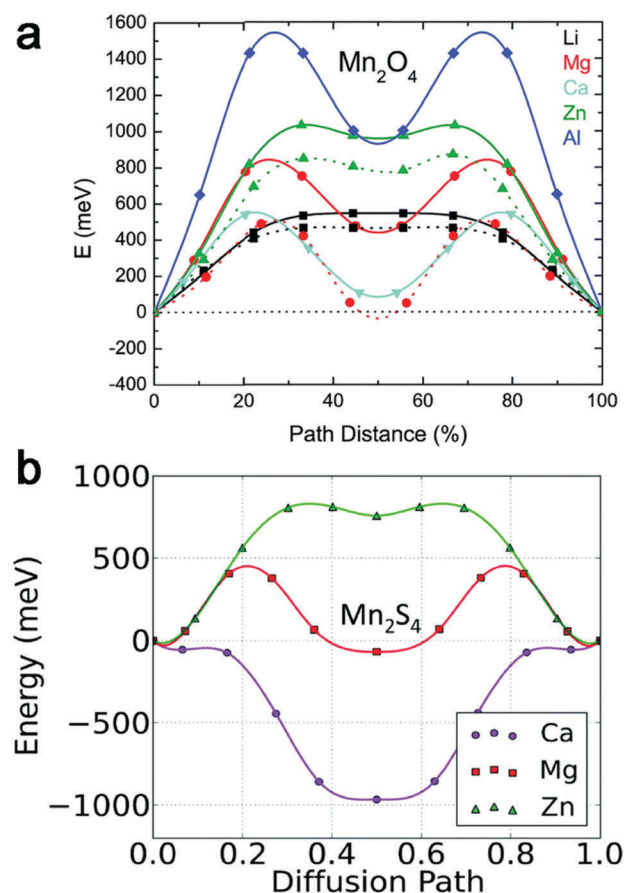


Fig. 7 Computed minimum energy paths for migration of different intercalants between the tetrahedral sites in (a) spinel Mn_2O_4 at the high vacancy limit (solid line) and dilute vacancy limit (dotted line). Reproduced from ref. 13 with permission from Royal Society of Chemistry, Copyright 2015. (b) Thiospinel Mn_2S_4 within the dilute limit of cation insertion. Reproduced from ref. 7 with permission from Royal Society of Chemistry, Copyright 2016.

RT (Fig. 8a and b).²⁹ Other than kinetic limitation, a phase transformation from cubic spinel Mn_2O_4 to tetragonal spinel MgMn_2O_4 during Mg^{2+} intercalation is also cited as a probable cause for the low magnesianation degree.²⁸ The tetragonal spinel

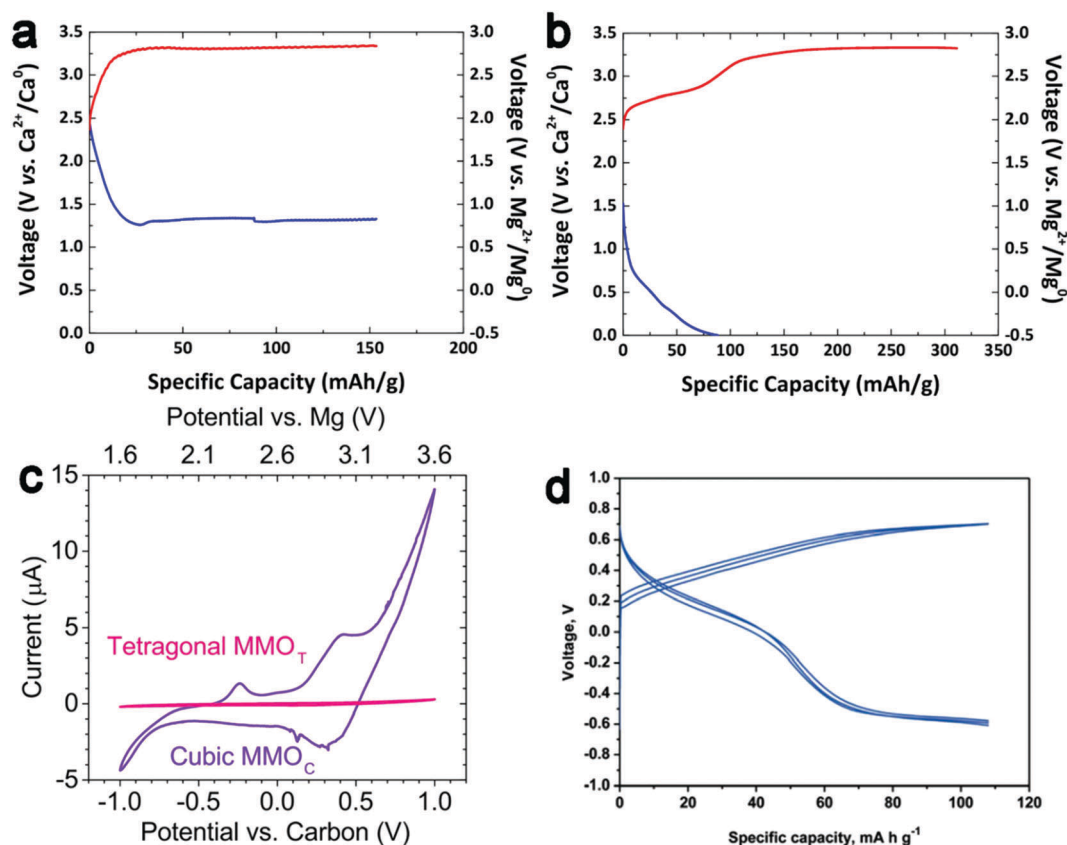


Fig. 8 (a and b) Voltage vs. capacity profiles for 3-electrode cells with Mn_2O_4 (made by delithiation of LiMn_2O_4) working electrodes, using 0.2 M $\text{Mg}(\text{TFSI})_2$ in diglyme (G2) and propylene carbonate (PC) as electrolytes, respectively. Reproduced from ref. 29 with permission from Wiley-VCH, Copyright 2015. (c) Cyclic voltammetry (CV) of tetragonal MgMn_2O_4 (pink) and cubic MgMn_2O_4 (purple) thin film. Reproduced from ref. 28 with permission from American Chemical Society, Copyright 2015. (d) Typical voltage–capacity curves of tetragonal MgMn_2O_4 for a magnesium-ion battery in 0.5 M $\text{Mg}(\text{ClO}_4)_2$ in EC:DEC. Reproduced from ref. 30 with permission from Royal Society of Chemistry, Copyright 2015.

structure, a partially inverted spinel with a majority of $\text{Mn}(\text{III})$ in the octahedral site as well as a fraction of $\text{Mn}(\text{IV})$ and $\text{Mn}(\text{II})$ in the octahedral and tetrahedral sites, respectively, is considered to block the Mg^{2+} intercalation. To demonstrate this, both phases were cycled in the same electrolyte, separately, and the cubic phase exhibited reversible Mg^{2+} electrochemical activity with charge capacity approaching 250 mA h g^{-1} (in theory: 270 mA h g^{-1}),²⁸ while no significant insertion behavior was observed for tetragonal phase (Fig. 8c), indicating that the phase stabilization of spinel Mn_2O_4 is critical to acquiring the reversible electrochemical activity. However, opposite results were obtained when tetragonal MgMn_2O_4 nanoparticles were employed with 0.5 M $\text{Mg}(\text{ClO}_4)_2$ in EC:DEC as the electrolyte, which delivered a reversible capacity of 120 mA h g^{-1} (Fig. 8d).³⁰ Such inconsistent results may be due to the different current densities and particle sizes in the experiments.^{28,30} Despite the low mobility of Mg^{2+} in spinel Mn_2O_4 ,^{13,28,30} reducing current density and particle size can potentially enable higher Mg storage in spinel Mn_2O_4 , and these experimental works seem to provide encouraging results to demonstrate this. Nevertheless, a more systematic experimental study is necessary to clear the confusion and confirm how phase transformation affects the capacity of spinel Mn_2O_4 .

Given the low mobility of Mg^{2+} in oxide spinel, sulfide spinels (thiospinel), which are expected to have higher Mg^{2+} mobility due to the moderate increase of diffusion channel size and less ionic interaction between Mg^{2+} and the host structure, were also investigated.^{7,31,32} Similar to oxide spinel, Mg^{2+} diffuse in the thiospinel along zigzag-shaped paths through a narrow, triangular aperture of three sulfur atoms (Fig. 5). Calculation of Mg^{2+} mobility in thiospinel with different transition metals (Ti, V, Cr, Mn, Fe, Co, Ni) shows that several thiospinel compounds exhibit reasonable Mg^{2+} mobility, including Mn_2S_4 (515 meV), Cr_2S_4 (567 meV), and Ti_2S_4 (615 meV) (Fig. 7b),⁷ which are slightly more than or close to the 525 meV threshold. Comparison between DFT calculations and experimental results shows that thiospinel TiS_2 have a $\sim 200 \text{ meV}$ reduction in migration barrier compared to spinel MnO_2 , which means ~ 4 order of magnitude improvement in diffusion, though still higher than Mo_6S_8 . Considering the thermodynamic stability, voltage, capacity, and migration activation energy, Cr_2S_4 , Ti_2S_4 , and Mn_2S_4 emerge as the top three cathode candidates amongst the 3d transition-metal thiospinel compounds.

To validate the theoretical prediction, thiospinel TiS_2 was synthesized and tested in APC electrolyte at 60°C , yielding an initial capacity of 200 mA h g^{-1} (corresponding to $\text{Mg}_{0.84}\text{Ti}_2\text{S}_4$)

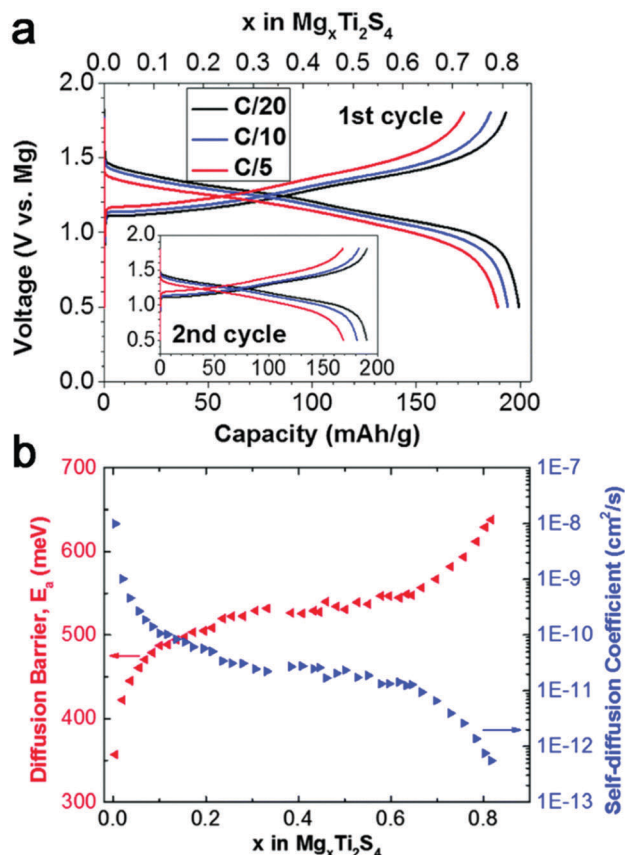


Fig. 9 Electrochemistry of C-Ti₂S₄ coin cells with an APC electrolyte and a Mg negative electrode at 60 °C. (a) Discharge and charge curves of the first and second (inset) cycles at various rates in APC/THF electrolyte. (b) Capacity and coulombic efficiency (CE) evolution at a C/10 rate in APC/G4 electrolyte (inset showing 99% CE). Reproduced from ref. 24 with permission from Royal Society of Chemistry, Copyright 2016.

with an average potential of 1.2 V at C/20 (Fig. 9a).²⁴ In addition, it exhibits excellent rate capabilities, and the small volume change during cycling promotes good capacity retention. Fourier mapping on the electrochemical magnesiation of 0.8 Mg demonstrated that ~30% of Mg²⁺ occupied octahedral 16c sites and ~20% tetrahedral 8a sites, corresponding to the composition of Mg[oct]_{0.59}Mg[tet]_{0.189}Cu_{0.1}Ti₂S₄. In addition, Mg²⁺ only occupied octahedral sites in partially discharged Ti₂S₄ (0.4 and 0.6 Mg/Ti₂S₄). Therefore, a stepwise Mg²⁺ intercalation mechanism is proposed: octahedral 16c sites are filled first, followed by population of tetrahedral 8a sites, which is driven by subtle thermodynamic and kinetic factors. The experimental results partially confirm simulations; however, the tri-vacancy hop mechanism employed in simulations should be improved because it shows some inconsistency with experimental results (Fig. 9b).

Compared with the Chevrel phase (Mo₆S₈ or Mo₆Se₈), spinel compounds holds the potential to obtain high voltage and capacity, and thus high energy density, as cathodes for RBMs. However, Mg²⁺ can hardly intercalate spinel compounds reversibly at room temperature, which is their biggest obstacle. Several methods have been used to remit the problem, such as elevating the operating temperature, reducing the particle

sizes, and increasing the volume of the spinel crystal structure.³³ In addition, Mg desolvation process followed by surface diffusion greatly affects intercalation overpotential. To our best knowledge, there is no study on the Mg desolvation process at the surface of spinel, which needs to be clarified in any future study concerning the kinetics of spinel. For oxide and sulfide spinel, the gravimetric capacities of sulfur spinel compounds are approximately 30% lower than their oxide counterparts due to the added mass of the S ion, in addition to the lower voltage. However, it is possible that sulfur-based compounds, with their improved intrinsic bulk cation mobility and less requirement (presumably) for electronically conductive coatings, could achieve a higher fraction of their theoretical energy density (~400 W h kg⁻¹), and thus higher practical energy densities.⁷

2.3 Layered sulfide/selenide

As a typical layered material, layered TiS₂ can serve as a model to investigate the thermodynamics and kinetics associated with Mg intercalation into layered structures. Layered TiS₂ consists of stacking sequences of TiS₂ slabs, each of which is composed of a stacking of close-packed two-dimensional triangular lattices of sulfur. Ti atoms occupy octahedrally coordinated interstitial sites between sulfur planes (Fig. 10a).^{22,33} Mg²⁺ ions

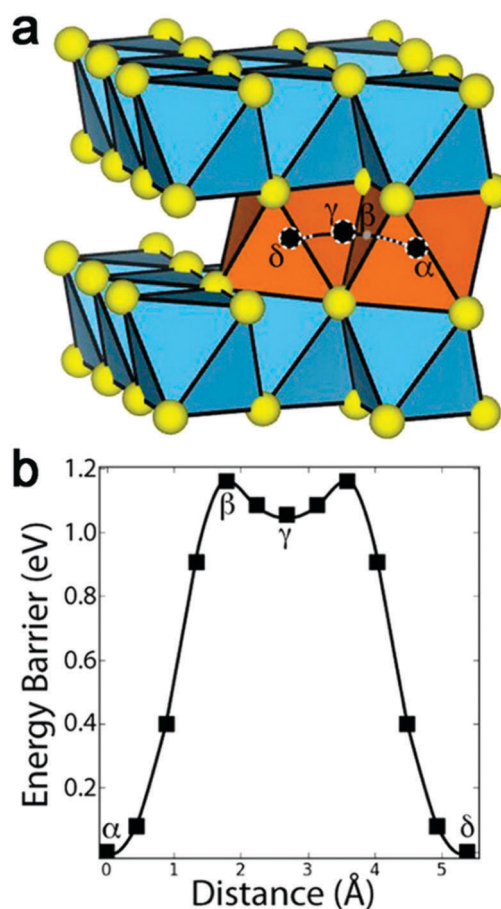


Fig. 10 (a) Crystal structure and pathway and (b) migration barrier in layered TiS₂. Reproduced from ref. 33 with permission from American Chemical Society, Copyright 2015.

diffuse between stable octahedral sites through intermediate tetrahedral sites, where the energy exhibits a local minimum before moving to the adjacent octahedral sites. The migration barriers at the dilute Mg concentrations are calculated, and the maximum barrier (1160 meV) occurs when Mg^{2+} passes through a triangle face created by three of the sulfur atoms of the MgS_6 octahedron (point β in Fig. 10a and b).³³ The shortest Mg–S distances along the migration path lie at the center of the triangular face separating the tetrahedral and octahedral sites, and the Ti–S bond length determines the size of diffusion channels.

The electrochemical performance of layered TiS_2 was measured in APC/THF at 60 °C.²² An initial discharge capacity of 270 mA h g^{-1} (0.56 Mg/TiS_2) at a C/20 rate (inset in Fig. 11a) was obtained. Three voltage plateaus are observed, and the corresponding phase transformation is confirmed by *in situ* XRD results (Fig. 11b and c). Both the experimental and calculated results demonstrate that Mg^{2+} can intercalate reversibly into layered TiS_2 . However, the low mobility renders its performance at RT unsatisfactory. Other than raising the temperature and reducing the particle size, substituting Se for S in layered TiS_2 could be an effective way to increase the mobility of Mg^{2+} .^{34–37}

Despite the absence of quantitative studies on how Se substitution affects the thermodynamics and kinetics of Mg^{2+} intercalation into layered TiS_2 , qualitative analysis shows that the substitution will enlarge the channel for Mg^{2+} diffusion (owing to the longer Ti–Se bond) and reduce the interaction between Mg^{2+} and the host lattice, especially at the center of the triangle (point β in Fig. 10), where Mg^{2+} encounters the maximum energy barriers.³⁴ For this reason, layered TiSe_2 holds more possibility for practical use at RT, especially considering its much higher volumetric capacity ($\sim 551 \text{ mA h cm}^{-3}$) than that of TiS_2 ($\sim 370 \text{ mA h cm}^{-3}$). TiSe_2 ($\sim 10 \mu\text{m}$) was employed as cathode at 25 °C and showed a specific capacity of $\sim 108 \text{ mA h g}^{-1}$ in the first 50 cycles (Fig. 12a).³⁸ In contrast, TiS_2 can only achieve comparable capacity at 60 °C and with smaller particle sizes.²²

Above, we discussed how substituting S with Se affects the diffusion of Mg^{2+} in layered TiSe_2 , providing a reasonable explanation for the better kinetics of TiSe_2 than TiS_2 . However, this may not be the only reason that accounts for the improvement in kinetics, as some research points out that the electronic structure also plays an important role.^{39–43} In transition-metal chalcogenides, electronic delocalization happens in metal–ligand units through orbital mixing because of good energy and symmetry match, and the electronic wave function of transition-metal chalcogenide spreads on both constituent atoms.⁴⁴ The charge density of the introduced electrons distributes over metal–ligand units (Fig. 13a). In a system with weak orbital mixing because of poor energy and/or spatial overlap of orbitals, the electrons will be accommodated only in the transition metal orbitals (Fig. 13b). In the case of selenides, d–p orbital mixing is enhanced by high orbital overlap due to the large 4p-orbital size of Se compared with that of oxides or sulfides. Since the energy levels of valence atomic orbitals in TiSe_2 , the 3d-orbital of Ti, and the 4p-orbital of Se are close to

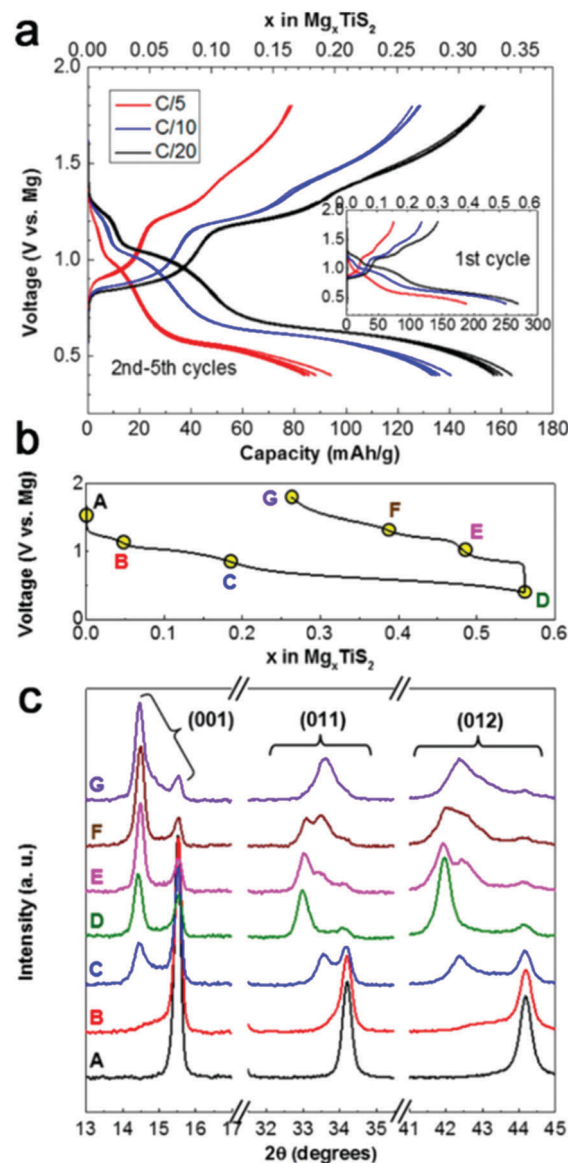


Fig. 11 (a) Discharge and charge profiles of layered TiS_2 . (b) Electrochemical discharge–charge profile at C/20 on the first cycle. (c) XRD profiles. Reproduced from ref. 22 with permission from American Chemical Society, Copyright 2016.

each other, the mixed electronic structure is expected around Fermi energy (Fig. 13c), which enables a better accommodation of electrons accompanying the intercalated Mg^{2+} , resulting in good electrochemical activity for Mg storage (Fig. 12a) even with micro-sized particles at RT.³⁸ Likewise, layered VSe_2 (Fig. 12b)³⁸ and WSe_2 ⁴⁵ show good electrochemical activity for Mg^{2+} intercalation at ambient temperature.

In view of many misunderstandings of the term orbital hybridization, it is necessary to elaborate it in this review. Orbital hybridization refers to mixing atomic orbitals into new hybrid orbitals within a single atomic site. The phenomenon of adjacent atomic orbitals with comparable energy from different atoms overlapping and forming a covalent bond or delocalized bond should be called orbital mixing, not orbital hybridization.

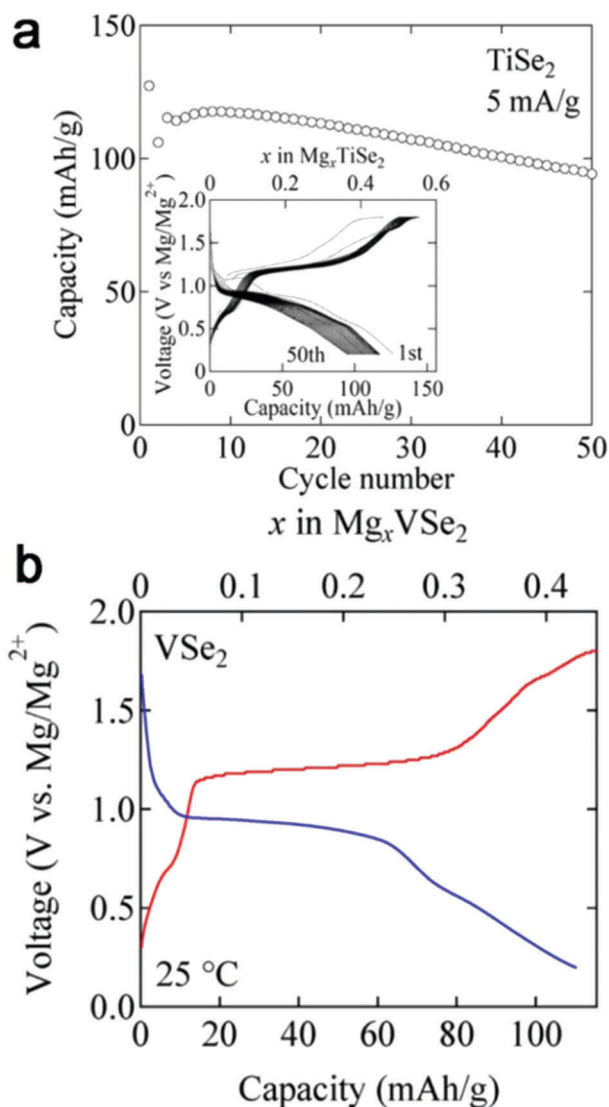


Fig. 12 (a) Cycle performance of RMBs with TiSe_2 for capacity measured at 25 °C. The inset shows the charge/discharge curves on each cycle. (b) The charge/discharge curve (on second cycle) with VSe_2 cathode measured at 25 °C. Reproduced from ref. 38 with permission from Springer Nature, Copyright 2015.

Orbital mixing is dictated by the energy match between neighbouring atoms' orbitals and their symmetry. The more closely the energy of adjacent atomic orbitals from different atoms match and the better spatial overlap they have, the more covalent the interaction is, and the electrons occupying the orbital are more delocalized between the two or more atoms.

The orbital mixing theory is further validated by the reversible Mg storage in titanium trisulfide (TiS_3).⁴⁶ The crystal structure of TiS_3 consists of chains of trigonal prismatic $[\text{TiS}_6]$ units sharing opposite faces along the b -axis (Fig. 14a).^{46–48} Neighbouring chains are connected laterally into slabs parallel to the (001) plane and separated by a van der Waals gap, which allows Mg^{2+} insertion into the space between chains. As the energy level of the S 3p orbital (−11.60 eV) is close to that of the Ti 3d orbital (−11.04 eV), the electronic structure is spread over

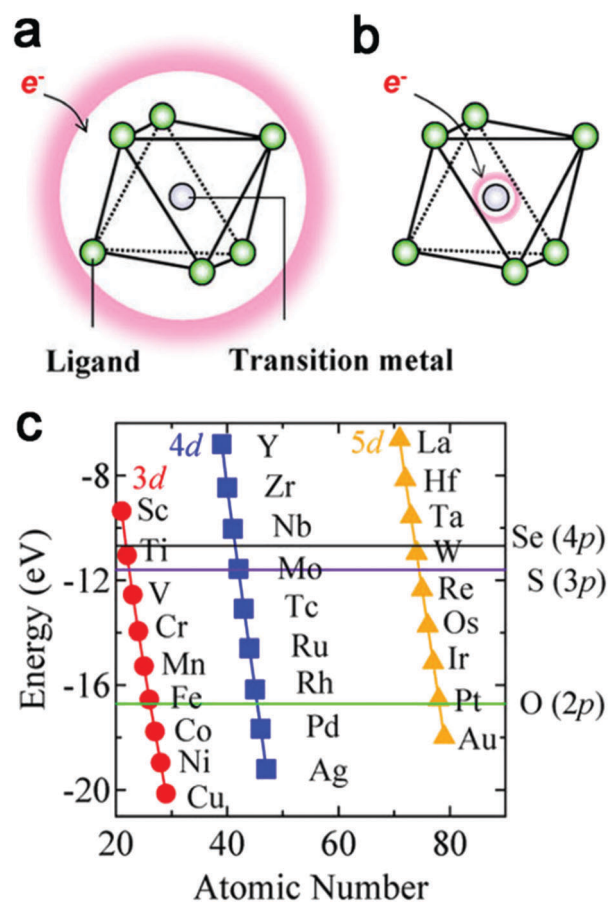


Fig. 13 Charge distribution in the electronic state with (a) strong d–p mixing and (b) weak d–p mixing. (c) Energy diagram of atomic orbitals. Reproduced from ref. 38 with permission from Springer Nature, Copyright 2015.

cluster-like $[\text{TiS}_3]$ units by d–p orbital mixing. In the electronic structure, electrons introduced by the Mg^{2+} insertion process are accommodated into a d–p orbital mixed electronic state, in which electron density is delocalized over both Ti and S atoms. In addition, the local electrostatic interaction between Mg^{2+} and the host lattice could be suppressed through the delocalization of electron density. Thus, micro-sized TiS_3 shows the first discharge capacity of 140 mA h g^{-1} at 10 mA g^{-1} and RT (Fig. 14b), corresponding to Mg concentration of $\text{Mg}_{0.37}\text{TiS}_3$, which is further confirmed by a low migration barrier of 292–698 meV calculated along the [010] direction (Fig. 14c and d).⁴⁹ This value is much lower than that in spinel and layered TiS_2 (615–1160 meV) and also the ~525 meV threshold.

Since d–p orbital mixing contributes to the good electrochemical performance of TiSe_2 and TiS_3 , further study based on the electronic structure could open a new way to design cathode materials for RMBs.

2.4 Layered vs. spinel: TiS_2

Based on calculated and experimental results,^{7,13,22,33} spinel and layered structures are compared systematically in this section using TiS_2 as an example. Mg^{2+} tends to occupy the octahedral

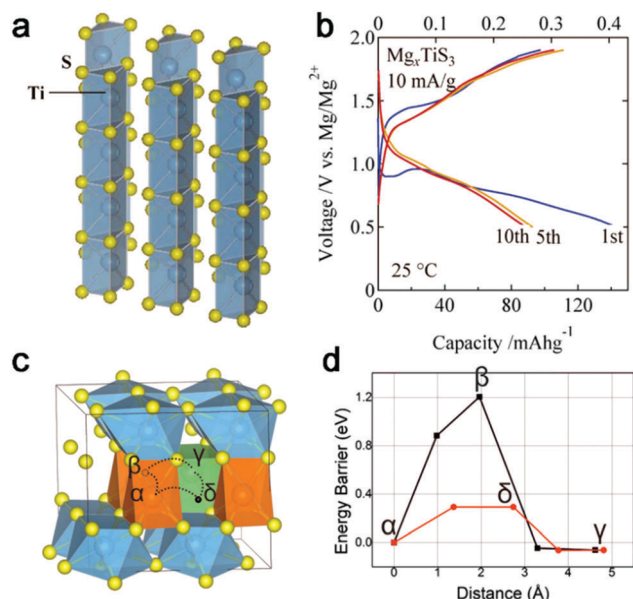


Fig. 14 (a) Crystal structure of TiS_3 . (b) Charge/discharge curve (on the 1st, 5th, and 10th cycles) of the Mg battery cell with TiS_3 measured at 25 °C. Reproduced from ref. 46 with permission from The Japan Society of Applied Physics, Copyright 2015. (c) Migration pathway and (d) diffusion energy barrier of Mg in $\text{Mg}_{0.375}\text{TiS}_3$. Reproduced from ref. 49 with permission from American Chemical Society, Copyright 2017.

sites in both layered and spinel TiS_2 , with diffusion mediated by hops between octahedral sites that pass through adjacent tetrahedral sites (Fig. 5b and 10a). The calculated voltage profile for layered Mg_xTiS_2 shows three plateaus (Fig. 15a), corresponding to three stable Mg-vacancy orderings: $\text{Mg}_{1/6}\text{TiS}_2$, $\text{Mg}_{1/3}\text{TiS}_2$, and $\text{Mg}_{1/2}\text{TiS}_2$, while the sloping regions at low and intermediate Mg concentration can be ascribed to solid solutions characterized by Mg-vacancy disorder.³³ In contrast, spinel Mg_xTiS_2 exhibits a sloping voltage profile (Fig. 15b) as x varies between 0 and 0.5 in Mg_xTiS_2 , which represents more of a solid solution across the entire composition range. As we have discussed before, both spinel and layered TiS_2 hold high diffusion barriers for Mg^{2+} .^{7,33} To improve the mobility of Mg^{2+} , an effective method is to increase the size of the diffusion pathway by increasing the c -lattice parameter or crystal volume. In layered $\text{Mg}_{1/32}\text{TiS}_2$, increasing the c -lattice parameter by 5% or 10% lowers mobility barriers to 900 and 550 meV (Fig. 15c), while in spinel $\text{Mg}_{1/32}\text{TiS}_2$, a 5% volume increase lowers the mobility barrier to 680 meV (Fig. 15d). The results indicate that both layered and spinel TiS_2 are sensitive to the size of octahedral and tetrahedral sites, and artificially increasing the distance between layers in layered TiS_2 and the crystal volume of spinel TiS_2 benefits Mg^{2+} mobility.

The interaction between the intercalants (the cation) and the host (the intercalation compound) can be understood by evaluating the degree of remixing between the transition metals

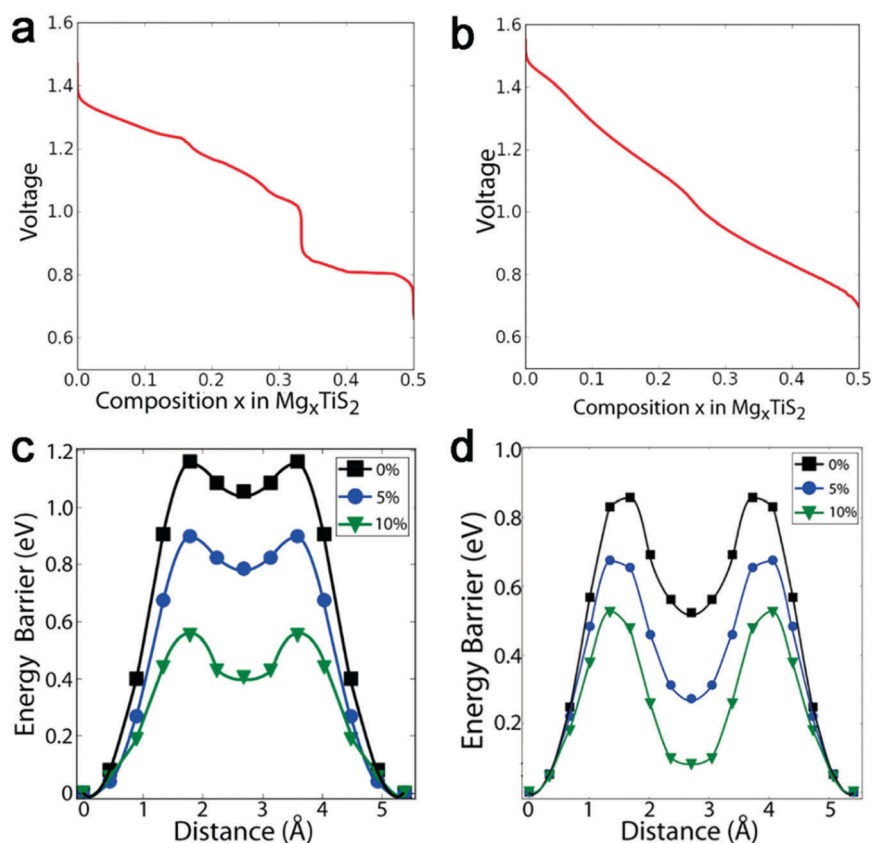


Fig. 15 Voltage curve for (a) spinel and (b) layered Mg_xTiS_2 calculated with Monte Carlo simulations at 300 K. Migration barriers in (c) spinel and (d) layered TiS_2 for different volume expansions. Reproduced from ref. 33 with permission from American Chemical Society, Copyright 2015.

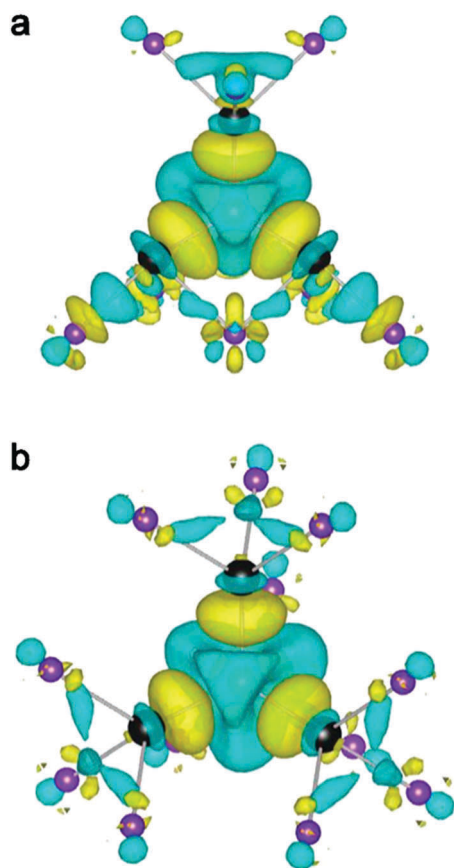


Fig. 16 Charge remixing upon insertion of Mg in the tetrahedral site of (a) layered and (b) spinel TiS_2 with identical S–S bond lengths. Areas of charge accumulation are shown in yellow, while depletion is shown in blue. Sulfur atoms are shown as large black spheres, Ti as small purple spheres, and Mg at the center as an orange sphere. Bonds are drawn in gray. Reproduced from ref. 33 with permission from American Chemical Society, Copyright 2015.

and anions of the host. Charge difference plots were compared for Mg insertion into tetrahedral sites of layered and spinel TiS_2 (Fig. 16),³³ in which the remixing in the spinel tetrahedral sites is more evenly distributed than that in the tetrahedral site of layered TiS_2 . In spinel, each S anion coordinating a tetrahedral Mg site mixes with three Ti (Fig. 16b). In layered TiS_2 , only one of the four S anions coordinating a tetrahedral Mg site mixes evenly with three Ti (the top sulfur atom in Fig. 16a), while the remaining three S mix primarily with only one Ti each and partially mix with two additional Ti that are “shared” by the other S anions. Such a higher coordination of the S sublattice with Ti is likely to distribute the remixing over more Ti–S bonds, accounting for much of the lower migration barrier in spinel compared to that in layered TiS_2 .³³

The migration barriers for Mg hops in layered and spinel TiS_2 correlate with the difference in energy between octahedral and tetrahedral site occupancy. Several factors contribute to the energy difference between tetrahedral and octahedral sites: the size of sites, the flexibility of coordinating ions, and the electrostatic energy. Also, more complex quantum mechanical effects exist, including the flexibility of adjacent ions to remix

as the positively charged cation migrates from one site to another. However, no unambiguous ways can disentangle the role of purely electrostatic interactions from the quantum mechanical interactions responsible for remixing.

The conclusion drawn in this charge remixing calculation is also in accordance with the aforementioned d–p mixing mechanism,^{38,46} in which high Mg migration mobility and low migration barrier are expected when the electronic structure of the transition metal (d orbital) overlaps more with the electronic structure of the anion (p orbital) so that charge can be better distributed over the Ti–S/Se bonds.

Summarizing the above discussions, several measures can be taken to improve the migration kinetics of Mg^{2+} in intercalation cathodes: (1) increasing temperature, which can improve the Mg^{2+} activity.^{22,23} (2) Downsizing the particles of cathodes, which will shorten the diffusion distance of Mg^{2+} in cathodes.³⁴ (3) Substituting O with S and Se. The substitution will reduce the ionicity of the hosts and enlarge the channel for Mg^{2+} diffusion, both of which weaken the interaction between Mg^{2+} and the host lattice.^{7,35,38} Besides, the substitution will decrease site energy difference along the diffusion pathway, contributing to Mg^{2+} hopping.⁵⁰ (4) Employing compounds with similar d–p orbital energy, which can contribute to the accommodation of charge brought by Mg^{2+} , according to the d–p mixing mechanism discussed above.^{33,38,46} (5) Using transition metal ions that readily shift by more than one valence state, such as Mo, as they are likely to be more flexible in remixing as Mg migrates through the crystal.

2.5 Layered oxides

In the last section, we discussed layered sulfides/selenides. Despite layered sulfides comprising a large group among inorganic compounds, TiS_2 stands out as a model system for our discussion because of extensive experimental, theoretical and computational studies. In this section, our discussion proceeds to layered oxides, also a very rich family of inorganic materials. Unfortunately, we could not find a similar representative example to focus on, so we will expand the discussion to several typical oxides.

Similar to layered sulfide, the weak van der Waals force between layers renders layered oxides presumably good intercalation compounds, and their higher voltage vs. sulfide makes them more attractive in terms of energy density.^{51–53} Besides, their structural flexibility, which can accommodate the expected severe structural deformations upon insertion of Mg^{2+} ,^{54–57} also makes layered transition metal oxides a promising cathode candidate for RMBs.

2.5.1 V_2O_5 . V_2O_5 has received the most attention for Mg batteries among all layered oxides.^{57–65} Its lattice is comprised of layers of alternating edge- and corner-sharing VO_5 pyramids (Fig. 17), with the intercalant atoms (yellow spheres) located between the layers.⁶⁵ The main difference between α and δ polymorphs lies in the different stacking of layers along a direction (perpendicular to the b – c plane; Fig. 17b). When intercalated into V_2O_5 , Mg atoms occupy the center of four VO_6 octahedrons running along the a -direction of the orthorhombic lattice. The calculation

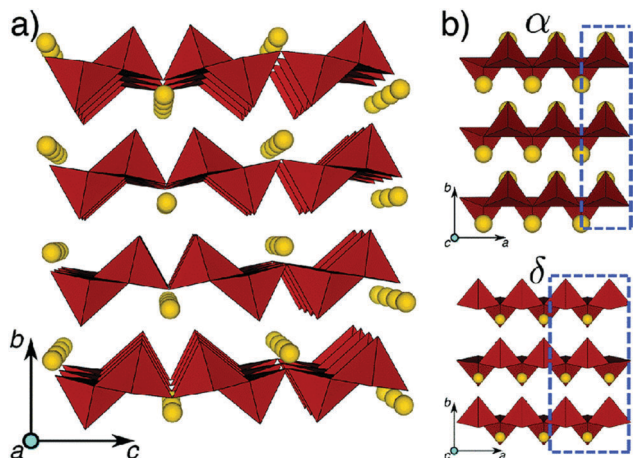


Fig. 17 (a) The V_2O_5 structure of both the α and δ polymorphs on the b - c plane, with the yellow spheres indicating the intercalant sites; (b) the α and δ polymorphs on the a - b plane. Reproduced from ref. 65 with permission from Royal Society of Chemistry, Copyright 2015.

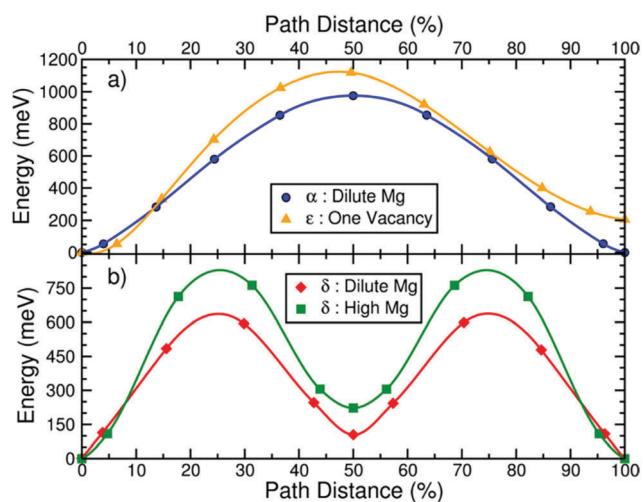


Fig. 18 Activation barriers for Mg diffusion in (a) α - V_2O_5 and (b) δ - V_2O_5 . Reproduced from ref. 61 with permission from American Chemical Society, Copyright 2015.

shows that the migration barriers in the δ phase (~ 600 – 760 meV) are much lower than those in the α phase (~ 975 – 1120 meV), with the respective migration energies adopting “valley” and “plateau” shapes, which can be attributed to the changes in the coordination environment of Mg along the diffusion path (Fig. 18).^{58,61} In the α phase, Mg migrates between adjacent 8-fold coordinated sites through a shared 3-fold coordinated site (activated state), a net $8 \rightarrow 3 \rightarrow 8$ coordination change, while in the δ phase, Mg migrates between adjacent 6-fold coordinated sites through two 3-fold coordinated sites separated by a metastable 5-fold coordinated “valley”, a net $6 \rightarrow 3 \rightarrow 5 \rightarrow 3 \rightarrow 6$ coordination change.⁶¹ Hence, for Mg^{2+} that prefers a lower coordination number, an α to δ transition upon Mg^{2+} insertion in V_2O_5 is likely.

In order to systematically evaluate the difference of α - and δ - V_2O_5 in Mg^{2+} insertion/extraction, the interlayer spacing,

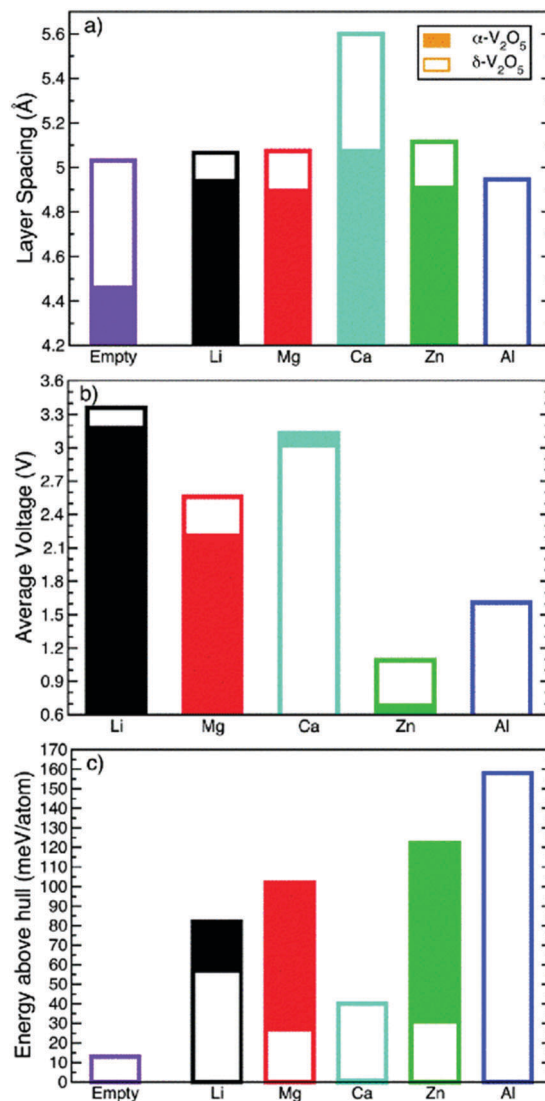


Fig. 19 (a) Layer spacing values for the empty and intercalated versions of AV_2O_5 ($A = Li, Mg, Ca, Zn$ and Al) for both α and δ polymorphs. (b) Calculated average voltage values for the intercalation of the different ions. (c) Energy above hull, which quantifies the stability of a structure, for the empty and intercalated versions of α and δ . Reproduced from ref. 65 with permission from Royal Society of Chemistry, Copyright 2015.

average voltage, and thermodynamic stability of α - and δ - V_2O_5 were calculated.⁶⁵ The interlayer spacing in α - and δ -polymorphs were calculated for empty V_2O_5 and intercalated MgV_2O_5 (Fig. 19a). At the same intercalant composition, the δ structures consistently have larger layer spacing than α (~ 3 – 5% larger). The change in the layer spacing is much smaller in δ (less than 2%) than α (9 – 14%). The higher layer spacing, plus the smaller coordination changes, contribute to the lower migration barriers of the δ phase. The average voltage of δ - V_2O_5 (2.56 V) is higher than that of α - V_2O_5 (2.21 V) (Fig. 19b). In the de-intercalated limit, α - V_2O_5 is thermodynamically stable, while δ phase is metastable at RT. In the intercalated state, δ phase is more stable than α (by 75 meV per atom) (Fig. 19c), aligning well with the preferred coordination environment of Mg^{2+} , and accordingly, the insertion

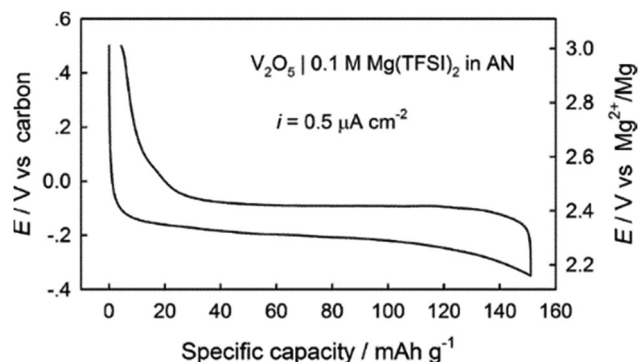


Fig. 20 Typical galvanostatic titration curve of a V_2O_5 thin-film electrode in 0.1 M Mg(TFSI)_2 in AN (current density = $0.5 \mu\text{A cm}^{-2}$). Reproduced from ref. 57 with permission from American Chemical Society, Copyright 2013.

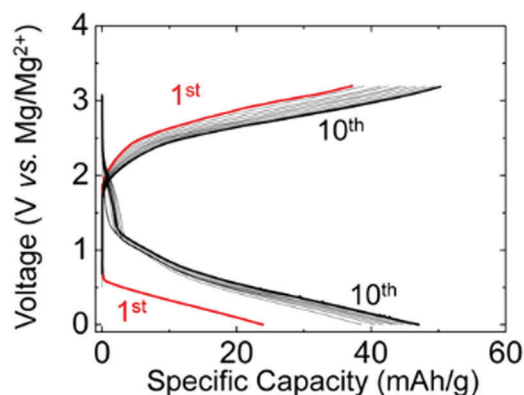


Fig. 22 Galvanostatic charge-discharge curves of $\text{V}_2\text{O}_5 \cdot n\text{H}_2\text{O}$ in 1.0 M Mg(TFSI)_2 /diglyme electrolyte at $20 \mu\text{A cm}^{-2}$. Reproduced from ref. 67 with permission from American Chemical Society, Copyright 2016.

voltage is higher for δ than α (Fig. 19b). Considering the lower energy barriers, larger layer spacing, higher average voltage, and moderate thermodynamic stability, $\delta\text{-V}_2\text{O}_5$ is a more promising cathode candidate for RBMs.

However, no experimental results have been reported for Mg^{2+} intercalated into $\delta\text{-V}_2\text{O}_5$ to date, which is likely related to the possibility of metastability in the de-intercalation limit at RT. On the other hand, reversible Mg intercalation/de-intercalation was observed in thin-film $\alpha\text{-V}_2\text{O}_5$ with nanoscale thickness ($\sim 100 \text{ nm}$).⁵⁷ A capacity of 150 mA h g^{-1} , corresponding to $\text{Mg}_{0.5}\text{V}_2\text{O}_5$, was achieved with the voltage of $\sim 2.35 \text{ V}$ at $0.5 \mu\text{A cm}^{-2}$ (Fig. 20), in agreement with the calculation results, which predicted a voltage drop at $x_{\text{Mg}} \sim 0.5$ due to the formation of a stable Mg vacancy ordering.⁶¹

In another work, “solvent” molecules are incorporated in the cathode structure, which can presumably “shield” the charge on the Mg^{2+} electrostatically and attenuate the structural distortions.^{66,67} Xerogel V_2O_5 ($\text{V}_2\text{O}_5 \cdot n\text{H}_2\text{O}$) comprises a “bilayer” arrangement of V_2O_5 layers (Fig. 21),^{66,68} in contrast with the monolayer in α - and $\delta\text{-V}_2\text{O}_5$.^{69,70} A single bilayer of V_2O_5 is made up of two individual V_2O_5 monolayers (red polyhedra in Fig. 21), and intercalated guest species and H_2O molecules are present in the space between two bilayers. Such a bilayered framework host, with the interbilayer spacing of $\sim 13.5 \text{ \AA}$,⁷¹ can provide the structure flexibility to adapt to the geometry of the intercalant ions by

adjusting the interlayer separation. While each mole of H_2O added (removed) to (from) the structure results in an increase (decrease) of the interbilayer spacing by $\sim 2.8 \text{ \AA}$, the intercalated Mg^{2+} will lead to a decrease in the spacing.

The cycling of xerogel- V_2O_5 in Mg(TFSI)_2 /diglyme electrolyte achieved a discharge capacity of $\sim 50 \text{ mA h g}^{-1}$ ($0.25 \text{ Mg/V}_2\text{O}_5 \cdot n\text{H}_2\text{O}$) at $20 \mu\text{A cm}^{-2}$ (Fig. 22).⁶⁷ A plausible mechanism for the intercalation process was proposed: during discharge, a solvation shell (diglyme) coordinated Mg^{2+} enters the $\text{V}_2\text{O}_5 \cdot n\text{H}_2\text{O}$ bilayer and largely sheds the lattice water, resulting in the compression of interlayer distance ascribed to the attraction between V_2O_5 layers and Mg complex. Upon galvanostatic charge, Mg coordinated clusters are pulled out of the lattice, accompanied by free diglyme molecules and/or a reservoir of composed diglyme filling the lattice to compensate the void, resulting in the largest interlayer distance. This mechanism appears to be reversible at the expense of further electrolyte decomposition, likely accounting for a slightly gradual capacity escalation, and Mg metal passivation *via* decomposed electrolyte species and the removal of lattice water. However, the intercalation mechanism needed to be further confirmed in view of the large overpotential. The function of crystal water, whether just maintaining the crystal structure or improving the kinetics of Mg^{2+} diffusion, is still unknown.

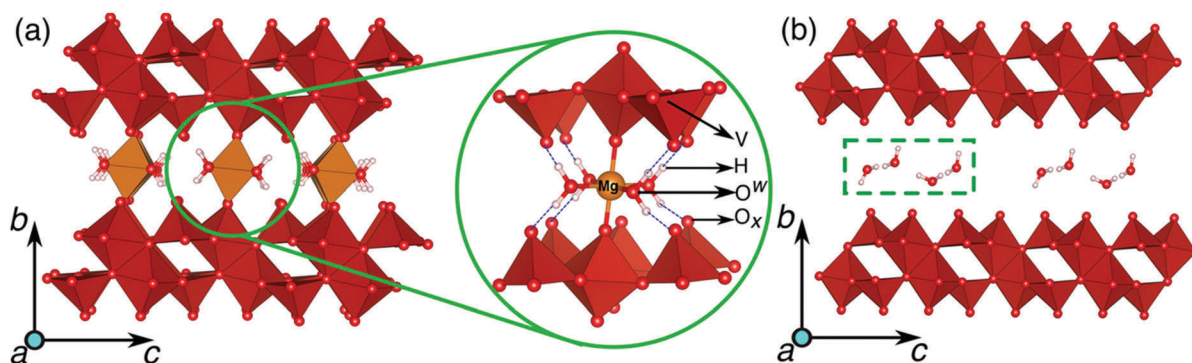


Fig. 21 The structures of the fully magnesiated ($x_{\text{Mg}} = 0.5$) and the fully demagnesiated xerogel structures, with $1\text{H}_2\text{O}$ per formula unit of V_2O_5 , are displayed in a and b, respectively. Reproduced from ref. 66 with permission from American Chemical Society, Copyright 2016.

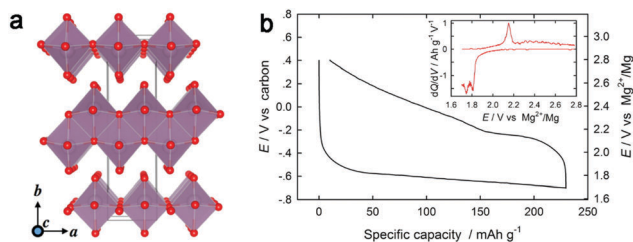


Fig. 23 (a) Crystal structure of layered α - MoO_3 (with Mo ions in violet, six-coordinated by oxygens in red); layers stack along the b axis. Reproduced from ref. 5 with permission from American Chemical Society, Copyright 2017. (b) Galvanostatic titration curve of α - MoO_3 thin-film electrode in 0.1 M $\text{Mg}(\text{TFSI})_2/\text{AN}$ solution (current density = $0.3 \mu\text{A cm}^{-2}$). Corresponding dQ/dV plot is provided in the inset. Reproduced from ref. 57 with permission from American Chemical Society, Copyright 2013.

2.5.2 α - MoO_3 . Sharing a similar layered structure with V_2O_5 , orthorhombic α - MoO_3 is known as an intercalation host for monovalent and divalent cations.^{72–76} It is built up by double layers of edge- and corner-sharing $[\text{MoO}_6]$ octahedra, which are held together by weak van der Waals attraction forces, with the interlayer distance of $\sim 6.929 \text{ \AA}$ (Fig. 23a).^{54,57,72} When intercalated into α - MoO_3 , Mg^{2+} occupies the sites within and between α - MoO_3 layers, running along the c -axis.⁷⁷ The migration barriers were calculated to be 880 meV, corresponding to the diffusion constant of $10^{-17} \text{ cm}^2 \text{ s}^{-1}$, much higher than the $\sim 525 \text{ meV}$ threshold, indicating sluggish diffusion kinetics.^{57,77–79} A thin α - MoO_3 film ($\sim 100 \text{ nm}$) electrode was prepared to reduce the diffusion path for the intercalating ion, somewhat mitigating the sluggish kinetics.⁵⁷ α - MoO_3 film delivered a magnesiation capacity of $\sim 220 \text{ mA h g}^{-1}$, corresponding to $0.59 \text{ Mg}^{2+}/\text{MoO}_3$, with voltage of 1.7–2.8 V at $0.3 \mu\text{A cm}^{-2}$ (Fig. 23b). The voltage difference (0.2–0.4 V) between the magnesiation and de-magnesiation process of α - MoO_3 (Fig. 23b), 3–6 times larger than that for V_2O_5 film,⁵⁷ indicates greater kinetic limitations. The large overpotential and some degree of irreversibility may be due to the voltage-induced structural damage,⁸⁰ lower electronic conductivity of demagnesiated MoO_3 ,^{81,82} and some possible conversion reactions at the surface of α - MoO_3 .⁸³ Therefore, modifications are needed to make α - MoO_3 a promising cathode candidate for RBMs.

2.5.3 $\text{MoO}_{2.8}\text{F}_{0.2}$. To enhance the kinetics of Mg intercalation, $\text{MoO}_{2.8}\text{F}_{0.2}$ with the α - MoO_3 structure was prepared by mild fluorination.⁸⁴ The introduction of fluorine liberates an electron that is delocalized over the entire Mo–O layer in the ac plane, which will increase the electronic conductivity of $\text{MoO}_{2.8}\text{F}_{0.2}$.^{85–87} Delocalization, introduced by fluorine atoms, contributes to the accommodation of charge introduced by Mg^{2+} intercalation and reduces the diffusion barrier of Mg^{2+} .⁷⁷ Like in α - MoO_3 , when intercalated into $\text{MoO}_{2.8}\text{F}_{0.2}$, Mg^{2+} ions occupy the sites within and between $\text{MoO}_{2.8}\text{F}_{0.2}$ layers, running along the c -axis. Meanwhile, the migration barriers are lowered to $\sim 490 \text{ meV}$, smaller than the 525 meV threshold.⁷⁷ Micrometer-sized $\text{MoO}_{2.8}\text{F}_{0.2}$ delivered a first-discharge capacity of $\sim 40 \text{ mA h g}^{-1}$ at $5 \mu\text{A}$, which increased to $\sim 70 \text{ mA h g}^{-1}$ ($0.25 \text{ Mg}^{2+}/\text{MoO}_{2.8}\text{F}_{0.2}$) in the 18th cycle, better than the

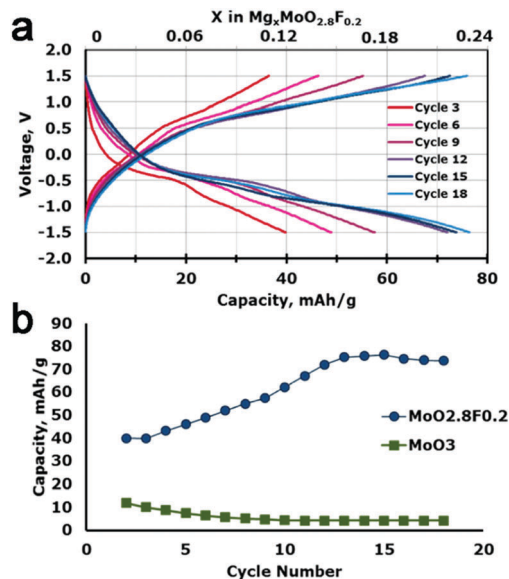


Fig. 24 (a) Voltage profile for $\text{MoO}_{2.8}\text{F}_{0.2}$ over the first 18 cycles and (b) capacity versus cycle number. Electrolyte is 0.2 M $\text{Mg}(\text{TFSI})_2$ in PC. Reproduced from ref. 84 with permission from American Chemical Society, Copyright 2016.

micron-sized α - MoO_3 (Fig. 24),⁸⁴ indicating halogen substitution may be a viable strategy for improving the kinetics of layered oxides.⁸⁸

2.5.4 $\text{Mo}_{2.5+y}\text{VO}_{9+\delta}$. Slow Mg diffusion in layered oxide-based cathodes (V_2O_5 and α - MoO_3) can be managed by the orthorhombic Mo–V oxides with open-tunnel structure.⁸⁹ The structure of Mo–V oxides contains layers, each of which is stacked by corner-sharing to form a microporous framework with three-, six-, and seven-membered ring tunnels (Fig. 25a and b).^{89–92} The diameters of the six- and seven-membered ring channels are approximately 3 and 5 \AA , respectively,⁹⁰ which can provide facile diffusion of Mg^{2+} . In Mo–V oxides, molybdenum or vanadium ions, which can change by two or more oxidation states, facilitate local electroneutrality and lower the barriers to Mg^{2+} diffusion.^{33,37}

$\text{Mo}_{2.5+y}\text{VO}_{9+\delta}$ ($\sim 200 \text{ nm}$ in diameter) achieved a capacity of 397 mA h g^{-1} (1st discharge) at C/70 and RT, corresponding to 3.49 Mg^{2+} per formula unit (Fig. 25c). The attainable capacity dropped to $\sim 114 \text{ mA h g}^{-1}$ and 90 mA h g^{-1} at rates of C/40 and C/12, respectively. An intercalation reaction mechanism is confirmed by the continuous XRD peak shifts with increasing Mg concentration.⁸⁹ Hence, combining mixed transition metal ions in oxides with an open-tunnel structure might contribute to the Mg^{2+} intercalation. Despite the low Mg mobility in the material, in view of its high capacity and cycle stability, $\text{Mo}_{2.5+y}\text{VO}_{9+\delta}$ might warrant further theoretical and experimental investigation.

2.6 Polyanion

Above we discussed oxides, sulfides, and selenides with 3D and 2D diffusion pathways as cathodes for RBMs. In this part, we will further discuss polyanion compounds with 1D diffusion channel.

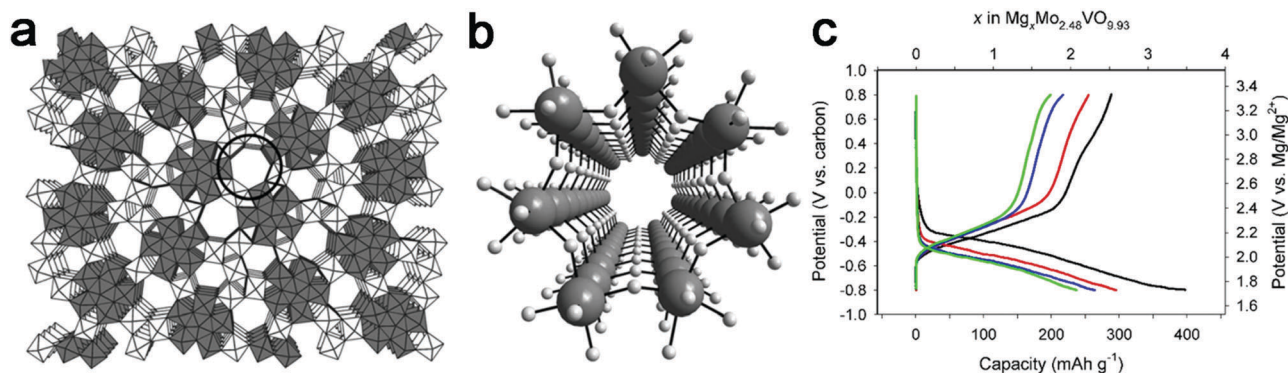


Fig. 25 Polyhedral representation of orthorhombic Mo–V oxide. The circle in (a) indicates a seven-membered ring. (b) Ball-and-stick representation of the channel structure. Reproduced from ref. 91 with permission from Royal Society of Chemistry, Copyright 2011. (c) Electrochemical discharge–charge profiles of an AC/Mo_{0.48}VO_{9.93} cell at C/70 (1C = 140 mA g^{−1}): 1st cycle, black; 2nd cycle, red; 5th cycle, blue; 10th cycle, green. Reproduced from ref. 89 with permission from American Chemical Society, Copyright 2016.

Given their great success in LIBs,^{93–96} polyanion compounds (mainly olivine) could be promising cathodes for RMBs.

The olivine structure consists of a distorted hexagonal close-packed (hcp) framework of oxygen with tetrahedral sites occupied by P or Si and two distinct octahedral sites: 4a occupied by Mg or Li, and 4c occupied by M ions (M = Fe, Mn, Co) (Fig. 26a).⁹⁷ 4a sites form linear chains of edge-sharing octahedra,

favoring the diffusion of ions along the 1D channel while maintaining the topology of olivine during cycling.^{98,99} Each 4a site connects the two nearest neighboring 4c sites, forming a zigzag 1D chain (Fig. 26b).

2.6.1 Phosphates. Mg²⁺ ions diffuse in olivine FePO₄ along the “wave-like” path from the octahedral (O) sites to the tetrahedral (T) sites (Fig. 27a).¹⁰⁰ The migration barrier of Mg²⁺ in FePO₄ is 580 meV, corresponding to a diffusivity of 10^{−13} cm² s^{−1}, while the migration barrier in the magnesiated FePO₄ (Mg_{0.5}FePO₄) is 1025 meV, much higher than the ~525 meV threshold, corresponding to a diffusivity constant of ~10^{−20} cm² s^{−1}, indicating that removal of Mg²⁺ from Mg_{0.5}FePO₄ is not possible (Fig. 27a). Olivine FePO₄ only delivered a capacity of ~12 mA h g^{−1} at 20 μA cm^{−2} (Fig. 27b), 6% of its theoretical capacity, which is attributed to surface amorphization that prohibits the electrochemical reaction from penetrating deeply into the bulk.¹⁰⁰ The amorphization is explained by the thermodynamically metastable intercalated product (Fig. 27c), which is demonstrated by calculations and the failure to synthesize Mg_{0.5}FePO₄ *via* the solid state route.

2.6.2 Silicates. Similarly, Mg²⁺ ions diffuse in silicate along the 1D channel from octahedral sites to tetrahedral sites (Fig. 26).⁹⁷ The migration barriers in MgMSiO₄ (M = Fe, Mn, Co) were calculated to be 740–770 meV (Fig. 28a),¹⁰¹ which is higher than the ~525 meV threshold, corresponding to a diffusivity constant of ~10^{−16} cm² s^{−1}, too high for Mg²⁺ to diffuse in silicates.

The majority of reports on silicates are presented by the same research group^{102–109} and demonstrate their high capacity and stable cycling performance. However, the reported average voltages are significantly lower than calculated results (Fig. 28b).⁹⁷ A more recent study re-examined silicates under the same conditions, but little capacity was achieved.¹⁰¹

The metastable orthorhombic MgFeSiO₄, with tetrahedrally coordinated Mg (Fig. 29a), delivered a reversible capacity of ~330 mA h g^{−1} at ~2.5 V, 6.62 mA g^{−1}, and 55 °C (Fig. 29c).¹¹⁰ The improved kinetics could be due to the tetrahedrally coordinated Mg, less favorable in energy than octahedrally coordinated Mg, which favors the Mg²⁺ diffusion.

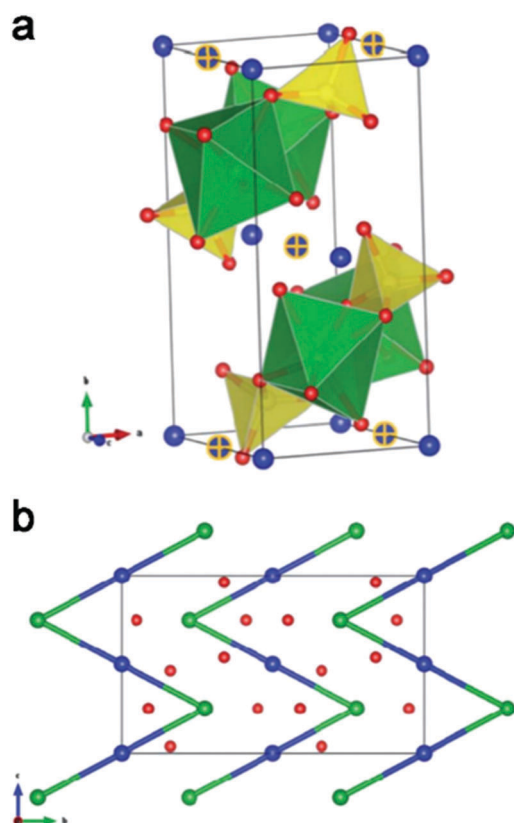
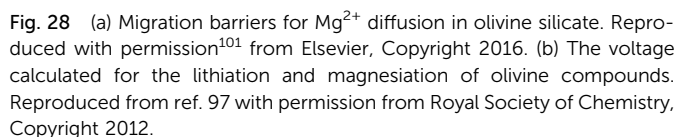
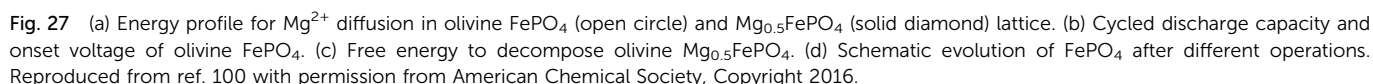


Fig. 26 (a) Crystal structure of olivine compounds. Red, oxygen; yellow, Si or P; green, transition metal (M) at 4c sites; and blue, Mg or Li at 4a sites. (b) 2D view of olivine structures along the (100) plane. Si/P atoms are neglected for simplicity. Reproduced from ref. 97 with permission from Royal Society of Chemistry, Copyright 2012.



In summary, reversible magnesiation of phosphate is prohibited by the surface amorphization, which blocks the electrochemical reaction from penetrating deeply into the bulk phase. Limited by high migration barriers, diffusion of Mg^{2+} in normal silicates is not possible unless at elevated temperature. Utilizing the less stable tetrahedrally coordinated Mg site in silicates can achieve superior Mg diffusivity and improved kinetics for Mg insertion/extraction. Despite some inconsistency in the full-cell studies, probably due to the electrochemical setup and electrolytes, it is worthwhile to further investigate Mg^{2+} intercalation into olivine silicate, given the promise of excellent energy density and safety.

2.7 Open framework

The open framework structure is a system containing voids with sizes ranging from a few angstroms to hundreds of angstroms.^{111–115} The large channels and interstices, beneficial for ion intercalation, fundamentally distinguish the open framework structure from other intercalation compounds.¹¹⁶ A typical example is the Prussian blue analogues (PBAs). PBAs have a typical formula of $A_xM_y[M'(CN)_6]$, in which M and M' refer to transition metal and CN refers to the ligand, which connects all transition metals and therefore forms an open framework (Fig. 30).^{116–119} The triple-bonded CN ligands increase the separation between M and M' ions and open up the structure for ion and small molecule insertion. Intercalated ions are likely to be at least partially hydrated,^{120,121} and larger hydrated ions occupy the interstitial A sites (4.6 Å in diameter) and diffuse along the open $\langle 100 \rangle$ channels (3.2 Å in diameter).¹²² Materials in the PBA family have been explored for reversible monovalent, divalent, and trivalent ion insertion.^{120,123–127} However, the

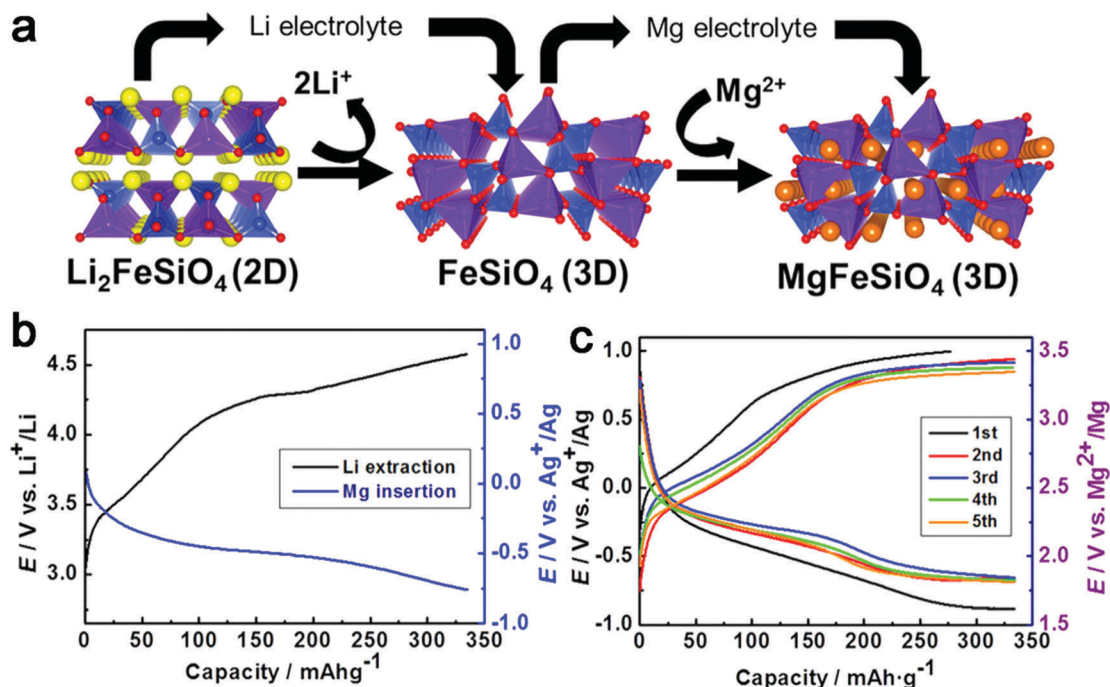


Fig. 29 (a) Schematic illustration of the ion-exchange methodology for the electrochemical synthesis of metastable orthorhombic MgFeSiO_4 from $\text{Li}_2\text{FeSiO}_4$. (b) Charge-discharge profiles for ion exchange process from $\text{Li}_2\text{FeSiO}_4$ to MgFeSiO_4 . (c) Charge-discharge profiles of ion-exchanged MgFeSiO_4 . All measurements were conducted at 55°C . Reproduced from ref. 110 with permission from Springer Nature, Copyright 2014.

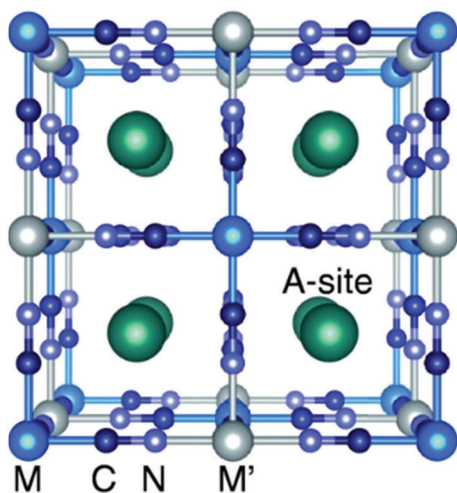


Fig. 30 Structure of a PBA $\text{A}_x\text{M}_y[\text{M}'(\text{CN})_6] \cdot n\text{H}_2\text{O}$. Cations A and water are accommodated in A-sites. M and M' are transition metal ions. Reproduced from ref. 118 with permission from The Electrochemical Society, Copyright 2015.

impact of various transition metals in PBAs on the thermodynamics (theoretical capacity and voltage) and kinetics (diffusivity) of the intercalation process requires further study.

Reversible Mg^{2+} intercalation was demonstrated with nickel hexacyanoferrate (NFCN), showing an initial capacity of $\sim 40 \text{ mA h g}^{-1}$ in $\text{Mg}(\text{TFSI})_2/\text{PC}$ electrolyte and increasing to 80 mA h g^{-1} in the 50th cycle (Fig. 31a), with a relatively high potential of $\sim 2.9 \text{ V}$ vs. Mg/Mg^{2+} and low overpotential (Fig. 31b).¹²⁸

Apart from the study in organic electrolyte, PBAs, including nickel hexacyanoferrate,¹²⁹ manganese hexacyanomanganate,¹¹⁶ copper hexacyanoferrate,^{116,123} and $\text{K}_{0.1}\text{Cu}[\text{Fe}(\text{CN})_6]_{0.7} \cdot 3.6\text{H}_2\text{O}$,¹³⁰ are also reported to intercalate Mg^{2+} reversibly in aqueous electrolyte (details in the following section). In order to investigate the different mechanisms of Mg^{2+} intercalation in PBAs in aqueous and nonaqueous electrolyte, PBA composed of Cu and Fe ions was studied using both aqueous and organic electrolytes.¹¹⁸ The redox potential of CuFe-PBA was approximately 3 V vs. Mg/Mg^{2+} in electrolytes with $\text{Fe}^{\text{III}}/\text{Fe}^{\text{II}}$ as the main redox active species. It delivered negligible capacity in organic electrolyte, while a capacity of $40\text{--}60 \text{ mA h g}^{-1}$ at 1C rate was achieved in aqueous electrolyte, suggesting that incomplete desolvation in the aqueous electrolyte could alleviate the electrostatic interaction of Mg^{2+} with the framework constituents, resulting in fast diffusion of Mg^{2+} ions (Fig. 31c and d).¹¹⁸

Reversible Mg^{2+} intercalation into PBAs is demonstrated both in organic and aqueous electrolytes, indicating that open framework structures with large voids can tolerate the diffusion of highly polarizing Mg^{2+} and co-intercalation of water molecules. However, the limited energy densities yielded by most PBAs frameworks hinder their practical application in RMBS.

3. Conversion cathode

Other than intercalation compounds, materials undergoing conversion reaction, which can achieve higher energy density in theory, are also investigated. In contrast to intercalation cathodes, magnesiation and de-magnesiation of conversion

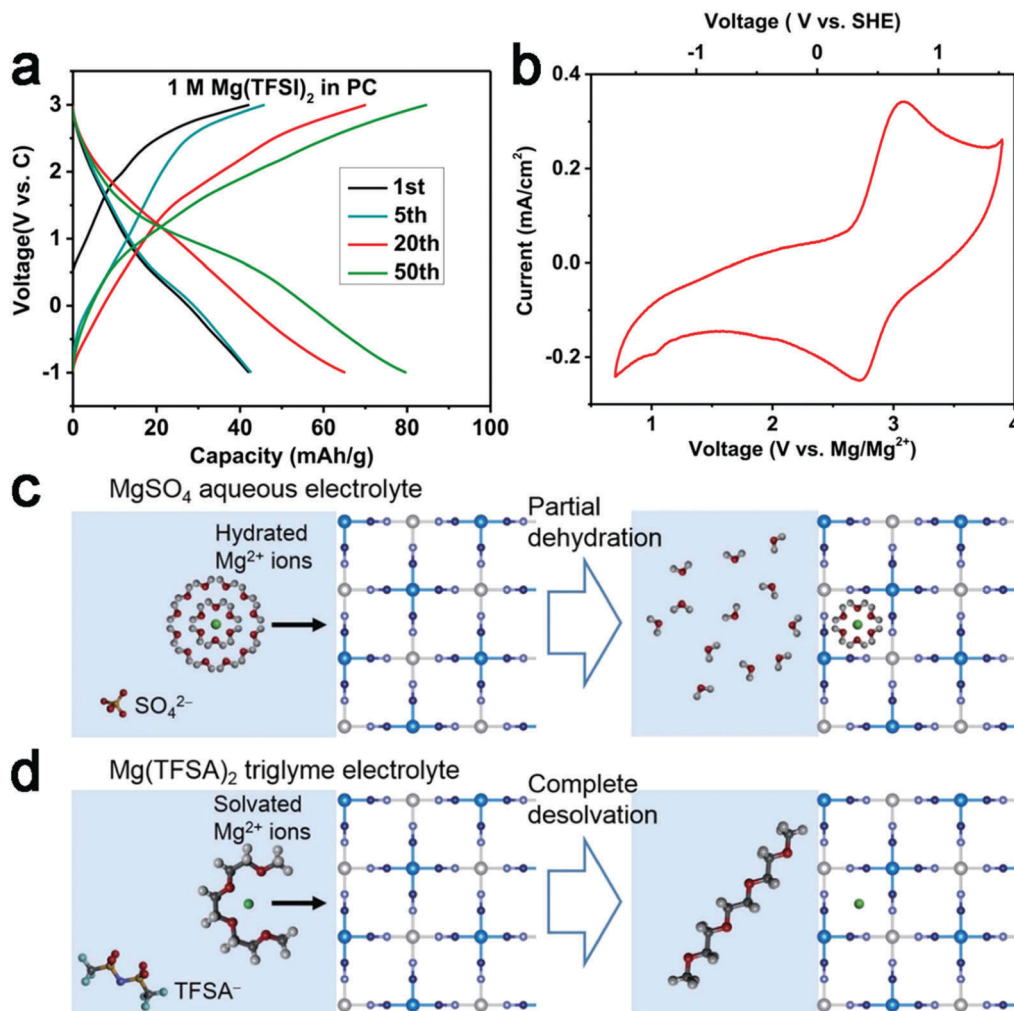
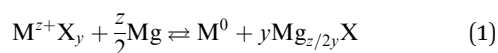


Fig. 31 (a) Galvanostatic cycling and (b) cyclic voltammograms of nickel hexacyanoferrate at a rate of 10 mA g^{-1} with 1 M Mg(TFSI)_2 in PC as the electrolyte. Reproduced from ref. 128 with permission from Elsevier, Copyright 2016. Schematic illustration of the insertion of Mg^{2+} ions into CuFe-PBA in (c) MgSO_4 aqueous electrolyte and (d) Mg(TFSA)_2 triglyme electrolyte. Reproduced from ref. 118 with permission from The Electrochemical Society, Copyright 2015.

materials break chemical bonds and create new ones during the insertion and extraction of Mg .^{131–133} According to eqn (1), cathode particles typically convert into nanocomposite particles comprising metal M nanoparticles dispersed in a $\text{Mg}_{z/2y}\text{X}$ matrix during magnesiation. The morphology and spatial correlation of the new phases may be controlled by diffusion coefficients of cations and anions, by electronic and ionic conductivity of new phases, as well as by interfacial energies. Conversion reaction usually occurs during ion insertion when the electrode materials do not have open ion diffusion channels, or the number of inserted ions exceeds the maximum available sites. Materials of this type include many transition metal oxides, sulfides, chloride, *etc.* Some manganese oxides, *e.g.*, $\alpha\text{-MnO}_2$ and ramsdellite- MnO_2 , despite their open channels for ion transport, are shown to undergo conversion reaction due to the strong distortion that damages the structure integrity.¹³⁴



3.1 MnO_2

Transition metal oxides are the most studied conversion material for Mg batteries due to their richness of compositions and crystal structures, especially manganese oxide. Mn atom usually coordinates with six O atoms, forming a MnO_6 octahedron. Such octahedra act as the building blocks for different polymorphs of MnO_2 . Depending on the size and orientation of the open channel between these octahedral building blocks, MnO_2 can be categorized as α -, β -, γ -, δ -, and λ -phases, with a 2×2 , 1×1 , and 2×1 sized 1D tunnel, 2D tunnel and 3D tunnel, respectively (Fig. 32).¹³⁵

3.1.1 $\alpha\text{-MnO}_2$. $\alpha\text{-MnO}_2$ (also hollandite phase) has 2×2 sized tunnels (Fig. 32), providing large ion transport channels. For this reason, its use has been demonstrated as an intercalation cathode for LIBs.^{136–139} Since the size of the channel ($\sim 5 \text{ \AA}$) is much larger than the size of Mg^{2+} (0.86 \AA), transport of Mg^{2+} along the channels is speculated to be energetically feasible.^{140–144} For Mg concentrations less than 0.25 in $\alpha\text{-Mg}_x\text{MnO}_2$, the migration barriers of $\sim 300\text{--}600 \text{ meV}$ (Fig. 33a) are comparable

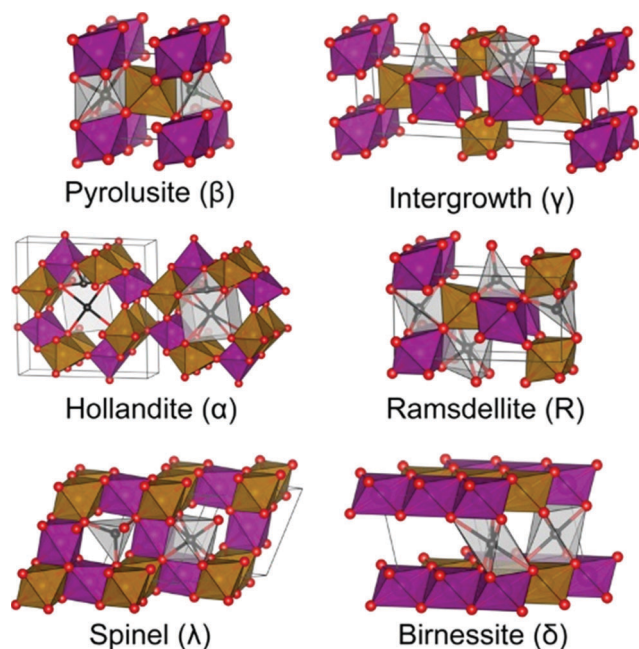


Fig. 32 Common polymorphs of MnO_2 and predicted sites for Mg intercalation. The purple and yellow spheres and surrounding the octahedra denote spin-up and spin-down Mn atoms and MnO_6 octahedra, while the black spheres and surrounding gray polyhedra denote potential intercalation sites for Mg ions in the structure. Reproduced from ref. 135 with permission from American Chemical Society, Copyright 2017.

to those for Li diffusion in typical LIB cathodes.¹⁴⁵ At Mg concentration higher than 0.25, the diffusion barrier significantly increases to $\sim 1300\text{--}1400$ meV, much higher than the threshold of ~ 525 meV, suggesting that the insertion of Mg^{2+} beyond 0.25 is not kinetically practical.¹¹

It was experimentally demonstrated that when a low magnesium concentration was intercalated (0.14 or 0.26 $\text{Mg}/\alpha\text{-MnO}_2$), $\alpha\text{-MnO}_2$ showed good cycling performance. When a high magnesium concentration was intercalated (0.47 $\text{Mg}/\alpha\text{-MnO}_2$), the capacity faded quickly, in accordance with the calculations.^{142,143,146} Attempts have been made to advance the cycling performance, including adding acetylene black into $\alpha\text{-MnO}_2$ to enhance its electronic conductivity¹⁴⁴ and stabilizing $\alpha\text{-MnO}_2$ tunnels with K^+ cation,⁸³ but without success.

The experiment on MnO_2 with various morphologies further revealed that the magnesiation process was strongly governed by the active surface area of MnO_2 (Fig. 33b).¹⁴³ Microscopic and spectroscopic investigations found that an amorphous layer was generated in the $\alpha\text{-MnO}_2$ after the first electrochemical magnesiation,⁸³ while crystalline grains were still observed in the center of the nanorod, forming a core@shell morphology. Manganese was reduced to Mn^{2+} in the shell, whereas Mn^{4+} remained in the core. This experimental observation indicates that the discharge of $\alpha\text{-MnO}_2$ results in a conversion reaction outcome.

To reveal why the conversion reaction occurs during magnesiation of $\alpha\text{-MnO}_2$, a comprehensive analysis was conducted.¹⁴¹ The most stable phase of discharge products is calculated to be the mixture of crystalline MgO and manganese oxide (Fig. 34a),

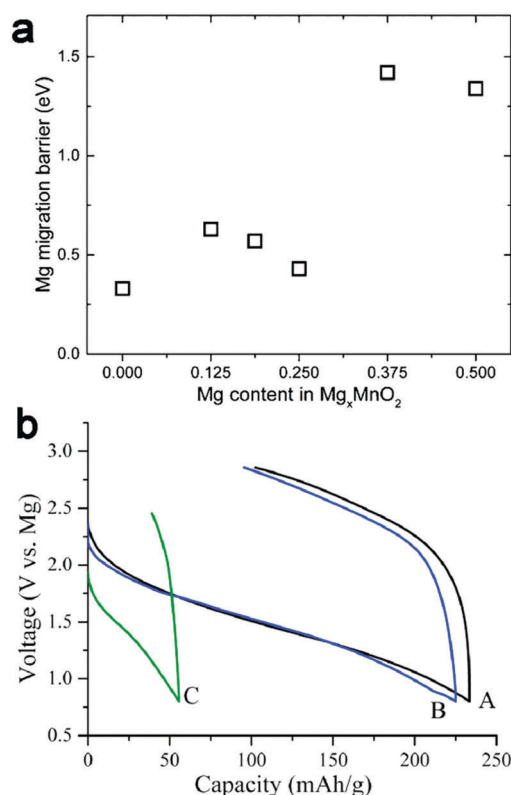


Fig. 33 (a) Mg hopping barrier in the ground states of $\alpha\text{-Mg}_x\text{MnO}_2$. Reproduced from ref. 141 with permission from American Chemical Society, Copyright 2015. (b) Initial discharge-charge profiles of $\alpha\text{-MnO}_2$ nanorods (A, B, and C) with different surface areas (231, 149, and $30\text{ m}^2\text{ g}^{-1}$, respectively). The cells were operated at a current density of 0.02 mA cm^{-2} under room temperature. Reproduced from ref. 143 with permission from Elsevier, Copyright 2015.

which, however, may not form in practical operation due to kinetic hindrance from phase transformation. The energy to form amorphous Mg_xMnO_2 is lower than that to form intercalated $\alpha\text{-Mg}_x\text{MnO}_2$, and the voltage for the formation of amorphous oxides is always higher than that for the intercalation reaction (Fig. 34b), indicating the thermodynamic preference for the reaction to occur *via* the conversion path. Besides, volumes of amorphous oxide are reduced compared to the intercalated crystalline compounds (Fig. 34c), which are beneficial for relaxing the expansion caused by the insertion of Mg, further improving the thermodynamic stability of amorphous Mg_xMnO_2 relative to intercalated $\alpha\text{-Mg}_x\text{MnO}_2$. Therefore, two possible reaction routes exist (Fig. 34d): the direct conversion from the beginning, which is thermodynamically preferable, or starting with partial Mg-intercalation, followed by the structure destruction. Even if the metastable intercalation could occur, the concentration of intercalated Mg is limited to $\alpha\text{-Mg}_{0.125}\text{MnO}_2$, beyond which the structure of the intercalated compound undergoes a strong tetragonal-to-orthorhombic distortion, resulting in the formation of magnesium and manganese oxides. Above all, the conversion path is thermodynamically preferable to the intercalation path, consistent with the experimental observation that the discharge of $\alpha\text{-MnO}_2$ forms an

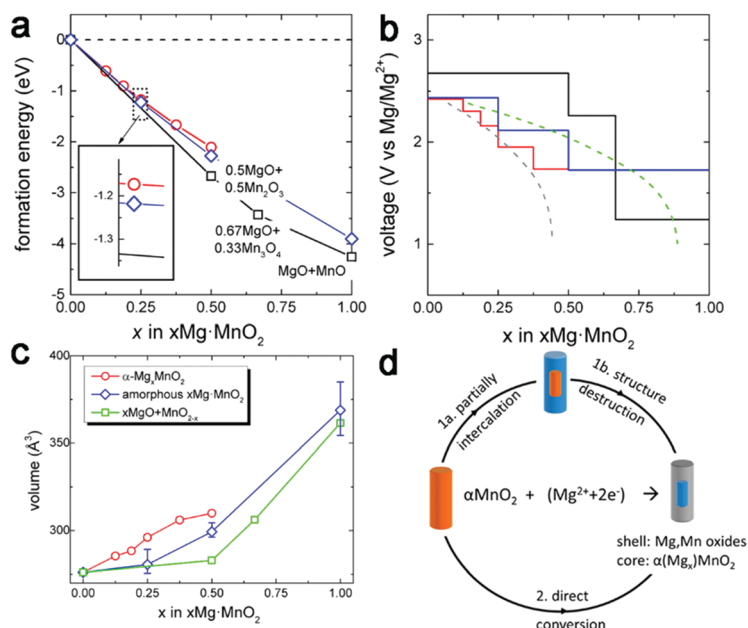


Fig. 34 (a) Reaction energy with the formation of intercalated compound (red), amorphous magnesium and manganese oxides (blue), and crystalline magnesium and manganese oxides (black). (b) Voltage profile for the reaction between Mg and $\alpha\text{-MnO}_2$ to form intercalated compound (red), amorphous magnesium and manganese oxides (blue), and crystalline magnesium and manganese oxides (black). The dashed line shows the average experimental voltage profile, assuming that all (gray) or half (green) of $\alpha\text{-MnO}_2$ participates in the first cycling. (c) Volumetric evolution of magnesiated $\alpha\text{-MnO}_2$ following different reaction paths. (d) Possible reaction routes for the magnesiation of $\alpha\text{-MnO}_2$. Reproduced from ref. 141 with permission from American Chemical Society, Copyright 2015.

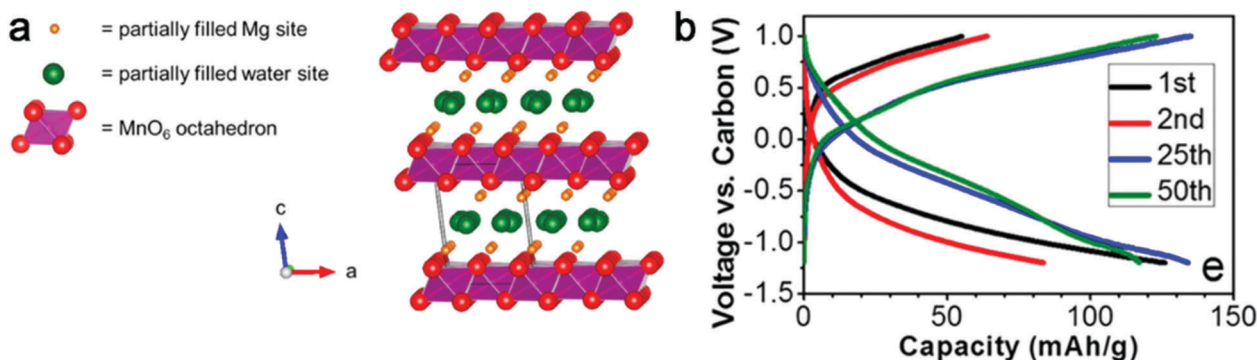


Fig. 35 (a) Birnessite crystal structure showing a water monolayer between the MnO_2 sheets. (b) Electrochemistry of $\delta\text{-MnO}_2$ /carbon cloth for RMBs in the nonaqueous electrolyte at C/10. Reproduced from ref. 149 with permission from American Chemical Society, Copyright 2016.

amorphous shell of magnesium and gradually reduced manganese oxides.

Other than $\alpha\text{-MnO}_2$, few studies are performed on other 1D MnO_2 structures, either due to the small size of the tunnel (β) or the complexity of the structure.^{135,143,147,148}

3.1.2 $\delta\text{-MnO}_2$. $\delta\text{-MnO}_2$, or birnessite, consists of stacked MnO_2 planes with structural water in the interlayer space and the interlayer distance of $\sim 7 \text{ \AA}$, which provides a 2-dimensional diffusion path for Mg^{2+} (Fig. 35a).¹⁴⁹

Mg^{2+} intercalation into $\delta\text{-MnO}_2$ has been reported under aqueous conditions,^{149,150} which will be discussed in the following section. In 0.25 M $\text{Mg}(\text{TFSI})_2/\text{diglyme}$ electrolyte, $\delta\text{-MnO}_2$ showed a capacity of $\sim 135 \text{ mA h g}^{-1}$ after 20 cycles at C/10 before the capacity slowly decayed (Fig. 35b).¹⁴⁹

A conversion mechanism takes place during cycling in the non-aqueous electrolyte, with the formation of MnOOH , MnO , and $\text{Mn}(\text{OH})_2$ upon discharge, which might result not only from the slow diffusion kinetics of Mg^{2+} but also the presence of surface bonded TFSI^- blocking the intercalation. No calculations on the diffusion barriers of Mg^{2+} in $\delta\text{-MnO}_2$ have been done, nor for the thermodynamic stability of intercalated products. However, according to the experimental results, the diffusion barriers are probably too high to intercalate Mg^{2+} .

For spinel $\lambda\text{-MnO}_2$, as discussed in Section 2, a very low degree of magnesiation was obtained ($< 3 \text{ at\% Mg per } \lambda\text{-MnO}_2$) in non-aqueous electrolyte.²⁹ However, no convincing evidence exists for Mg^{2+} intercalation into $\lambda\text{-MnO}_2$. Based on the discussion on $\alpha\text{-MnO}_2$ and $\beta\text{-MnO}_2$, a conversion reaction may also happen,

generating amorphous magnesium and manganese oxide, which block the further magnesiation of λ - MnO_2 . This speculation needs to be further confirmed.

3.2 Chalcogenide

3.2.1 CuS. As ion diffusion in solid state and the desolvation process upon interfacial charge transfer are thermally activated processes,^{151–154} high temperature testing is necessary for many materials that do not show electrochemical activity at RT. Recently, Nazar *et al.* proposed a high temperature test protocol and successfully realized reversible Mg intercalation/de-intercalation in both spinel²⁴ and layer TiS_2 ²² at 60 °C. Also, with a modified Swagelok cell in APC/G4, CuS with 5–10 mm particles achieved an initial discharge capacity of 550 mA h g⁻¹ at 150 °C, corresponding to 98% of the theoretical capacity (Fig. 36),¹⁵⁵ in contrast to its negligible capacity at RT. Although the high temperature helps to overcome the low mobility of Mg^{2+} , it also increases the kinetics of parasitic reactions. Further work, such as binder optimization and nanosizing CuS particles,¹⁵⁶ needs to be done to achieve comparable capacity at lower temperature.

3.2.2 Cu₂Se. According to the discussion in Section 2, selenides can present better kinetics than oxides and sulfides. β - Cu_2Se , as a super ionic conductor due to the high mobility of Cu^+ ,^{157–159} has been demonstrated to be feasible for the

reversible displacement reaction, which is a subcategory of conversion reactions.^{160–162} When used as the cathode for RMBs, β - Cu_2Se delivered a specific capacity of ~ 120 mA h g⁻¹ at 5 mA g⁻¹ (Fig. 37a), which increased to 230 mA h g⁻¹ (88.5% of its theoretical capacity) with nanosized crystals (Fig. 37b) at RT (Fig. 37c).¹⁶³ Despite the high capacities at RT, the practical application of β - Cu_2Se is limited due to the heavy and poisonous selenium.

Displacement reactions open a path to search a new class of electrode materials for RMBs. However, to date, only a few copper compounds have been reported to follow the displacement mechanism, because of the high mobility of copper ion. Further study on other metal compounds with high mobility needs to be done.

3.3 Chloride

Given the slow solid-state diffusion of Mg^{2+} , a novel conceptual Mg battery is proposed to address the kinetic hurdle by using chloride as the cathode.¹⁶⁴ In these materials, the formed MgCl_2 can easily dissolve into the electrolyte, avoiding the sluggish solid state Mg^{2+} diffusion, thus achieving ultrafast rate capability. AgCl/Mg battery achieved an initial discharge capacity of 178 mA h g⁻¹ (95.2% of the theoretical capacity) at 0.12C (23 mA g⁻¹) with a flat plateau of ~ 2.0 V (Fig. 38a). Even at 10C, the capacity remains at 104 mA h g⁻¹ (Fig. 38b), which is the highest rate capability ever reported for RMBs and can be attributed to the high mobility and high reversibility of Cl^- anion species.

In view of the high solubility of chloride in organic electrolyte, AgCl/Mg battery suffers from poor cyclability. Also, the energy density of the AgCl/Mg battery system is compromised by the amount of electrolyte required to dissolve the discharged product, MgCl_2 .¹⁶⁴ Nevertheless, its high rate capability makes the AgCl/Mg battery suitable for special applications requiring high rate, such as unmanned planes.

3.4 Organic compounds

As discussed above, inorganic intercalation materials are limited by the slow diffusion of Mg^{2+} , along with low intrinsic conductivity. An alternative approach is to use redox-active organic materials in which intermolecular forces may be weaker than those in inorganic materials and which thus interact less strongly with Mg^{2+} .⁶ In contrast to the valence change of the transition metal in inorganic cathodes, the redox reaction is based on the charge state change of the electroactive organic group or moiety in organic cathodes.^{165–168} The abundance and diversity of organic materials, benefiting from their flexible structure and tunability, can provide an opportunity for high-capacity and high-rate organic cathodes for RMBs, especially in terms of the resource sustainability and environmental friendliness.

An typical organic material is quinone.¹⁶⁹ 2,5-dimethoxy-1,4-benzoquinone (DMBQ) was reported to have low solubility in electrolyte,¹⁷⁰ high theoretical capacity (319 mA h g⁻¹),¹⁷¹ and much slower capacity decay upon cycling in LIBs.¹⁷⁰ However, when used as cathode for RMBs, its capacity faded fast, and low discharge voltage and large overpotential (~ 1 V) were observed,

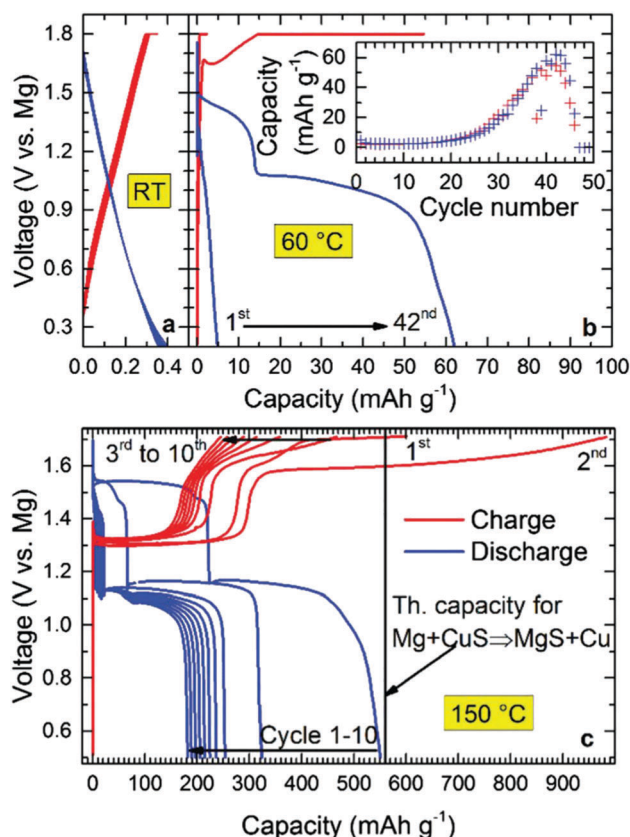


Fig. 36 Galvanostatic discharge and charge curves of CuS cycled at: (a) 25 °C in APC-THF; (b) 60 °C in APC-THF; (c) 150 °C in APC-G4. Reproduced from ref. 155 with permission from Royal Society of Chemistry, Copyright 2016.

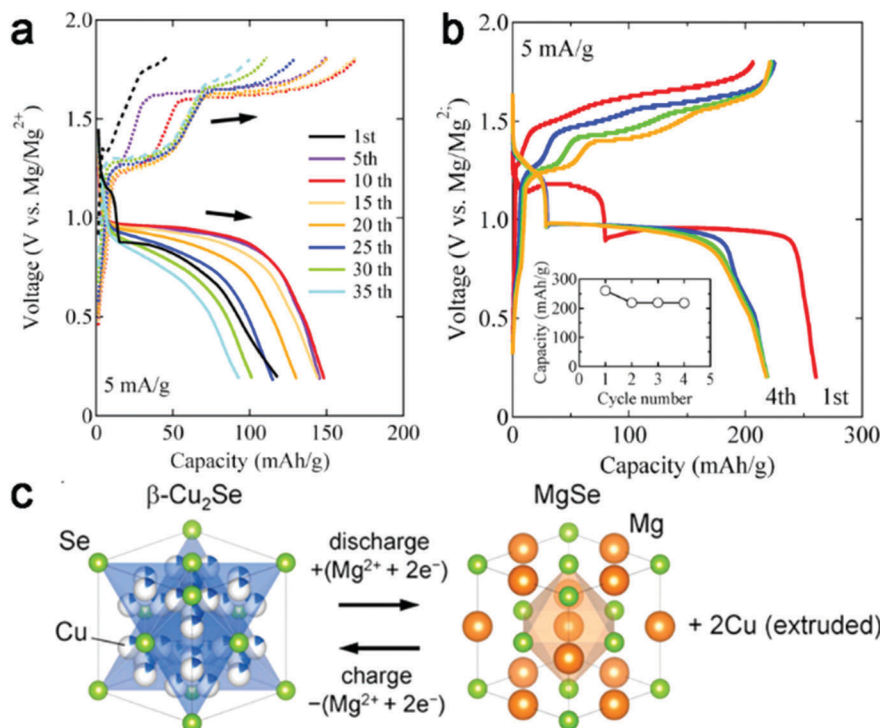


Fig. 37 The charge/discharge curve of β - Cu_2Se cathode with the length of (a) $1\ \mu\text{m}$ and (b) $\sim 100\ \text{nm}$. (c) The schematic illustration for the displacement of Cu ions in β - Cu_2Se with Mg ions to MgSe. Reproduced from ref. 163 with permission from Elsevier, Copyright 2016.

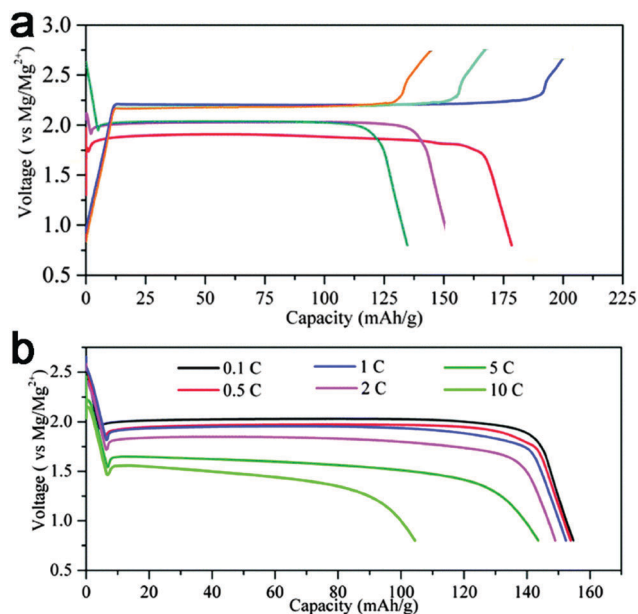


Fig. 38 (a) Galvanostatic curves for the Mg/AgCl battery. (b) Galvanostatic discharge curves for the AgCl/Mg batteries at different C rates. 1C is equal to $186\ \text{mA g}^{-1}$. Reproduced from ref. 164 with permission from Royal Society of Chemistry, Copyright 2015.

which was likely due to the incompatibility of electrolytes with metal Mg.¹⁷²

Another two magnesium electrolytes, $\text{Mg}(\text{TFSI})_2$ - MgCl_2 /DME and $\text{Mg}(\text{TFSI})_2$ /diglyme, were applied to study DMBQ.¹⁷¹

$\text{Mg}(\text{TFSI})_2$ - 2MgCl_2 /DME, which is capable of plating/stripping Mg (Fig. 39a), enabled Mg-DMBQ batteries with a discharge potentials of $\sim 2.0\ \text{V}$ (Fig. 39b), higher than the previously reported potential ($1.1\ \text{V}$).^{169,172} However, a considerable capacity loss, caused by electrode dissolution, was observed upon cycling.¹⁷¹

In addition to DMBQ, two new quinone-based polymers, 2,6-polyanthraquinone (26PAQ) and 1,4-polyanthraquinone (14PAQ) (Scheme 1), are reported.¹⁷³ In contrast to the slow capacity fading of 26PAQ, 14PAQ showed the best cycling stability in the $\text{Mg}(\text{HMDS})_2$ - 4MgCl_2 /THF electrolyte. Beyond the considerable capacity loss in the first few cycles, more than 1000 cycles with slight loss of capacity and good rate capacity of 14PAQ were achieved (Fig. 40a).¹⁷³ Unlike the structurally rigid polymer chain of 26PAQ, the redox-active quinonyl moieties in 14PAQ lie on the side of the main polymer chain (Scheme 1), allowing the rotation flexibility of anthraquinonyl groups along the polymer chain. The rotation flexibility helps to minimize the space hindrance and relax the structural stress of the polymer, which in turn provides better structure stability for 14PAQ.¹⁷³ In addition, upon discharging, the inserted Mg^{2+} species can be better stabilized by the two adjacent carbonyl ($\text{C}=\text{O}$) groups *via* the chelating effect, which has also been demonstrated to account for the enhanced cycling performance.¹⁷⁴

PAQS was also investigated as the cathode for RMBs with three different non-nucleophilic electrolytes: $[\text{Mg}_2\text{Cl}_3\cdot 6\text{THF}]$ [HMDSAlCl_3] in THF (MHCC), $\text{MgCl}_2\text{-AlCl}_3$ in THF (MACC), and $\text{MgCl}_2\text{-Mg}(\text{TFSI})_2$ in a mixture of THF and glyme (MTCC). Capacities between 150 and $200\ \text{mA h g}^{-1}$ at $1.5\text{--}2.0\ \text{V}$ were obtained (Fig. 40b).¹⁷⁵ Among the three electrolytes, MTCC

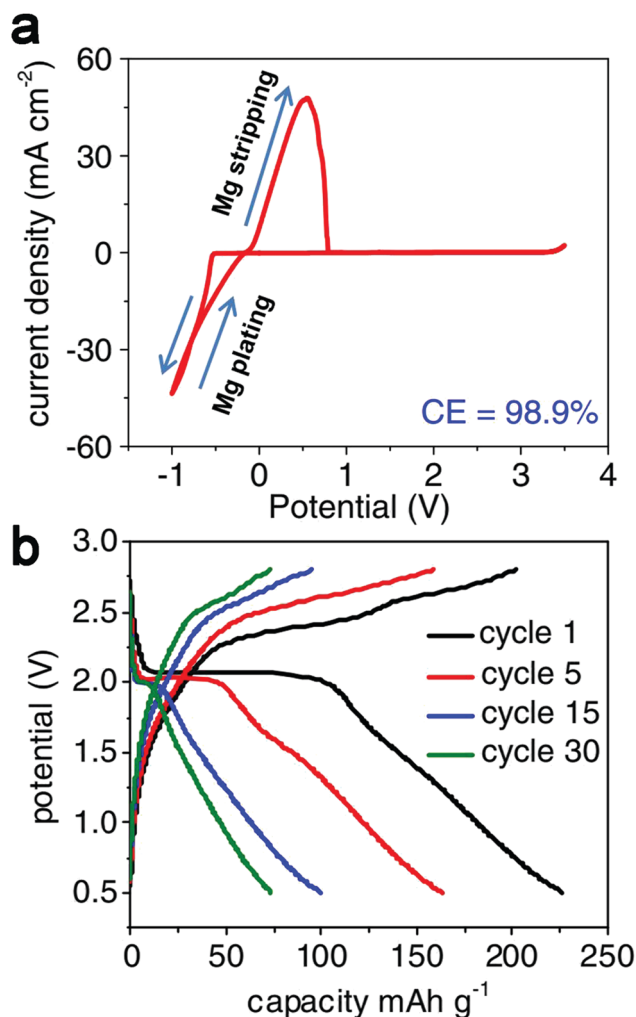


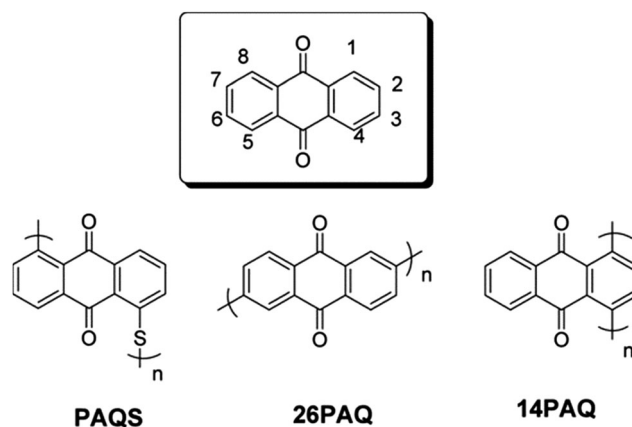
Fig. 39 (a) Steady state cyclic voltammograms in 0.5 M $\text{Mg}(\text{TFSI})_2$ – $2\text{MgCl}_2/\text{DME}$. (b) Representative charge–discharge profiles of the Mg–DMBQ cell using 0.5 M $\text{Mg}(\text{TFSI})_2$ – 2MgCl_2 in DME electrolyte at a current rate of 0.2C. Reproduced from ref. 171 with permission from The Electrochemical Society, Copyright 2016.

showed the best performance in terms of capacity and rate capability, but without significant improvement in long-term cycling over MHCC and MACC.¹⁷⁵

In summary, benefitting from their low cost and environmental benignancy, organics can be promising cathodes for RMBs. Yet, some challenges remain: the development of electrolyte systems to suppress electrode dissolution, discovery of more efficient electroactive structures, understanding of the charge/ion transport mechanism, and approaches to improve electrode stability.

4. Water co-intercalation

As discussed above, the kinetics of intercalation cathodes with organic electrolytes are limited by the slow interfacial charge transfer and sluggish diffusion. Studies have revealed that trace water in organic electrolyte can co-intercalate with Mg^{2+} , which



Scheme 1 The nomenclature of anthraquinone and the chemical structures of PAQS, 26PAQ, and 14PAQ. Reproduced from ref. 173 with permission from Wiley-VCH, Copyright 2016.

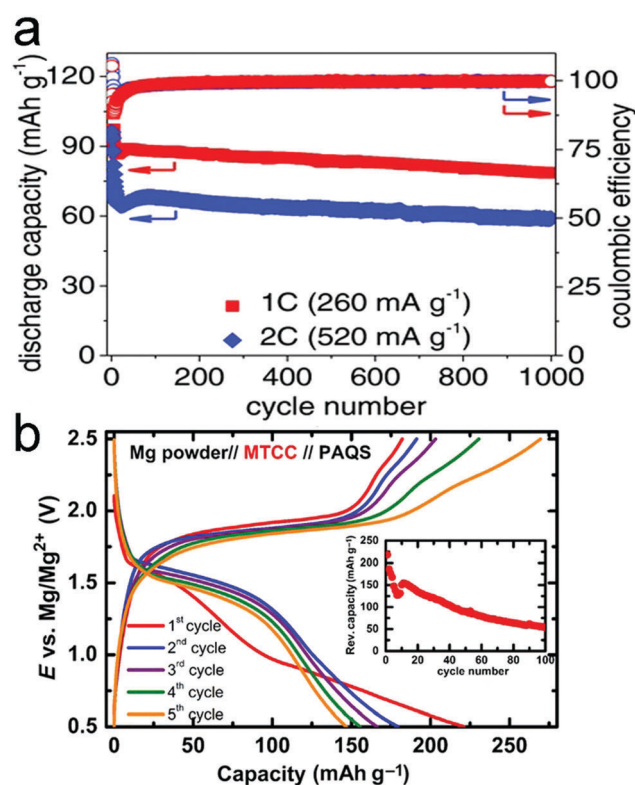


Fig. 40 (a) Mg–14PAQ cycling performance in the $\text{Mg}(\text{HMDS})_2$ – $4\text{MgCl}_2/\text{THF}$ electrolyte: capacities and coulombic efficiency profiles at the current rates of 1C and 2C ($1\text{C} = 520 \text{ mA g}^{-1}$). Reproduced from ref. 173 with permission from Wiley-VCH, Copyright 2016. (b) Galvanostatic curves for cycling of PAQS in MTCC between 0.5 and 2.5 V with a current density of 50 mA g^{-1} . Reproduced from ref. 175 with permission from Wiley-VCH, Copyright 2015.

could accelerate both interfacial ion transfer and ionic diffusion because of the screening effect.^{29,30,60,149,150,176}

The important role of water in wet electrolyte during Mg^{2+} intercalation is investigated in $\alpha\text{-V}_2\text{O}_5$ without H_2O in the structure. $\alpha\text{-V}_2\text{O}_5$ achieved the capacity of 260 mA h g^{-1} using 1 M $\text{Mg}(\text{TFSI})_2/\text{G2}$ with 2600 ppm water in the electrolyte

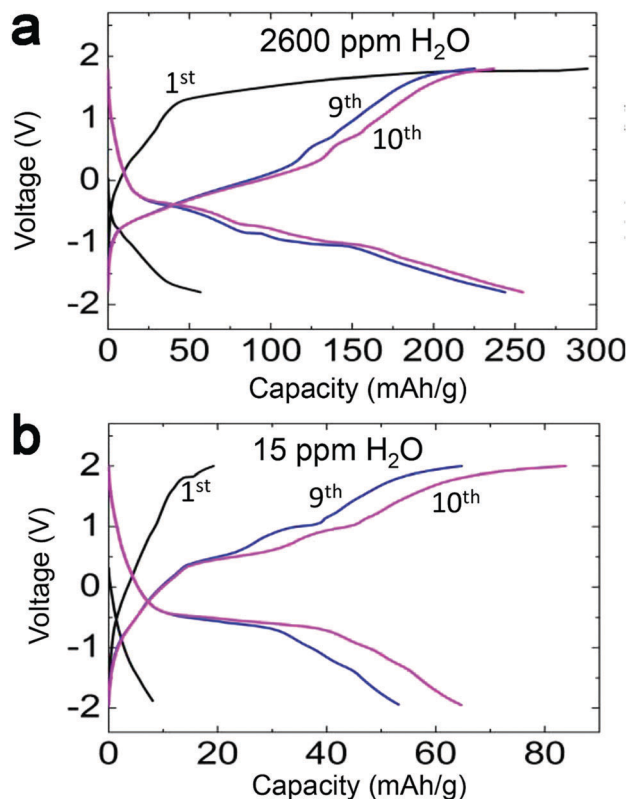


Fig. 41 Galvanostatic cycling of α - V_2O_5 vs. carbon coin cell in 1 M $\text{Mg}(\text{TFSI})_2/\text{G2}$ with (a) 2600 ppm H_2O and (b) 15 ppm H_2O at 20 mA cm^{-2} . Reproduced from ref. 60 with permission from Elsevier, Copyright 2016.

(Fig. 41a), much higher than 60 mA h g^{-1} in the dry electrolyte system (with 15 ppm H_2O) (Fig. 41b).⁶⁰ NMR results indicate that protons might participate in the intercalation process. However, the content of intercalated protons, as well as the

relationship between proton intercalation and water concentration in electrolyte, are yet to be explored.

To identify which species (e.g., desolvated magnesium ions, protons, hydronium ions, water- or solvent-solvated magnesium ions, or any combination of these) are intercalated into the host structure during electrochemical reduction, the crystal structure of the magnesium-inserted α - V_2O_5 , electrochemically reduced in the wet organic electrolyte, was studied.¹⁷⁷ The refined crystal structure was compared with the original V_2O_5 structure (Fig. 42). Distortions from the original VO_3 square pyramidal symmetry can be clearly found (Fig. 42b), where V1 and V3 maintain the five-coordination with oxygen, while V2 has only four oxygen atoms, like a tetrahedron. Eight oxygen atoms with similar center-to-oxygen distances of $\sim 2.47 \text{ \AA}$ coordinate the Cv_1 site (Fig. 42c). Therefore, the Cv_1 cavity size is sufficient for a single ion (Mg^{2+} or proton), but too small for solvated magnesium, such as $\text{Mg}(\text{H}_2\text{O})_n^{2+}$ or $\text{Mg}(\text{solvent}, \text{H}_2\text{O})_n^{2+}$, or for H_3O^+ or H_2O .

The Cv_2 site is coordinated by 12 oxygen atoms with various center-to-oxygen distances (average of 2.76 \AA) (Fig. 42c). Even though this cavity appears to be slightly larger than Cv_1, it is unlikely occupied by species other than single magnesium or protons because the closest distance to lattice oxygen, not the average value, is the determining factor for its suitability. The closest distance of the 12 center-to-oxygen distances in Cv_2 is shorter than 2.25 \AA . The Cv_3 site is surrounded by nine oxygen atoms with an average center-to oxygen distance of 2.48 \AA (Fig. 42c), which, similarly, is too small to accommodate H_2O or larger chemical species other than single magnesium ions or protons. Consequently, the only species intercalated into the vanadium pentoxide can be Mg^{2+} and H^+ , and not the other species ($\text{Mg}(\text{H}_2\text{O})_n^{2+}$, $\text{Mg}(\text{solvent}, \text{H}_2\text{O})_n^{2+}$, H_3O^+ or H_2O), which is not consistent with the previous simulation.⁶⁶ Yet, it is still unclear about how many H^+ ions are intercalated, and further work needs to be done.

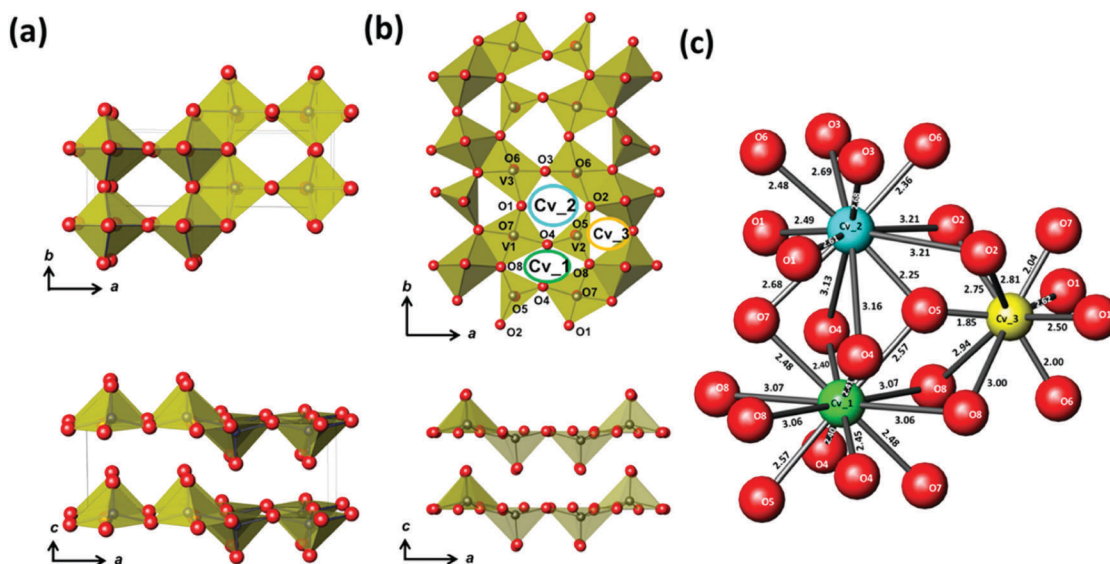


Fig. 42 (a) Crystal structure of the pristine V_2O_5 , (b) Mg -inserted V_2O_5 , and (c) local structures surrounding the cavity sites, denoted as Cv_ m ($m = 1, 2, 3$) in panel b. The numbers denote interatomic distances. Reproduced from ref. 177 with permission from American Chemical Society, Copyright 2017.

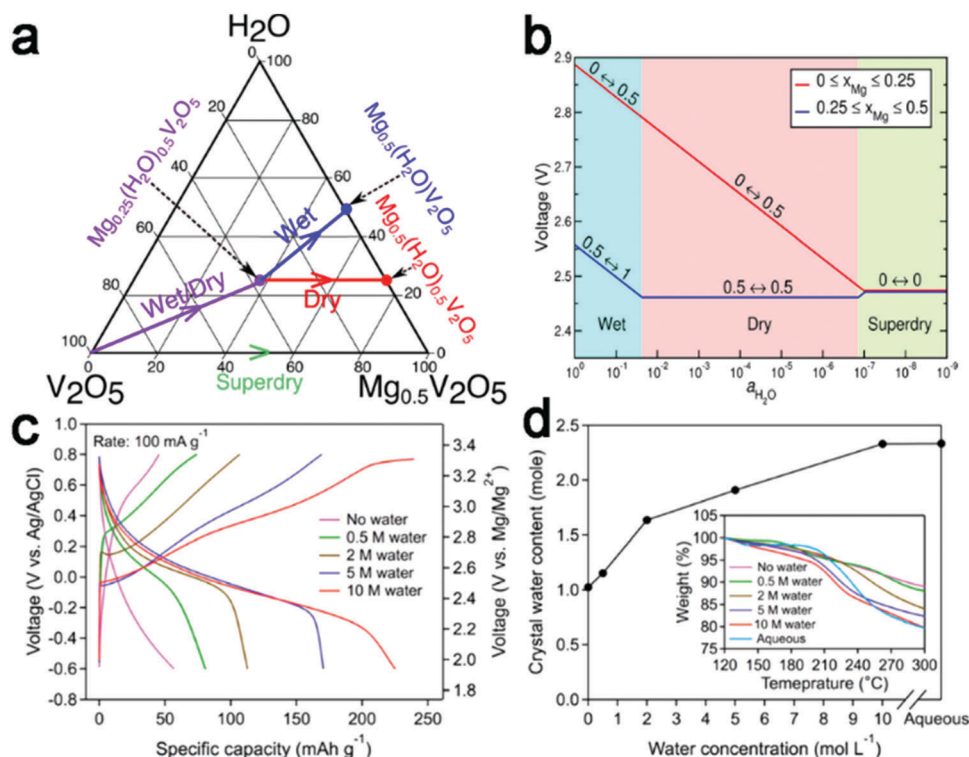


Fig. 43 (a) Ternary phase diagram of the Mg-(xerogel) V_2O_5 - H_2O system, which summarizes the possible equilibrium phases under different electrolyte conditions. (b) Average Mg insertion voltage for low (red line) and high (blue) Mg concentrations as a function of the electrolyte water content ($a_{\text{H}_2\text{O}}$). Reproduced from ref. 66 with permission from American Chemical Society, Copyright 2016. (c) The first discharge-charge voltage profiles of the birnessite MnO_2 cathodes with different water concentrations in acetonitrile-based electrolyte. (d) The water content in Mg-B at fully discharged state obtained from TGA profiles (inset). Reproduced from ref. 150 with permission from American Chemical Society, Copyright 2015.

In xerogel V_2O_5 with structural H_2O (Fig. 21), water co-intercalation with Mg^{2+} depended on water activity in the electrolyte, ranging from full co-intercalation in the wet condition to none in superdry conditions (Fig. 43a). The measured voltages would change if co-intercalation of the solvent/electrolyte with the redox ion occurs, leading to a co-dependence on the solvent/electrolyte chemical potential (Fig. 43b). The Mg^{2+} intercalation voltage was calculated to be higher in a wet electrolyte than in a dry electrolyte.

Birnessite MnO_2 with structural H_2O (Fig. 35a) achieved increasing specific capacity as the water concentration in acetonitrile-based electrolyte rose, in conjunction with decreased overpotential values (Fig. 43c).¹⁵⁰ As the water concentration in the electrolyte increases, the water content in birnessite MnO_2 host becomes higher (Fig. 43d), which confirms the insertion of hydrated Mg^{2+} . The maximal number of water molecules that are co-intercalated into Birnessite MnO_2 together with each Mg^{2+} is around 3.

In wet electrolyte, the proton intercalation will always occur,^{178,179} while the amount of intercalated protons are related to the water activity. The hydrated Mg^{2+} intercalation depends on the sufficient interlayer space of cathodes. Even though the capacity and rate capability of Mg^{2+} intercalation into cathodes can be improved by the presence of water in organic electrolytes, this approach has some drawbacks. It leads to a large effective radius of the intercalated moieties, which may lead to excessive

structural deformations of the host. Also, wet solutions are not compatible with magnesium anodes. The feasibility of Mg^{2+} co-intercalation with polar organic molecules, which can screen the interaction between Mg^{2+} and the host lattice, is worth investigating.

5. Elemental redox chemistry

As introduced above, cathodes based on intercalation and conversion mechanism suffer from limited energy density. With regard to the high energy density system, the ideal materials to couple with Mg are O_2 and S. Mg/O_2 system exhibits a higher energy density of 3900 W h kg^{-1} than Li/O_2 if MgO is the final product, while the Mg/S system offers a theoretical energy density of 1722 W h kg^{-1} , both of which are over ten times higher than that of Chevrel phase (140 W h kg^{-1}).

5.1 $\text{Mg}-\text{O}_2$

Nonaqueous metal/oxygen batteries possess high theoretical energy densities (Fig. 44a).^{180–182} Chemistries based on alkali metals, such as Li/O_2 ,^{181,183–185} Na/O_2 ,^{181,186,187} and K/O_2 ,¹⁸⁸ are the most studied, while Mg/O_2 chemistry receives much less attention. In a Mg/O_2 cell, the half-reactions (2) and (3) could be anticipated at the gas electrode.¹⁸⁹ A Mg/O_2 cell with a MgO discharge product would exhibit theoretical volumetric and

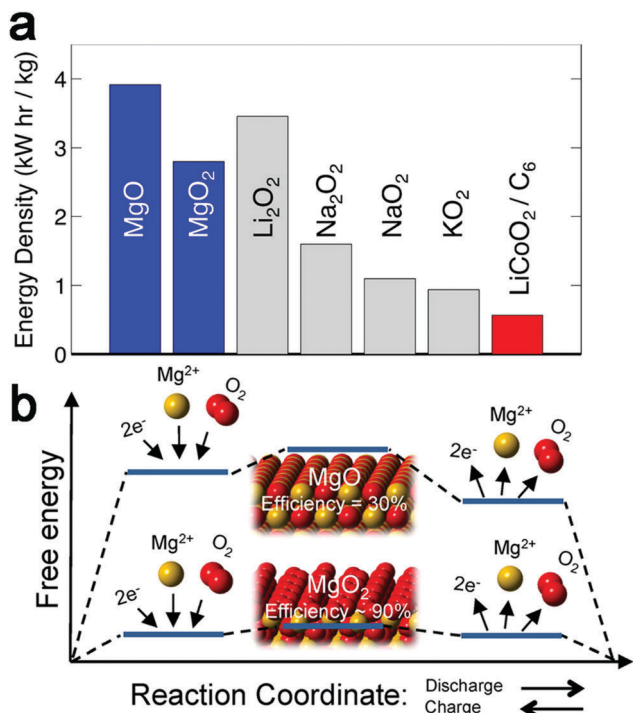
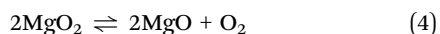
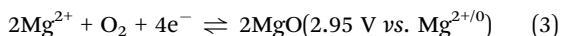
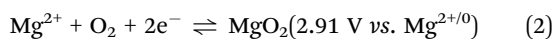


Fig. 44 (a) Theoretical specific energies (per mass of discharge product) of selected metal–oxygen chemistries (blue and gray bars) compared to Li-ion (red bar). (b) The free energy and efficiency of MgO₂- and MgO-based cells. Reproduced from ref. 182 with permission from American Chemical Society, Copyright 2016.

gravimetric energy densities of approximately 14 kW h L⁻¹ and 3.9 kW h kg⁻¹, respectively, surpassing Li/O₂ cells that discharge to Li₂O₂ (8.0 kW h L⁻¹ and 3.4 kW h kg⁻¹) (Fig. 44).¹⁸⁹



The mechanism of Li/O₂ system is well understood, in which oxygen reduction *via* a one-electron transfer is the most kinetically favorable and leads to the formation of LiO₂ (Li⁺ + O₂ + e⁻ → LiO₂).^{190,191} As LiO₂ is highly unstable, it further reacts to form lithium peroxide (Li₂O₂), either by a one-electron-transfer electrochemical process (LiO₂ + Li⁺ + e⁻ → Li₂O₂) or by disproportionation reaction (2LiO₂ → Li₂O₂ + O₂).¹⁸⁶ In contrast, the reaction mechanism for Mg/O₂ cell remains poorly understood.

Density functional theory calculations are employed to characterize the discharge/charge mechanisms on the surfaces of plausible discharge products, MgO and MgO₂.¹⁸² MgO₂-Based cells were predicted to be much more efficient: superoxide-terminated facets on MgO₂ crystallites enabled high round-trip efficiencies approaching 90% (Fig. 44b) and low overpotential, ranging from 0.11 to 0.18 V for discharge and 0.07 to 0.33 V for charge, which are slightly lower than 0.35 and 0.68 V for discharge and 0.2 and 0.4 V for charge with Li₂O₂ as the discharged product in the Li/O₂ system.¹⁹² In contrast, cells discharged to MgO exhibit low round-trip efficiencies (30%), which were rationalized by the presence of large thermodynamic hysteresis (the calculated discharge/charge voltages of 1.15/~4 V). This trend of superoxide-based cells exhibiting much lower overvoltage and higher round-trip efficiencies than those that discharge to a peroxide is consistent with the behavior of other metal oxygen batteries based on potassium¹⁸⁸ and sodium.^{186,193}

Experiments were performed to probe the discharged and charged products and verify the reaction mechanism. During the first cycle (Fig. 45a), the discharged product comprises roughly 70% MgO and 30% amorphous MgO₂ on a volumetric basis (Fig. 45b). This product was formed after electrochemical superoxide formation (eqn (2)), through chemical precipitation and disproportionation steps (eqn (4)).¹⁸⁹ The recharged positive electrode contains a small amount of residual MgO (Fig. 45c), suggesting that MgO₂ decomposes first during charging, followed by the slower MgO decomposition. Accordingly, the reaction pathway is concluded: during discharge, MgO₂ is firstly formed, followed by partial MgO₂ decomposition to MgO

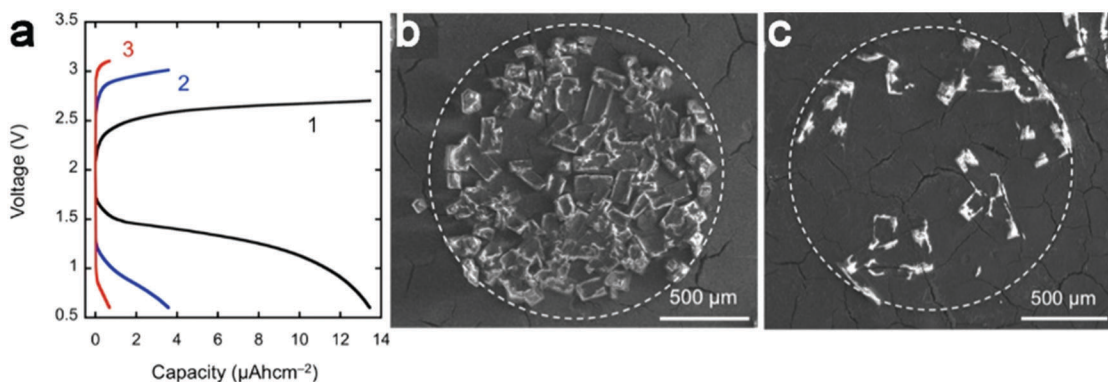


Fig. 45 (a) Discharge/recharge cycles for a room-temperature Mg/O₂ cell. SEM images of the positive-electrode surface on the side closest to the O₂ gas inlet: (b) an electrode after first discharge and (c) an electrode at the end of first recharge; the dashed circles represent boundaries of the regions that were directly exposed to O₂ through perforations in the Pt-coated current collector. Reproduced from ref. 189 with permission from American Chemical Society, Copyright 2015.

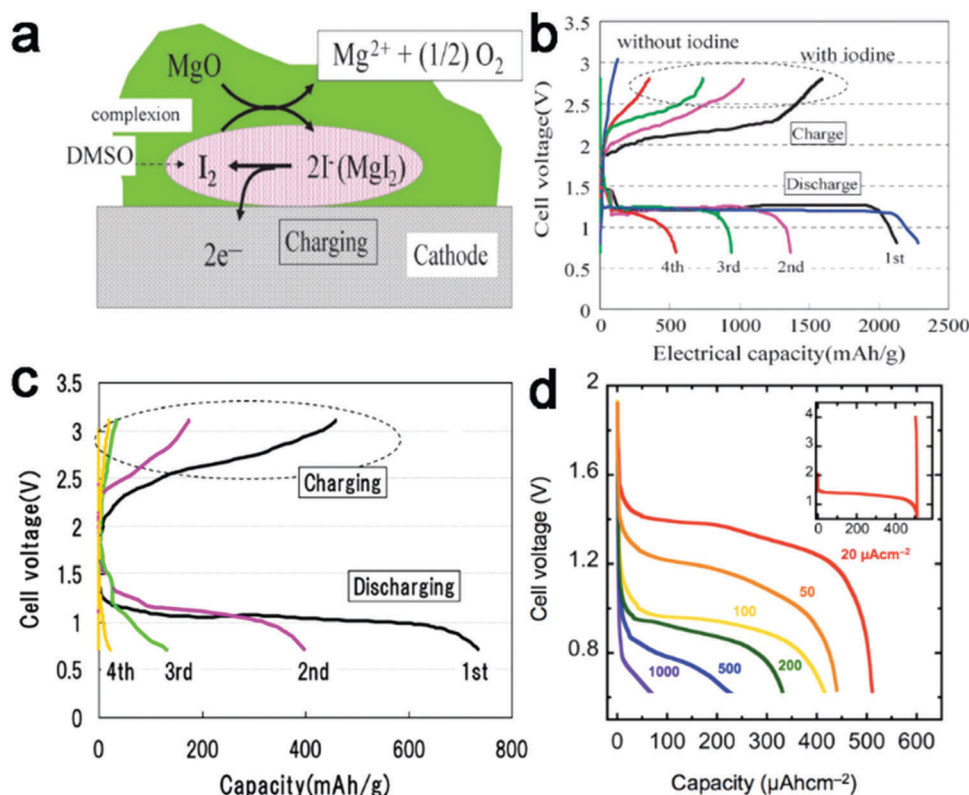


Fig. 46 (a) A proposed catalytic mechanism for the charging process. (b) Discharge–charge profiles of the non-aqueous Mg–O₂ battery with iodine (reproduced from ref. 194 with permission from Royal Society of Chemistry, Copyright 2013) and (c) with TEMPO + ClO₄⁻ incorporating PTMA in the cathode at 60°C, respectively. Reproduced from ref. 195 with permission from American Chemical Society, Copyright 2014. (d) Cell voltage vs. capacity for Mg/O₂ cells in MACC/DME at current densities ranging from 0.02 to 1 mA cm⁻² (superficial). The inset shows a typical discharge/charge cycle at 0.02 mA cm⁻². Reproduced from ref. 197 with permission from American Chemical Society, Copyright 2016.

through a disproportionation step; during charge, MgO₂ decomposes first, followed by more limited MgO decomposition.

According to the calculated and experimental results, several measures can be taken to improve the performance of the Mg/O₂ system. By using a redox mediator, MgO can be cycled reversibly *via* a liquid-phase reaction pathway, with lower over-voltage and higher capacities. Increasing the oxygen pressure and reducing the operation temperature can produce MgO₂ rather than MgO, resulting in much higher round-trip efficiency. Besides, the development of electrolytes with higher O₂ solubility and ionic conductivity could facilitate improvements in both the capacity and rate capability.

Based on the analysis above, iodine was added into Mg(ClO₄)₂–DMSO electrolyte to form iodine–DMSO complex by a charge-transfer interaction between DMSO and the bonds of the iodine molecule to catalyze the decomposition of MgO.¹⁹⁴ The catalytic cycle for the Mg–O₂ electrode was proposed by combining the decomposition of MgO with the I³⁻/3I⁻ redox couple (Fig. 46a). Mg–O₂ batteries with iodine showed a discharge capacity of 2131 mA h g⁻¹ and charge capacity of 1590 mA h g⁻¹ in the first cycle, in contrast to no charging behavior without iodine (Fig. 46b). Similarly, 2,2,6,6-tetramethylpiperidine-oxyl (TEMPO)–anion complex was also employed to catalyze the decomposition of MgO during the charge of Mg–oxygen battery, which exhibited rechargeable behavior over several

cycles (Fig. 46c).¹⁹⁵ Also, two dual redox mediators, 1,4-benzoquinone (BQ) and 5,10,15,20-tetraphenyl-21H,23H-porphine cobalt(II) (Co(II)TPP), were introduced to facilitate both the discharge and recharge processes of Mg–O₂ battery operations, showing promising results.¹⁹⁶

On the basis of the calculations, MgO₂-based cells can achieve high round-trip efficiencies and low thermodynamic hysteresis. The development of electrolytes with higher O₂ solubility facilitates MgO₂ production. Recently, a nonaqueous Mg/O₂ cell based on the all-inorganic magnesium aluminum chloride complex in dimethoxyethane electrolyte (MACC/DME) with higher O₂ solubility and ionic conductivity was demonstrated to exhibit a high discharge capacity (Fig. 46d).¹⁹⁷ However, poor rechargeability is observed, which is explained by the formation of an insulating film product, a mixture of Mg(ClO₄)₂ and MgCl₂ likely from the decomposition of electrolyte.¹⁹⁷ An additional impedance rises from an inert film formation on the Mg negative electrode, which can be attributed to the detrimental O₂ crossover.

Overall, despite some progress, there are several challenges for pursuing Mg/O₂ with substantial performance improvement: (1) the traditional ether-based electrolytes are not compatible with oxygen chemistry; (2) the dissolved O₂ in electrolytes will passivate the Mg anode; (3) redox mediators in electrolytes may react with the Mg anode.

5.2 Mg-S

As a high capacity cathode material (1675 mA h g^{-1}), sulfur has attracted intense interest in Li-S and Na-S systems.^{198–201} The combination of Mg with sulfur offers a theoretical capacity of 957 mA h g^{-1} with an average voltage of 1.77 V , corresponding to the energy density of 1722 W h kg^{-1} , over four times that of a commercial $\text{LiCoO}_2/\text{graphite}$ cell.²⁰² However, compared to the substantial progress in Li-S batteries, the study of Mg-S batteries is still in the early stage. One major challenge is to discover a suitable electrolyte that is chemically compatible to the electrophilic sulfur and capable of reversible Mg deposition/dissolution.²⁰³ In addition, similar to issues of Li/S batteries, dissolution of polysulfide and its shuttling effect, low active material utilization, and fast capacity fade are also expected.^{204,205} In order to solve these challenges, the discovery of suitable electrolytes and a fundamental understanding of the mechanism of Mg/S chemistry are of paramount importance.

Quasi-equilibrium discharge of Mg/S battery has revealed that sulfur reaction occurs through three consecutive steps. Stage (I) is elemental sulfur to long-chain polysulfide, showing a short slope at $2.5\text{--}1.5 \text{ V}$ ($\text{S}_8 + \text{Mg}^{2+} + 2\text{e}^- \rightarrow \text{MgS}_8$ ($2.5\text{--}1.5 \text{ V}$)). Stage (II) is chain-shortening of polysulfide, showing a long plateau at 1.5 V ($\text{MgS}_8 + 3\text{Mg}^{2+} + 6\text{e}^- + 4\text{MgS}_2$ (1.5 V)). Stage (III) is solid-state transition from short-chain polysulfide to MgS , showing another slope at $1.5\text{--}0.5 \text{ V}$ ($\text{MgS}_2 + \text{Mg}^{2+} + 2\text{e}^- \rightarrow \text{MgS}$ ($1.5\text{--}0.5 \text{ V}$)) (Fig. 47a).^{206,207} The reaction in stage (II) shows the fastest kinetics with small overpotential due to the synergetic effect of a fast surface reaction enabled by the dissolved polysulfide and the relative fast Mg^{2+} diffusion in the amorphous MgS_x , while stage (III) suffers from the slowest kinetics and high polarization because of solid-state magnesiation from MgS_2 to MgS (Fig. 47b–e).

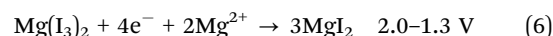
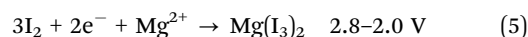
Several measures are applied to improve the performance of the Mg/S system: the use of new electrolytes and/or additives,^{206–210} cathode design,^{211,212} and Li^+ activating MgS_x species.²⁰² Progress has been achieved, but the reported electrochemical performance (discharge/charge curve, voltage hysteresis, *etc.*) has many discrepancies (Fig. 48). These discrepancies likely result from the

kinetics limitation of the magnesiation of sulfur, which can alter the discharge curve to different representations due to different kinetics at different stages. Factors that can affect kinetics include current, sulfur loading (S/C ratio), carbon host, and electrolyte chemistry. As for the large voltage hysteresis observed in some studies, the Mg anode overpotential is probably the main cause.²¹⁰

Significant progress has been achieved regarding electrolyte development and the fundamental understanding of the reaction mechanism. Yet, low sulfur loading (both sulfur/carbon ratio and sulfur/electrolyte ratio) and short cycling stability remain major challenges to convert Mg/S chemistry into usable technology. Some strategies from the Li/S system are translatable to the Mg/S system to tackle these challenges, *e.g.*, engineering the carbon host to achieve high sulfur loading, using highly concentrated electrolyte, and customized separators or special current collector (chemi- or physisorption) to suppress shuttle effect and achieve better cycling stability, as demonstrated by recent experimental studies.^{206,210} In addition, concerns regarding the passivation of Mg anode by dissolved sulfur species may not be a threat, as recent studies point out that SEI conducting Mg ion can also form on Mg anode.^{213,214}

5.3 Mg-I₂

To address the sluggish solid-state diffusion and the slow interfacial charge transfer discussed above, a two-phase (solid-liquid or liquid-solid) reaction pathway is considered a promising direction. I_2 is considered a good two-phase reaction cathode because I_2 and its partial reduction product, $\text{Mg(I}_3)_2$, have high solubility in ether-based electrolytes, while its final reduced product, MgI_2 , is insoluble.²¹⁵ The reaction mechanism for the magnesium/ I_2 batteries is proposed as follows:



A rechargeable Mg/ I_2 battery provided a high capacity of $\sim 200 \text{ mA h g}^{-1}$, an average voltage of 2.0 V at C/4 (Fig. 49a),

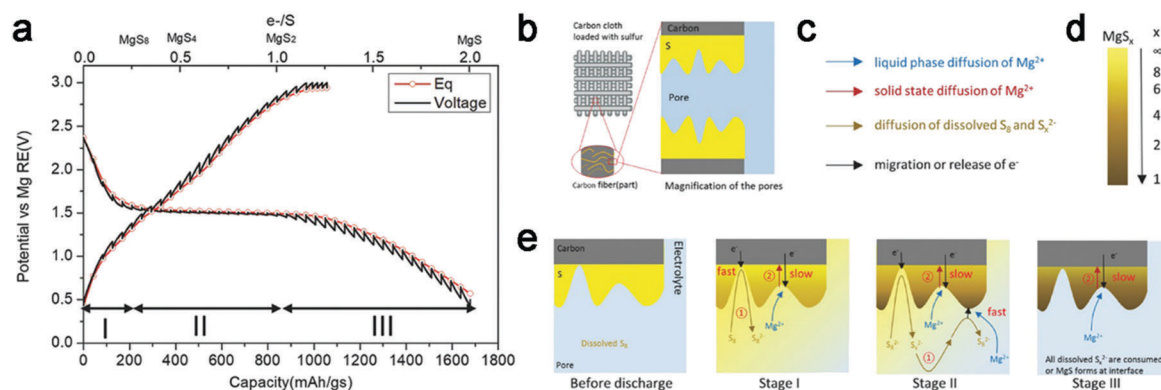


Fig. 47 (a) Thermodynamic equilibrium potential and three stages for sulfur reduction process. Schematic of sulfur reduction mechanism: (b) the structure of the carbon/sulfur composite cathode. (c) The kinetic processes during discharge. (d) Concentration of Mg in Mg-S binary compound. (e) Sulfur reduction mechanism. Reproduced from ref. 207 with permission from Wiley-VCH, Copyright 2017.

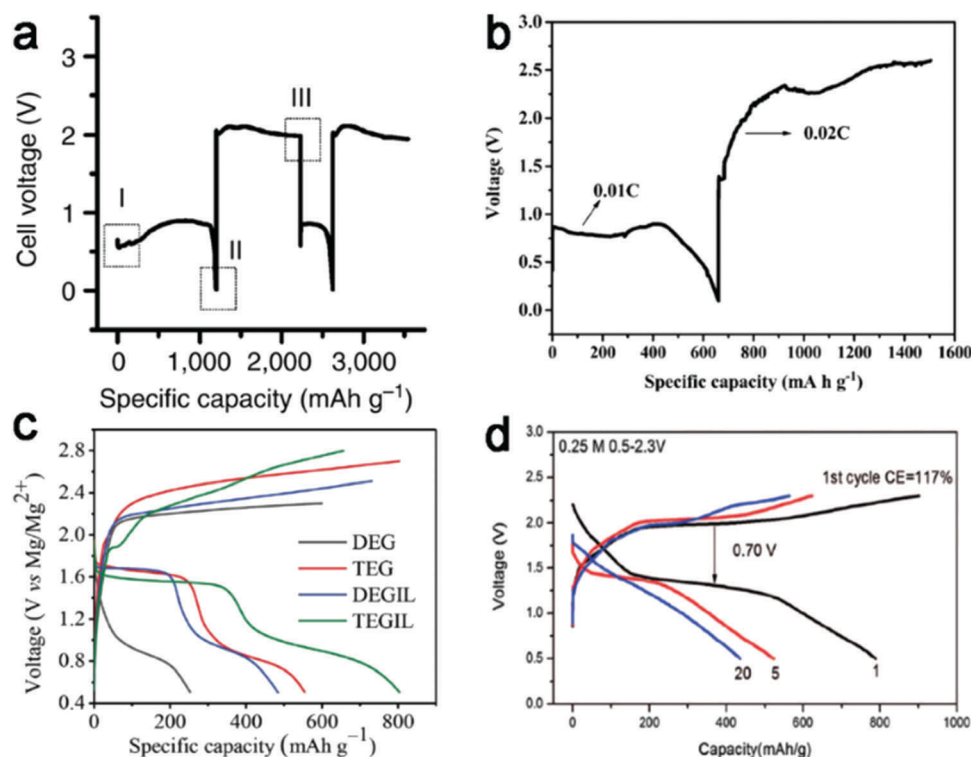


Fig. 48 (a) Discharge and charge of a Mg/S coin cell with the $[\text{Mg}_2(\mu\text{-Cl})_3\cdot 6\text{THF}][\text{HMDSAlCl}_3]$ electrolyte, in which the coulombic efficiency for Mg deposition/stripping is 100% at 50 and 25 μA . Reproduced from ref. 208 with permission from Springer Nature, Copyright 2011. (b) The first discharge and charge profiles of Mg/S cells with the $[\text{Mg}(\text{THF})_6][\text{AlCl}_4]_2$ electrolyte, in which the coulombic efficiency for Mg deposition/stripping is close to 100%. Reproduced from ref. 209 with permission from Wiley-VCH, Copyright 2016. (c) Initial discharge-charge curves of S/CMK400PEG composite using PVDF binder in diglyme (gray), tetraglyme (red), diglyme/PP14TFSI (blue), and tetraglyme/PP14TFSI (green). Reproduced from ref. 206 with permission from Wiley-VCH, Copyright 2014. (d) Voltage profiles in 0.25 M $\text{MgTFSI}_2/\text{MgCl}_2/\text{DME}$ electrolyte with coulombic efficiency for Mg deposition/stripping of 93%. Reproduced from ref. 210 with permission from Wiley-VCH, Copyright 2017.

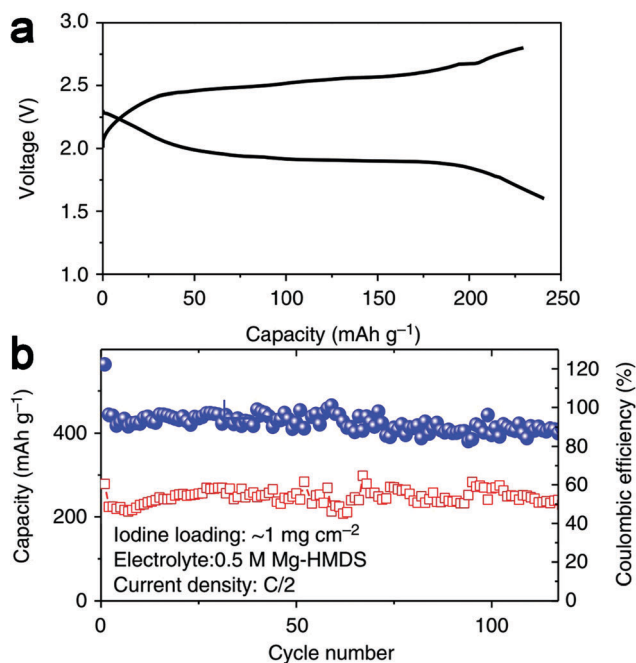


Fig. 49 (a) A typical discharge/charge curve of the Mg/I_2 battery with ACC/I_2 cathode. (b) Cycling stability of the Mg/I_2 battery at 0.5C (105.5 mA g^{-1}) with ACC/I_2 cathode. Reproduced from ref. 215 with permission from Springer Nature, Copyright 2017.

corresponding to 400 W h kg^{-1} , and excellent long-cycle stability with a capacity retention of 94.6% after 120 cycles at C/2 (Fig. 49b).²¹⁵ The rate capability of this battery is remarkable and demonstrates the potential of enhancing Mg battery performance by bypassing the solid state diffusion. The electrolyte is 2 M Mg-HMDS in tetraglyme, in which the coulombic efficiency for deposition/stripping of Mg is 94.5%, with the overpotential of 0.34 V. Therefore, the high coulombic efficiency and stable cycling performance for Mg/I_2 full cells are achieved with the excess of Mg.

The success of this proof-of-concept Mg/I_2 may open an avenue towards utilizing soluble redox couples not relying on solid-state Mg^{2+} diffusion for high-performance cathodes of RBMs.

6. Hybrid system

As discussed above, RBMs suffer much from the sluggish solid-state diffusion of Mg^{2+} , leading to the absence of viable cathodes, which has severely restricted the development of RBMs.²¹⁶ One potential approach is to circumvent the intercalation of clumsy Mg^{2+} by coupling the Mg metal anode with a mature LIB cathode in a mixed $\text{Mg}^{2+}/\text{Li}^+$ electrolyte. Thus, the hybrid battery chemistry simultaneously combines the high-capacity/high-voltage LIB

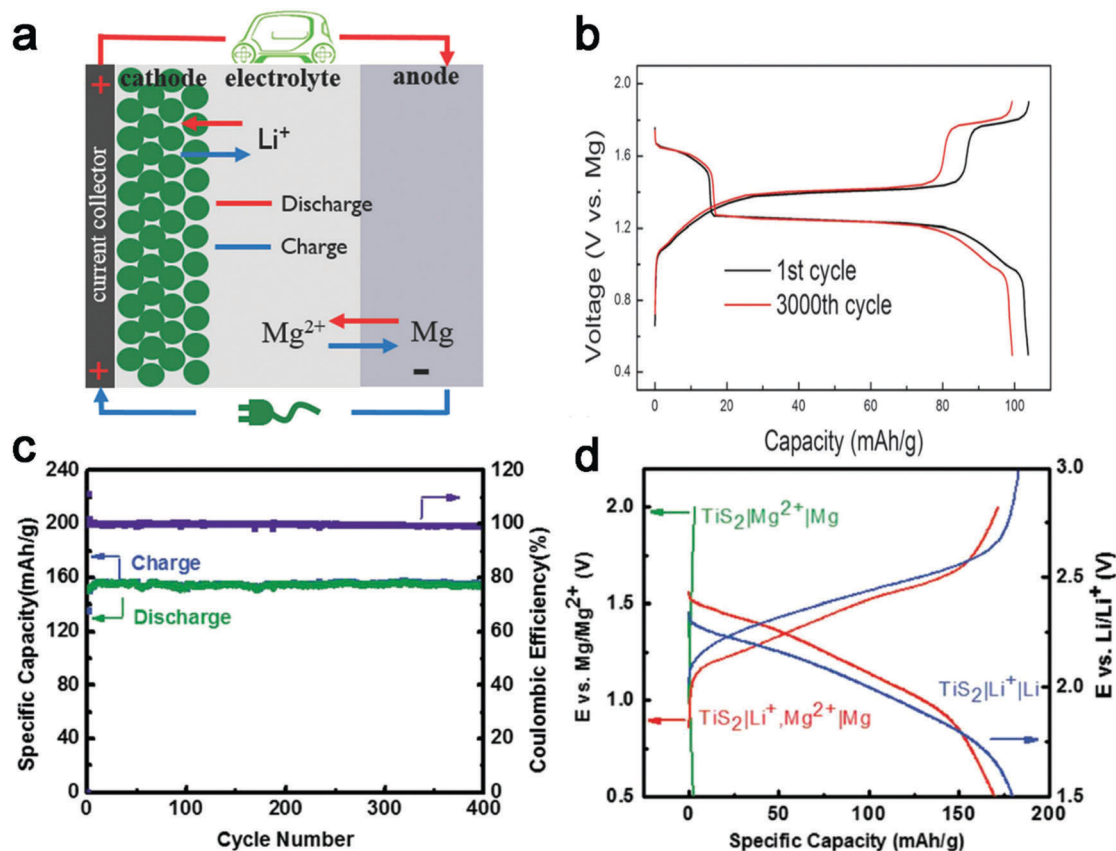


Fig. 50 (a) The operating mechanism of the hybrid Mg/Li ion battery. Reproduced from ref. 216 with permission from Wiley-VCH, Copyright 2015. (b) The charge–discharge profiles of Mo_6S_8 in hybrid Mg/Li ion battery for the first cycle and the 3000th cycle at 10C. Reproduced from ref. 229 with permission from Royal Society of Chemistry, Copyright 2014. (c) Cycling stability of a $\text{TiS}_2|\text{Li}^+, \text{Mg}^{2+}|\text{Mg}$ battery at $C/3$ ($1C = 240 \text{ mA h g}^{-1}$). (d) Discharge/charge curves of TiS_2 cathode in the $\text{TiS}_2|\text{Mg}^{2+}|\text{Mg}$ cell (1st cycle), $\text{TiS}_2|\text{Li}^+|\text{Li}$ cell (1st cycle), $\text{TiS}_2|\text{Li}^+, \text{Mg}^{2+}|\text{Mg}$ cell (2nd cycle) at 0.1C. Reproduced from ref. 216 with permission from Wiley-VCH, Copyright 2015.

cathodes, fast Li^+ intercalation, and the high-capacity/dendrite-free Mg anode.^{216,217} During discharge, Li^+ is inserted into cathodes and Mg is dissolved from Mg foil into the electrolyte, while during charge, Li^+ is extracted from lithiated cathodes and Mg is deposited onto Mg foil (Fig. 50a).

Several intercalation compounds have been used for this hybrid battery concept (Fig. 50).^{216–229} In addition to hybrid MLIBs, hybrid $\text{Mg}^{2+}/\text{Na}^+$ and $\text{Mg}^{2+}/\text{K}^+$ ion batteries are also reported based on the similar reaction mechanism with MLIBs, showing some progress.^{230–236} They all show significant performance improvement compared to a pure Mg system, which is mainly attributed to the insertion of Li^+ . To unravel the origin of the electrochemical properties of hybrid systems at the atomistic and macroscopic levels, theoretical and experimental investigations were conducted.²³⁷ Energetically preferable occupation sites for the first ion (either Mg^{2+} or Li^+) were calculated in the primitive Mo_6S_8 crystal structure at multiple stages of discharge, and based on that, various paths of Mg^{2+} and Li^+ could be predicted (Fig. 51).²³⁷ The insertion chemistry at the cathode strongly depends on the Li^+ activity in the electrolyte. Increasing Li^+ activity (α_{Li^+}) leads to thermodynamically more favorable lithiation in Mo_6S_8 rather than magnesiation.

The chemical composition of the deposit in the $\text{Mg}^{2+}/\text{Li}^+$ mixed-ion electrolyte was examined.^{216,238} All XRD peaks of the

deposition can be assigned to Mg, and no peaks can be indexed to Li or Mg–Li alloy, which was further verified by electron energy loss spectroscopy (EELS). Although Li^+ might electrochemically react with the deposited Mg to form Li–Mg alloy in the potential range of Mg deposition, results of several experimental works confirm that the deposition was pure magnesium with no detectable lithium.^{216,238}

Despite the significantly enhanced kinetics due to Li insertion in the hybrid system, an intrinsic limitation exists for this concept. In the traditional rechargeable battery, electrolyte only functions as an ion conductor, so its weight does not compromise the overall energy density of the full cell. In the hybrid system, however, the electrolyte also works as an ion reservoir, *i.e.*, storing the Li^+ needed for cathode intercalation. For this reason, when evaluating the energy density of hybrid systems, it is necessary to consider the amount of electrolyte to make a fair comparison.

In summary, great demonstrations of hybrid systems have been shown in literature using different electrolytes and intercalation compounds. Nevertheless, the influence of electrolyte amount needs to be thoroughly studied to justify the potential of this concept. In addition, the influence of Li intercalation on Mg diffusion also needs to be examined, as co-intercalation

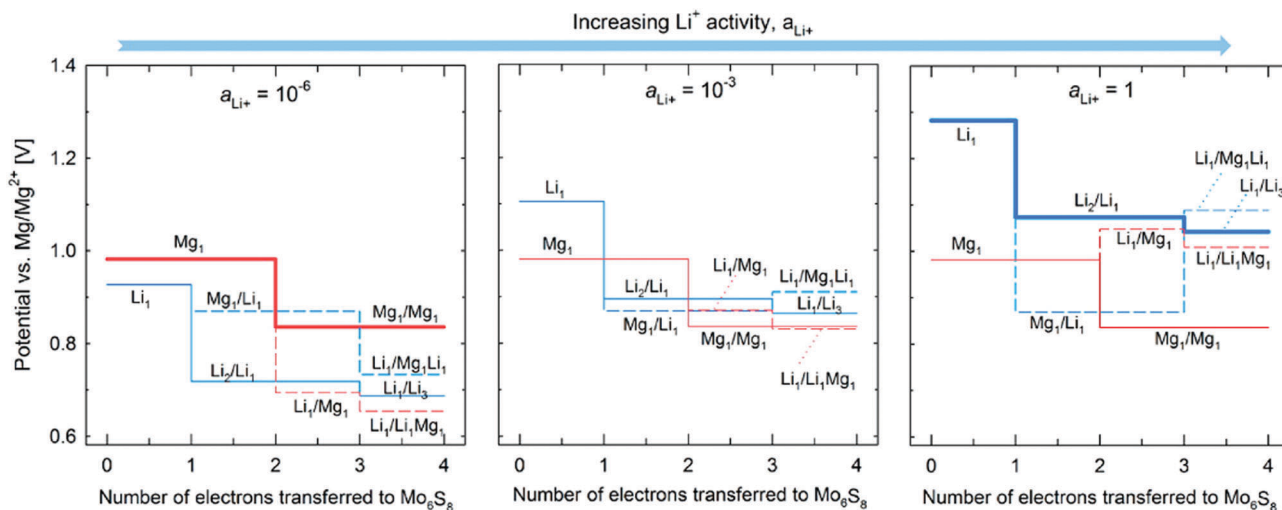


Fig. 51 Lithiation and magnesiation potentials of Mo_6S_8 (vs. Mg/Mg^{2+}) at different Li^+ activity levels (a_{Li^+}) determined by combining DFT energies with the Nernst equation. Mixed-insertion paths where Li^+ and Mg^{2+} occupy different sites in the same Mo_6S_8 host are shown as dashed lines. Full magnesiation and full lithiation paths are shown in bold. Reproduced from ref. 237 with permission from American Chemical Society, Copyright 2014.

could have a positive effect on Mg diffusion, which has never been investigated before.

7. Conclusion and perspective

The dawn of the 21st century has witnessed the great success of LIBs, which now power a spectrum of applications in our daily life, including portable devices, power tools, and EVs. As LIBs approach their limit, new technologies are inevitable to meet the growing demands on energy storage. Despite LIBs continuing to dominate many applications due to their good combination of several performance indexes, including energy density, power density and cycling stability, we believe other chemistries will become more competitive in certain applications where one or two performance indexes are critical. The rechargeable magnesium battery, coupling the high volumetric capacity of Mg metal with the safety benefit due to lack of dendrite formation, is highly suitable for applications where volumetric energy density is critical, *e.g.*, portable electronics.

In this review, we have reviewed the latest progress of RMB cathodes, generally categorized by intercalation compounds, conversion materials, elemental redox chemistry, and new mechanisms/concepts, including water co-intercalation and hybrid systems (Table 1).

Among these, intercalation compounds (with 3D, 2D, and 1D diffusion channel) are the most studied. Charge transfer kinetics and Mg diffusion in solids, especially the latter, are limiting the performance of intercalation compounds. Mg diffusion in the intercalation compounds highly depends on their structure and chemistry, manifested in (1) connectivity between sites; (2) sizes of the diffusion channel/cavity and intercalant; and (3) interaction strength between the intercalant and host structure. Chevrel phase shows the best kinetics

because of the highly delocalized electrons effectively shielding the charge of Mg^{2+} , along with the facilitated charge transfer due to the catalytic effect of surface Mo atoms. For a given structure, the chemistry of compounds plays the determining role. Taking spinel compounds as an example, in which Mg migrates along the tet \rightarrow oct \rightarrow tet pathway, both experiments and calculations show sulfides have better kinetics than oxides due to the lower migration barriers of Mg ion, because the larger sulfur anion leads to increasing size of the diffusion channel and the smaller electronegativity induces less interaction between Mg^{2+} and host anion lattices. Such structural and chemical effects on intercalation kinetics are generalizable to other intercalation compounds, including layered structures.

For polyanions, due to the thermodynamic instability of magnesiation products and high Mg^{2+} migration barriers, magnesiation of olivine phosphate is prohibited by surface amorphization. While several reports on olivine silicate (MgFeSiO_4 , MgCoSiO_4 *etc.*) achieved reversible Mg^{2+} intercalation, it needs to be validated by more experimental and theoretical investigations. With the potential of good Mg^{2+} diffusion kinetics and high energy density, the possible utility of olivine silicates is worth pursuing further.

To improve the kinetics of Mg intercalation, measures can be taken, including: (1) choosing structures with large diffusion channels; (2) replacing anions with soft ones (S or Se) or incorporating monovalent anions (F, Cl *etc.*) to decrease the interaction between hosts and intercalants; (3) utilizing mixed transition metal ions (Mo, V, *etc.*) in inorganic compounds to enhance charge redistribution brought by Mg^{2+} intercalation; (4) reducing particle sizes to decrease the Mg^{2+} migration length; and (5) elevating temperature to improve the mobility of Mg^{2+} . In addition, greater understanding of the charge transfer process at the cathode/electrolyte interface is necessary for engineering the surface of intercalation compounds for better interfacial reaction kinetics. Further systematic

Table 1 Summary of cathodes for rechargeable Mg batteries

		Structure	Materials	Diffusivity (meV)	Potential (V)	Capacity (mA h g ⁻¹)	Ref.
Intercalation	3D	Chevrel phase Spinel	Mo ₆ S ₈	360a	0.99, ^a 1–1.3	120	7, 14 and 18
			Mn ₂ O ₄	~ 650–850 ^a	2.86, ^a 2.9	270 ^a	13 and 29
			Ti ₂ S ₄	615, ^a 550	0.89, ^a 1.2	216, ^a 200	7 and 24
	2D	Layered sulfide/ selenide (trigonal)	TiS ₂	1160 ^a	~ 1	115	22 and 33
			TiSe ₂		~ 1	130, ^a 110	38
			VSe ₂		~ 1	110	38
			TiS ₃	292–698 ^a	~ 1.2	83.7	46 and 49
		Monoclinic Layered oxide	α-V ₂ O ₅	975–1120 ^a	2.21, ^a 2.35	150	57, 61 and 65
			δ-V ₂ O ₅	600–760 ^a	2.56		61 and 65
			α-MoO ₃	880 ^a	1.8	210	57 and 77
			MoO _{2.8} F _{0.2}	490 ^a		70	77 and 84
	1D	Olivine	Mo _{2.5+y} VO _{9+δ}		~ 2.1	235	89
			FePO ₄	580–1025 ^a	~ 2	12	100
			Silicate	740–770 ^a	~ 2.1–4		97 and 101
		Open framework	Prussian blue analogues (PBAs)		2.9	80	128
			Fullerene				
Conversion			C60		1.2–1.6	50	115
		Oxide	α-MnO ₂		~ 2	80	142, 143 and 146
			δ-MnO ₂			150	149
		Chalcogenide	CuS		1.3–1.6	200	155 and 156
			Cu ₂ Se		~ 1.2	230	163
		Chloride	AgCl		2	178	164
			DMBQ		~ 2	100	171
		Organic materials	PAQ		1.7 V	150	175
			14PAQ		1.6–1.7	105	173
Water co-intercalation			α-V ₂ O ₅			260	60
			Birnessite MnO ₂		2.8	231.1	150
Elemental redox chemistry			Mg–O ₂		~ 2.9 ^a	~ 1300 ^a	182 and 189
			Mg–S		1.77 ^a	957, ^a 600	206 and 210
			Mg–I		2	200	215
Hybrid system			Mg/Li ion batteries				216 and 229

^a Calculated results.

investigation is also required on oxides (λ -MnO₂) and poly-anions to clear confusions due to some inconsistent results in the literature.

Many conversion cathodes are being investigated, including transition metal oxides (MnO₂ *etc.*), sulfides and selenides (CuS, Cu₂Se *etc.*), and chloride (AgCl *etc.*). Due to the thermodynamic instability of the magnesiation products, amorphization occurs on the surface of various manganese oxides after initial intercalation, despite the existence of open tunnel for diffusion in their structures. Such amorphous film prevents Mg²⁺ further intercalation, causing low capacity and significant irreversibility. Amorphization does not occur in layered oxides (V₂O₅, MoO₃ *etc.*), and whether it will happen in other transition metal oxides with open tunnels needs to be further investigated. Sulfides (TiS₂, Ti₂S₄, and TiS₃ *etc.*) and selenides (TiSe₂, WSe₂ *etc.*) with layered and spinel structure have been reported to undergo an intercalation reaction, while CuS and Cu₂Se without Mg²⁺ diffusion channels demonstrate a displacement reaction, which enables fast magnesiation kinetics as a result of the high mobility of copper ions. Such great performance suggests that displacement reaction could be a promising direction to explore conversion cathode materials with fast kinetics. Chlorides undergo a solid–liquid two-phase reaction

during magnesiation because the formed MgCl₂ can dissolve into the electrolyte. The two-phase reaction can significantly increase the kinetics due to circumvention of solid state Mg diffusion, which comes at the cost of fast capacity fading. Such ultrafast kinetics permits chloride suitable for special applications requiring high rates.

Organic materials (DMBQ, 26PAQ, 14PAQ, and PAQS) are reported to show faster kinetics than inorganic compounds due to the weak interaction between Mg²⁺ and organic molecules. The severe dissolution and low electronic conductivity are limiting their performance, which can be mitigated by developing new electrolytes, organic polymerization, and improving the structure stability.

Mg/O₂ and Mg/S can provide high theoretical capacity and energy density. Mg/O₂ suffers from high overpotential and irreversibility due to the inert discharged products (MgO). Some redox mediators are introduced to catalyze the decomposition of MgO, which can improve the reversibility of Mg/O₂ systems, but the reaction with Mg metal anode needs to be carefully investigated. Methods can be taken to enhance the reversibility, including increasing oxygen pressure, reducing operation temperature, and developing electrolytes with higher O₂ solubility to produce more reversible MgO₂, *etc.* For the Mg/S

system, significant progress regarding electrolyte development has been made. The fundamental understanding of reaction mechanisms has been achieved, in which a three-stage reaction mechanism corresponding to long chain polysulfide formation, chain shortening to MgS_2 , and formation of MgS has been revealed, with the kinetics and thermodynamics of each stage carefully investigated. Yet, low sulfur loading and short cycling stability remain major challenges to convert this promising chemistry into usable technology. To address these issues, lessons can be learned from Li/S chemistry, which includes the use of additives, highly concentrated electrolyte, customized separators and special current collector (chemi- or physisorption).

Water co-intercalation has achieved improved magnesiation kinetics in some oxides ($\alpha\text{-V}_2\text{O}_5$, xerogel V_2O_5 , and birnessite MnO_2). Proton cycling has been widely demonstrated. Some fundamental questions remain to be addressed: the amount of intercalated protons; whether hydrated Mg^{2+} is cycled; how co-intercalation improves the kinetics by increasing Mg^{2+} mobility or reducing the desolvation energy.

Regarding hybrid systems, prototype cells have been demonstrated to work reversibly with different intercalation compounds. Further investigations need to examine carefully how electrolyte amount compromises the energy density of the system, given that the electrolyte needs to store sufficient ions for hybrid systems to work. In addition, the influence of Li intercalation on Mg diffusion needs to be clarified. Considering the limited energy density, hybrid systems may be a good choice in certain applications where safety and fast discharge and charge are the priority.

Compared with the success of LIBs, rechargeable Mg batteries are still at the infant stage. Despite some remaining challenges, the last decade has witnessed significant progress in the understanding of reaction mechanisms and kinetic limitations of many cathode materials, providing precious insights and guidelines for future research. Fortunately, the vast chemical space of new structures and chemistries remains unexplored, which provides possibilities for feasible cathodes with better kinetics and higher energy density. We hope this review will act as a call for more efforts into rechargeable magnesium batteries, an emerging and exciting new direction in energy storage research, especially in cathode materials.

Conflicts of interest

The authors declare no conflict of interest.

Acknowledgements

The authors acknowledge the support from the Army Research Office (Grant number: W911NF-15-1-0187) and Nanostructures for Electrical Energy Storage (NEES), an Energy Frontier Research Center funded by the US Department of Energy, Office of Science, Basic Energy Sciences, under Award number DESC0001160. This work was also supported by the National Natural Science Foundation of China (Grant no. 51302079) and Hunan Provincial

Innovation Foundation for Postgraduate (no. CX2016B120). M. Mao's fellowship was supported by China Scholarship Council (grant no. 201606130050). The authors thank Mr Zengxi Wei from Hunan University for the help on schematic illustration.

References

- 1 M. Armand and J. M. Tarascon, *Nature*, 2008, **451**, 652.
- 2 M. S. Whittingham, *Chem. Rev.*, 2014, **114**, 11414–11443.
- 3 B. Scrosati, *Electrochim. Acta*, 2000, **45**, 2461–2466.
- 4 H. D. Yoo, I. Shterenberg, Y. Gofer, G. Gershinsky, N. Pour and D. Aurbach, *Energy Environ. Sci.*, 2013, **6**, 2265–2279.
- 5 P. Canepa, G. Sai Gautam, D. C. Hannah, R. Malik, M. Liu, K. G. Gallagher, K. A. Persson and G. Ceder, *Chem. Rev.*, 2017, **117**, 4287–4341.
- 6 J. Muldoon, C. B. Bucur and T. Gregory, *Chem. Rev.*, 2014, **114**, 11683–11720.
- 7 M. Liu, A. Jain, Z. Rong, X. Qu, P. Canepa, R. Malik, G. Ceder and K. A. Persson, *Energy Environ. Sci.*, 2016, **9**, 3201–3209.
- 8 M. S. Whittingham, *Chem. Rev.*, 2004, **104**, 4271–4302.
- 9 J. B. Goodenough and Y. Kim, *Chem. Mater.*, 2010, **22**, 587–603.
- 10 H. Gwon, S.-W. Kim, Y.-U. Park, J. Hong, G. Ceder, S. Jeon and K. Kang, *Inorg. Chem.*, 2014, **53**, 8083–8087.
- 11 R. Malik, D. Burch, M. Bazant and G. Ceder, *Nano Lett.*, 2010, **10**, 4123–4127.
- 12 Z. Rong, R. Malik, P. Canepa, G. Sai Gautam, M. Liu, A. Jain, K. Persson and G. Ceder, *Chem. Mater.*, 2015, **27**, 6016–6021.
- 13 M. Liu, Z. Rong, R. Malik, P. Canepa, A. Jain, G. Ceder and K. A. Persson, *Energy Environ. Sci.*, 2015, **8**, 964–974.
- 14 D. Aurbach, Z. Lu, A. Schechter, Y. Gofer, H. Gizbar, R. Turgeman, Y. Cohen, M. Moshkovich and E. Levi, *Nature*, 2000, **407**, 724.
- 15 E. Levi, Y. Gofer, Y. Vestfried, E. Lancry and D. Aurbach, *Chem. Mater.*, 2002, **14**, 2767–2773.
- 16 E. Lancry, E. Levi, Y. Gofer, M. Levi, G. Salitra and D. Aurbach, *Chem. Mater.*, 2004, **16**, 2832–2838.
- 17 A. Mitelman, M. D. Levi, E. Lancry, E. Levi and D. Aurbach, *Chem. Commun.*, 2007, 4212–4214.
- 18 C. Ling and K. Suto, *Chem. Mater.*, 2017, **29**, 3731–3739.
- 19 E. Levi, E. Lancry, A. Mitelman, D. Aurbach, O. Isnard and D. Djurado, *Chem. Mater.*, 2006, **18**, 3705–3714.
- 20 J. K. Burdett and J. H. Lin, *Inorg. Chem.*, 1982, **21**, 5–10.
- 21 F. Thole, L. F. Wan and D. Prendergast, *Phys. Chem. Chem. Phys.*, 2015, **17**, 22548–22551.
- 22 X. Sun, P. Bonnick and L. F. Nazar, *ACS Energy Lett.*, 2016, **1**, 297–301.
- 23 M. D. Levi, E. Lancry, H. Gizbar, Z. Lu, E. Levi, Y. Gofer and D. Aurbach, *J. Electrochem. Soc.*, 2004, **151**, A1044–A1051.
- 24 X. Sun, P. Bonnick, V. Duffort, M. Liu, Z. Rong, K. A. Persson, G. Ceder and L. F. Nazar, *Energy Environ. Sci.*, 2016, **9**, 2273–2277.

- 25 L. F. Wan, B. R. Perdue, C. A. Appleby and D. Prendergast, *Chem. Mater.*, 2015, **27**, 5932–5940.
- 26 Y. Cheng, L. R. Parent, Y. Shao, C. Wang, V. L. Sprenkle, G. Li and J. Liu, *Chem. Mater.*, 2014, **26**, 4904–4907.
- 27 S. U. Kim, B. Perdue, C. A. Appleby and V. Srinivasan, *J. Electrochem. Soc.*, 2016, **163**, A1535–A1542.
- 28 Z. Feng, X. Chen, L. Qiao, A. L. Lipson, T. T. Fister, L. Zeng, C. Kim, T. Yi, N. Sa, D. L. Proffitt, A. K. Burrell, J. Cabana, B. J. Ingram, M. D. Biegalski, M. J. Bedzyk and P. Fenter, *ACS Appl. Mater. Interfaces*, 2015, **7**, 28438–28443.
- 29 C. Kim, P. J. Phillips, B. Key, T. Yi, D. Nordlund, Y.-S. Yu, R. D. Bayliss, S.-D. Han, M. He, Z. Zhang, A. K. Burrell, R. F. Klie and J. Cabana, *Adv. Mater.*, 2015, **27**, 3377–3384.
- 30 M. Cabello, R. Alcantara, F. Nacimiento, G. Ortiz, P. Lavela and J. L. Tirado, *CrystEngComm*, 2015, **17**, 8728–8735.
- 31 P. Bonnicks, X. Sun, K.-C. Lau, C. Liao and L. F. Nazar, *J. Phys. Lett.*, 2017, **8**, 2253–2257.
- 32 V. V. Kulish, D. Koch and S. Manzhos, *Phys. Chem. Chem. Phys.*, 2017, **19**, 6076–6081.
- 33 A. Emly and A. Van der Ven, *Inorg. Chem.*, 2015, **54**, 4394–4402.
- 34 D. Aurbach, G. S. Suresh, E. Levi, A. Mitelman, O. Mizrahi, O. Chusid and M. Brunelli, *Adv. Mater.*, 2007, **19**, 4260–4267.
- 35 M. D. Levi, E. Lanci, E. Levi, H. Gizbar, Y. Gofer and D. Aurbach, *Solid State Ionics*, 2005, **176**, 1695–1699.
- 36 G. S. Suresh, M. D. Levi and D. Aurbach, *Electrochim. Acta*, 2008, **53**, 3889–3896.
- 37 E. Levi, M. D. Levi, O. Chasid and D. Aurbach, *J. Electroceram.*, 2009, **22**, 13–19.
- 38 Y. Gu, Y. Katsura, T. Yoshino, H. Takagi and K. Taniguchi, *Sci. Rep.*, 2015, **5**, 12486.
- 39 G. Ceder, Y. M. Chiang, D. R. Sadoway, M. K. Aydinol, Y. I. Jang and B. Huang, *Nature*, 1998, **392**, 694.
- 40 K. Taniguchi, T. Yoshino, Y. Gu, Y. Katsura and H. Takagi, *J. Electrochem. Soc.*, 2015, **162**, A198–A202.
- 41 A. Doron, W. Idit, G. Yosef and L. Elena, *Chem. Rec.*, 2003, **3**, 61–73.
- 42 C. M. Fang, R. A. de Groot and C. Haas, *Phys. Rev. B: Condens. Matter Mater. Phys.*, 1997, **56**, 4455–4463.
- 43 M. T. Czyżyk, R. Potze and G. A. Sawatzky, *Phys. Rev. B: Condens. Matter Mater. Phys.*, 1992, **46**, 3729–3735.
- 44 M. Saubanière, M. B. Yahia, S. Lebègue and M. L. Doublet, *Nat. Commun.*, 2014, **5**, 5559.
- 45 B. Liu, T. Luo, G. Mu, X. Wang, D. Chen and G. Shen, *ACS Nano*, 2013, **7**, 8051–8058.
- 46 T. Kouji, G. Yunpeng, K. Yukari, Y. Takafumi and T. Hidenori, *Appl. Phys. Express*, 2016, **9**, 011801.
- 47 J. Kang, H. Sahin, H. D. Ozaydin, R. T. Senger and F. M. Peeters, *Phys. Rev. B: Condens. Matter Mater. Phys.*, 2015, **92**, 075413.
- 48 E. Guilmeau, D. Berthebaud, P. R. N. Misse, S. Hébert, O. I. Lebedev, D. Chateigner, C. Martin and A. Maignan, *Chem. Mater.*, 2014, **26**, 5585–5591.
- 49 M. Arsentev, A. Missyul, A. V. Petrov and M. Hammouri, *J. Phys. Chem. C*, 2017, **121**, 15509–15515.
- 50 Y. Liang, H. D. Yoo, Y. Li, J. Shuai, H. A. Calderon, F. C. Robles Hernandez, L. C. Grabow and Y. Yao, *Nano Lett.*, 2015, **15**, 2194–2202.
- 51 J. Desilvestro and O. Haas, *J. Electrochem. Soc.*, 1990, **137**, 5C–22C.
- 52 H. Yuan, L. Jiao, J. Cao, X. Liu, M. Zhao and Y. Wang, *J. Mater. Sci. Technol.*, 2004, **20**, 41–45.
- 53 R. Wang, C.-C. Chung, Y. Liu, J. L. Jones and V. Augustyn, *Langmuir*, 2017, **33**, 9314–9323.
- 54 M. E. Spahr, P. Novák, O. Haas and R. Nesper, *J. Power Sources*, 1995, **54**, 346–351.
- 55 P. Novák and J. Desilvestro, *J. Electrochem. Soc.*, 1993, **140**, 140–144.
- 56 W.-h. Yu, D.-z. Wang, B. Zhu, S.-j. Wang and L.-x. Xue, *Solid State Commun.*, 1987, **61**, 271–273.
- 57 G. Gershinsky, H. D. Yoo, Y. Gofer and D. Aurbach, *Langmuir*, 2013, **29**, 10964–10972.
- 58 B. Zhou, H. Shi, R. Cao, X. Zhang and Z. Jiang, *Phys. Chem. Chem. Phys.*, 2014, **16**, 18578–18585.
- 59 S. H. Lee, R. A. DiLeo, A. C. Marschillok, K. J. Takeuchi and E. S. Takeuchi, *ECS Electrochem. Lett.*, 2014, **3**, A87–A90.
- 60 N. Sa, H. Wang, D. L. Proffitt, A. L. Lipson, B. Key, M. Liu, Z. Feng, T. T. Fister, Y. Ren, C.-J. Sun, J. T. Vaughey, P. A. Fenter, K. A. Persson and A. K. Burrell, *J. Power Sources*, 2016, **323**, 44–50.
- 61 G. Sai Gautam, P. Canepa, A. Abdellahi, A. Urban, R. Malik and G. Ceder, *Chem. Mater.*, 2015, **27**, 3733–3742.
- 62 A. Parija, D. Prendergast and S. Banerjee, *ACS Appl. Mater. Interfaces*, 2017, **9**, 23756–23765.
- 63 A. Mukherjee, N. Sa, P. J. Phillips, A. Burrell, J. Vaughey and R. F. Klie, *Chem. Mater.*, 2017, **29**, 2218–2226.
- 64 A. Parija, Y. Liang, J. L. Andrews, L. R. De Jesus, D. Prendergast and S. Banerjee, *Chem. Mater.*, 2016, **28**, 5611–5620.
- 65 G. S. Gautam, P. Canepa, R. Malik, M. Liu, K. Persson and G. Ceder, *Chem. Commun.*, 2015, **51**, 13619–13622.
- 66 G. Sai Gautam, P. Canepa, W. D. Richards, R. Malik and G. Ceder, *Nano Lett.*, 2016, **16**, 2426–2431.
- 67 N. Sa, T. L. Kinnibrugh, H. Wang, G. Sai Gautam, K. W. Chapman, J. T. Vaughey, B. Key, T. T. Fister, J. W. Freeland, D. L. Proffitt, P. J. Chupas, G. Ceder, J. G. Baren, I. D. Bloom and A. K. Burrell, *Chem. Mater.*, 2016, **28**, 2962–2969.
- 68 V. Petkov, P. N. Trikalitis, E. S. Bozin, S. J. L. Billinge, T. Vogt and M. G. Kanatzidis, *J. Am. Chem. Soc.*, 2002, **124**, 10157–10162.
- 69 C. Delmas, H. Cognac-Auradou, J. M. Cocciantelli, M. Ménétrier and J. P. Doumerc, *Solid State Ionics*, 1994, **69**, 257–264.
- 70 T. Yao, Y. Oka and N. Yamamoto, *J. Mater. Chem.*, 1992, **2**, 337–340.
- 71 S. Tepavcevic, H. Xiong, V. R. Stamenkovic, X. Zuo, M. Balasubramanian, V. B. Prakapenka, C. S. Johnson and T. Rajh, *ACS Nano*, 2012, **6**, 530–538.
- 72 P. Novák, R. Imhof and O. Haas, *Electrochim. Acta*, 1999, **45**, 351–367.
- 73 W. Li, F. Cheng, Z. Tao and J. Chen, *J. Phys. Chem. B*, 2006, **110**, 119–124.
- 74 J. Światowska-Mrowiecka, S. de Diesbach, V. Maurice, S. Zanna, L. Klein, E. Briand, I. Vickridge and P. Marcus, *J. Phys. Chem. C*, 2008, **112**, 11050–11058.

- 75 T. S. Sian and G. B. Reddy, *Appl. Surf. Sci.*, 2004, **236**, 1–5.
- 76 T. S. Sian and G. B. Reddy, *Solid State Ionics*, 2004, **167**, 399–405.
- 77 L. F. Wan, J. T. Incorvati, K. R. Poeppelmeier and D. Prendergast, *Chem. Mater.*, 2016, **28**, 6900–6908.
- 78 T. S. Sian, G. B. Reddy and S. M. Shivaprasad, *Electrochem. Solid-State Lett.*, 2006, **9**, A120–A122.
- 79 S. S. Tarsame, B. R. Gade and M. S. Sonnada, *Jpn. J. Appl. Phys.*, 2004, **43**, 6248.
- 80 J. W. Bullard and R. L. Smith, *Solid State Ionics*, 2003, **160**, 335–349.
- 81 C. Julien and G. A. Nazri, *Solid State Ionics*, 1994, **68**, 111–116.
- 82 C. Julien, O. Mohammad Hussain, L. El-Farh and M. Balkanski, *Solid State Ionics*, 1992, **53–56**, 400–404.
- 83 T. S. Arthur, R. Zhang, C. Ling, P.-A. Glans, X. Fan, J. Guo and F. Mizuno, *ACS Appl. Mater. Interfaces*, 2014, **6**, 7004–7008.
- 84 J. T. Incorvati, L. F. Wan, B. Key, D. Zhou, C. Liao, L. Fuoco, M. Holland, H. Wang, D. Prendergast, K. R. Poeppelmeier and J. T. Vaughey, *Chem. Mater.*, 2016, **28**, 17–20.
- 85 F. Sauvage, V. Bodenez, H. Vezin, T. A. Albrecht, J.-M. Tarascon and K. R. Poeppelmeier, *Inorg. Chem.*, 2008, **47**, 8464–8472.
- 86 D. B. Rogers, R. D. Shannon, A. W. Sleight and J. L. Gillson, *Inorg. Chem.*, 1969, **8**, 841–849.
- 87 M. D. Donakowski, A. Görne, J. T. Vaughey and K. R. Poeppelmeier, *J. Am. Chem. Soc.*, 2013, **135**, 9898–9906.
- 88 M. C. Bonatto, G. Ping, Z. K. Zhirong, M. Xiaoke, D. Thomas, P. Maxim, V. S. K. Chakravadhanula, B. R. Juergen and F. Maximilian, *ChemElectroChem*, 2017, **4**, 738–745.
- 89 W. Kaveevivitchai and A. J. Jacobson, *Chem. Mater.*, 2016, **28**, 4593–4601.
- 90 W. Kaveevivitchai and A. J. Jacobson, *Chem. Mater.*, 2013, **25**, 2708–2715.
- 91 M. Sadakane, S. Ohmura, K. Kodato, T. Fujisawa, K. Kato, K.-I. Shimidzu, T. Murayama and W. Ueda, *Chem. Commun.*, 2011, **47**, 10812–10814.
- 92 S. Masahiro, K. Katsunori, K. Takao, N. Yoshinobu, S. Kenji, S. Norihito, N. Takuro, M. Yoshio and U. Wataru, *Angew. Chem., Int. Ed.*, 2008, **47**, 2493–2496.
- 93 A. K. Padhi, K. S. Nanjundaswamy and J. B. Goodenough, *J. Electrochem. Soc.*, 1997, **144**, 1188–1194.
- 94 Z. Gong and Y. Yang, *Energy Environ. Sci.*, 2011, **4**, 3223–3242.
- 95 H. Kim, I. Park, D.-H. Seo, S. Lee, S.-W. Kim, W. J. Kwon, Y.-U. Park, C. S. Kim, S. Jeon and K. Kang, *J. Am. Chem. Soc.*, 2012, **134**, 10369–10372.
- 96 J.-M. Tarascon and M. Armand, *Materials for Sustainable Energy*, Co-Published with Macmillan Publishers Ltd, UK, 2012, pp. 171–179.
- 97 C. Ling, D. Banerjee, W. Song, M. Zhang and M. Matsui, *J. Mater. Chem.*, 2012, **22**, 13517–13523.
- 98 G. K. P. Dathar, D. Sheppard, K. J. Stevenson and G. Henkelman, *Chem. Mater.*, 2011, **23**, 4032–4037.
- 99 D. Morgan, A. Van der Ven and G. Ceder, *Electrochem. Solid-State Lett.*, 2004, **7**, A30–A32.
- 100 R. Zhang and C. Ling, *ACS Appl. Mater. Interfaces*, 2016, **8**, 18018–18026.
- 101 X. Chen, F. L. Bleken, O. M. Løvvik and F. Vullum-Bruer, *J. Power Sources*, 2016, **321**, 76–86.
- 102 Z. Feng, J. Yang, Y. NuLi, J. Wang, X. Wang and Z. Wang, *Electrochem. Commun.*, 2008, **10**, 1291–1294.
- 103 Z. Feng, J. Yang, Y. NuLi and J. Wang, *J. Power Sources*, 2008, **184**, 604–609.
- 104 Y. Zheng, Y. NuLi, Q. Chen, Y. Wang, J. Yang and J. Wang, *Electrochim. Acta*, 2012, **66**, 75–81.
- 105 Y. NuLi, J. Yang, J. Wang and Y. Li, *J. Phys. Chem. C*, 2009, **113**, 12594–12597.
- 106 Y. NuLi, J. Yang, Y. Li and J. Wang, *Chem. Commun.*, 2010, **46**, 3794–3796.
- 107 Y. Li, Y. Nuli, J. Yang, T. Yilinuer and J. Wang, *Chin. Sci. Bull.*, 2011, **56**, 386–390.
- 108 Y. NuLi, Y. Zheng, F. Wang, J. Yang, A. I. Minett, J. Wang and J. Chen, *Electrochem. Commun.*, 2011, **13**, 1143–1146.
- 109 Y. NuLi, Y. Zheng, Y. Wang, J. Yang and J. Wang, *J. Mater. Chem.*, 2011, **21**, 12437–12443.
- 110 Y. Orikasa, T. Masese, Y. Koyama, T. Mori, M. Hattori, K. Yamamoto, T. Okado, Z.-D. Huang, T. Minato, C. Tassel, J. Kim, Y. Kobayashi, T. Abe, H. Kageyama and Y. Uchimoto, *Sci. Rep.*, 2014, **4**, 5622.
- 111 R. Kitaura, F. Iwahori, R. Matsuda, S. Kitagawa, Y. Kubota, M. Takata and T. C. Kobayashi, *Inorg. Chem.*, 2004, **43**, 6522–6524.
- 112 C. K. Anthony, F. Gérard and L. Thierry, *Angew. Chem., Int. Ed.*, 1999, **38**, 3268–3292.
- 113 S. L. Suib, *Annu. Rev. Mater. Sci.*, 1996, **26**, 135–151.
- 114 Z. Yaming, Z. Haoguo, C. Zhenxia, C. Minqin, X. Yan, Z. Haoyu and Z. Dongyuan, *Angew. Chem.*, 2001, **113**, 2224–2226.
- 115 R. Zhang, F. Mizuno and C. Ling, *Chem. Commun.*, 2015, **51**, 1108–1111.
- 116 M. Pasta, C. D. Wessells, N. Liu, J. Nelson, M. T. McDowell, R. A. Huggins, M. F. Toney and Y. Cui, *Nat. Commun.*, 2014, **5**, 3007.
- 117 M. P. Shores, L. G. Beauvais and J. R. Long, *J. Am. Chem. Soc.*, 1999, **121**, 775–779.
- 118 S. Yagi, M. Fukuda, T. Ichitsubo, K. Nitta, M. Mizumaki and E. Matsubara, *J. Electrochem. Soc.*, 2015, **162**, A2356–A2361.
- 119 K. Itaya, I. Uchida and V. D. Neff, *Acc. Chem. Res.*, 1986, **19**, 162–168.
- 120 H. Lee, Y.-I. Kim, J.-K. Park and J. W. Choi, *Chem. Commun.*, 2012, **48**, 8416–8418.
- 121 Y. Mizuno, M. Okubo, E. Hosono, T. Kudo, H. Zhou and K. Oh-ishi, *J. Phys. Chem. C*, 2013, **117**, 10877–10882.
- 122 M. Yutaka, I. Kazuhiro, K. Jungeun and T. Hiroshi, *Appl. Phys. Express*, 2009, **2**, 085001.
- 123 W. Y. Richard, S. Badri, S. H. Kevin, W. J. Nelson, P. Mauro, L. Hyun-Wook, T. F. Michael and C. Yi, *Adv. Energy Mater.*, 2015, **5**, 1401869.
- 124 C. D. Wessells, R. A. Huggins and Y. Cui, *Nat. Commun.*, 2011, **2**, 550.
- 125 Y. Lu, L. Wang, J. Cheng and J. B. Goodenough, *Chem. Commun.*, 2012, **48**, 6544–6546.

- 126 W. Long, L. Yuhao, L. Jue, X. Maowen, C. Jinguang, Z. Dawei and J. B. Goodenough, *Angew. Chem., Int. Ed.*, 2013, **52**, 1964–1967.
- 127 C. D. Wessells, S. V. Peddada, R. A. Huggins and Y. Cui, *Nano Lett.*, 2011, **11**, 5421–5425.
- 128 A. L. Lipson, S.-D. Han, S. Kim, B. Pan, N. Sa, C. Liao, T. T. Fister, A. K. Burrell, J. T. Vaughey and B. J. Ingram, *J. Power Sources*, 2016, **325**, 646–652.
- 129 R. Y. Wang, C. D. Wessells, R. A. Huggins and Y. Cui, *Nano Lett.*, 2013, **13**, 5748–5752.
- 130 Y. Mizuno, M. Okubo, E. Hosono, T. Kudo, K. Oh-ishi, A. Okazawa, N. Kojima, R. Kurono, S.-I. Nishimura and A. Yamada, *J. Mater. Chem. A*, 2013, **1**, 13055–13059.
- 131 F. Wu and G. Yushin, *Energy Environ. Sci.*, 2017, **10**, 435–459.
- 132 R. Malini, U. Uma, T. Sheela, M. Ganesan and N. G. Renganathan, *Ionics*, 2009, **15**, 301–307.
- 133 Y. Seung-Ho, L. S. Hong, L. D. Jun, S. Yung-Eun and H. Taeghwan, *Small*, 2016, **12**, 2146–2172.
- 134 C. Ling, R. Zhang and F. Mizuno, *ACS Appl. Mater. Interfaces*, 2016, **8**, 4508–4515.
- 135 D. A. Kitchaev, S. T. Dacek, W. Sun and G. Ceder, *J. Am. Chem. Soc.*, 2017, **139**, 2672–2681.
- 136 B. Li, G. Rong, Y. Xie, L. Huang and C. Feng, *Inorg. Chem.*, 2006, **45**, 6404–6410.
- 137 J. Dai, S. F. Y. Li, K. S. Siow and Z. Gao, *Electrochim. Acta*, 2000, **45**, 2211–2217.
- 138 C. S. Johnson, M. F. Mansuetto, M. M. Thackeray, Y. Shao-Horn and S. A. Hackney, *J. Electrochem. Soc.*, 1997, **144**, 2279–2283.
- 139 D. A. Tompsett and M. S. Islam, *Chem. Mater.*, 2013, **25**, 2515–2526.
- 140 M. M. Huie, D. C. Bock, E. S. Takeuchi, A. C. Marschilok and K. J. Takeuchi, *Coord. Chem. Rev.*, 2015, **287**, 15–27.
- 141 C. Ling, R. Zhang, T. S. Arthur and F. Mizuno, *Chem. Mater.*, 2015, **27**, 5799–5807.
- 142 R. Zhang, X. Yu, K.-W. Nam, C. Ling, T. S. Arthur, W. Song, A. M. Knapp, S. N. Ehrlich, X.-Q. Yang and M. Matsui, *Electrochem. Commun.*, 2012, **23**, 110–113.
- 143 R. Zhang, T. S. Arthur, C. Ling and F. Mizuno, *J. Power Sources*, 2015, **282**, 630–638.
- 144 S. Rasul, S. Suzuki, S. Yamaguchi and M. Miyayama, *Solid State Ionics*, 2012, **225**, 542–546.
- 145 Y. S. Meng and M. E. Arroyo-de Dompablo, *Energy Environ. Sci.*, 2009, **2**, 589–609.
- 146 S. Rasul, S. Suzuki, S. Yamaguchi and M. Miyayama, *Electrochim. Acta*, 2013, **110**, 247–252.
- 147 J.-Y. Luo, J.-J. Zhang and Y.-Y. Xia, *Chem. Mater.*, 2006, **18**, 5618–5623.
- 148 X. Wang and Y. Li, *J. Am. Chem. Soc.*, 2002, **124**, 2880–2881.
- 149 X. Sun, V. Duffort, B. L. Mehdi, N. D. Browning and L. F. Nazar, *Chem. Mater.*, 2016, **28**, 534–542.
- 150 K. W. Nam, S. Kim, S. Lee, M. Salama, I. Shterenberg, Y. Gofer, J.-S. Kim, E. Yang, C. S. Park, J.-S. Kim, S.-S. Lee, W.-S. Chang, S.-G. Doo, Y. N. Jo, Y. Jung, D. Aurbach and J. W. Choi, *Nano Lett.*, 2015, **15**, 4071–4079.
- 151 N. Balke, S. Jesse, A. N. Morozovska, E. Eliseev, D. W. Chung, Y. Kim, L. Adamczyk, R. E. García, N. Dudney and S. V. Kalinin, *Nat. Nanotechnol.*, 2010, **5**, 749.
- 152 P. Yu, B. N. Popov, J. A. Ritter and R. E. White, *J. Electrochem. Soc.*, 1999, **146**, 8–14.
- 153 K. Xu and A. von Wald Cresce, *J. Mater. Res.*, 2012, **27**, 2327–2341.
- 154 T. Abe, H. Fukuda, Y. Iriyama and Z. Ogumi, *J. Electrochem. Soc.*, 2004, **151**, A1120–A1123.
- 155 V. Duffort, X. Sun and L. F. Nazar, *Chem. Commun.*, 2016, **52**, 12458–12461.
- 156 F. Xiong, Y. Fan, S. Tan, L. Zhou, Y. Xu, C. Pei, Q. An and L. Mai, *Nano Energy*, 2018, **47**, 210–216.
- 157 H. Liu, X. Shi, F. Xu, L. Zhang, W. Zhang, L. Chen, Q. Li, C. Uher, T. Day and G. J. Snyder, *Nat. Mater.*, 2012, **11**, 422.
- 158 M. A. Korzhuev, *Phys. Solid State*, 1998, **40**, 217–219.
- 159 M. K. Balapanov, R. A. Yakshibaev and U. K. Mukhamed'yanov, *Phys. Solid State*, 2003, **45**, 634–638.
- 160 C. Jordi, M. Laure, L. Dominique and P. M. Rosa, *Adv. Mater.*, 2010, **22**, E170–E192.
- 161 R. G. Pearson, *J. Chem. Educ.*, 1968, **45**, 581.
- 162 K. He, Z. Yao, S. Hwang, N. Li, K. Sun, H. Gan, Y. Du, H. Zhang, C. Wolverton and D. Su, *Nano Lett.*, 2017, **17**, 5726–5733.
- 163 Y. Tashiro, K. Taniguchi and H. Miyasaka, *Electrochim. Acta*, 2016, **210**, 655–661.
- 164 R. Zhang, C. Ling and F. Mizuno, *Chem. Commun.*, 2015, **51**, 1487–1490.
- 165 S. Renault, D. Brandell, T. Gustafsson and K. Edstrom, *Chem. Commun.*, 2013, **49**, 1945–1947.
- 166 Z. Song and H. Zhou, *Energy Environ. Sci.*, 2013, **6**, 2280–2301.
- 167 W. Deng, X. Liang, X. Wu, J. Qian, Y. Cao, X. Ai, J. Feng and H. Yang, *Sci. Rep.*, 2013, **3**, 2671.
- 168 L. Yanliang, T. Zhanliang and C. Jun, *Adv. Energy Mater.*, 2012, **2**, 742–769.
- 169 H. Sano, H. Senoh, M. Yao, H. Sakaebe and T. Kiyobayashi, *Chem. Lett.*, 2012, **41**, 1594–1596.
- 170 M. Yao, H. Senoh, S.-I. Yamazaki, Z. Siroma, T. Sakai and K. Yasuda, *J. Power Sources*, 2010, **195**, 8336–8340.
- 171 B. Pan, D. Zhou, J. Huang, L. Zhang, A. K. Burrell, J. T. Vaughey, Z. Zhang and C. Liao, *J. Electrochem. Soc.*, 2016, **163**, A580–A583.
- 172 H. Senoh, H. Sakaebe, H. Sano, M. Yao, K. Kuratani, N. Takeichi and T. Kiyobayashi, *J. Electrochem. Soc.*, 2014, **161**, A1315–A1320.
- 173 P. Baofei, H. Jinhua, F. Zhenxing, Z. Li, H. Meinan, Z. Lu, V. T. John, B. J. Michael, F. Paul, Z. Zhengcheng, B. K. Anthony and L. Chen, *Adv. Energy Mater.*, 2016, **6**, 1600140.
- 174 Z. Song, Y. Qian, X. Liu, T. Zhang, Y. Zhu, H. Yu, M. Otani and H. Zhou, *Energy Environ. Sci.*, 2014, **7**, 4077–4086.
- 175 B. Jan, P. Klemen, B. Tanja, G. Miran, G. Boštjan, R. V. Anna and D. Robert, *ChemSusChem*, 2015, **8**, 4128–4132.
- 176 S. Tepavcevic, Y. Liu, D. Zhou, B. Lai, J. Maser, X. Zuo, H. Chan, P. Král, C. S. Johnson, V. Stamenkovic, N. M. Markovic and T. Rajh, *ACS Nano*, 2015, **9**, 8194–8205.

- 177 S.-C. Lim, J. Lee, H. H. Kwak, J. W. Heo, M. S. Chae, D. Ahn, Y. H. Jang, H. Lee and S.-T. Hong, *Inorg. Chem.*, 2017, **56**, 7668–7678.
- 178 Y. P. Chabre, *J. Electrochem. Soc.*, 1991, **138**, 329–330.
- 179 G. J. Browning and S. W. Donne, *J. Appl. Electrochem.*, 2005, **35**, 871–878.
- 180 C.-X. Zu and H. Li, *Energy Environ. Sci.*, 2011, **4**, 2614–2624.
- 181 Y.-C. Lu, B. M. Gallant, D. G. Kwabi, J. R. Harding, R. R. Mitchell, M. S. Whittingham and Y. Shao-Horn, *Energy Environ. Sci.*, 2013, **6**, 750–768.
- 182 J. G. Smith, J. Naruse, H. Hiramatsu and D. J. Siegel, *Chem. Mater.*, 2016, **28**, 1390–1401.
- 183 J. Lu, J.-B. Park, Y.-K. Sun, F. Wu and K. Amine, *Chem. Rev.*, 2014, **114**, 5611–5640.
- 184 Z. Peng, S. A. Freunberger, Y. Chen and P. G. Bruce, *Science*, 2012, **337**, 563–566.
- 185 G. Girishkumar, B. McCloskey, A. C. Luntz, S. Swanson and W. Wilcke, *J. Phys. Lett.*, 2010, **1**, 2193–2203.
- 186 P. Hartmann, C. L. Bender, M. Vračar, A. K. Dürr, A. Garsuch, J. Janek and P. Adelhelm, *Nat. Mater.*, 2012, **12**, 228.
- 187 B. L. Conrad, H. Pascal, V. Miloš, A. Philipp and J. Jürgen, *Adv. Energy Mater.*, 2014, **4**, 1301863.
- 188 X. Ren and Y. Wu, *J. Am. Chem. Soc.*, 2013, **135**, 2923–2926.
- 189 G. Vardar, E. G. Nelson, J. G. Smith, J. Naruse, H. Hiramatsu, B. M. Bartlett, A. E. S. Sleightholme, D. J. Siegel and C. W. Monroe, *Chem. Mater.*, 2015, **27**, 7564–7568.
- 190 J. Lu, L. Li, J.-B. Park, Y.-K. Sun, F. Wu and K. Amine, *Chem. Rev.*, 2014, **114**, 5611–5640.
- 191 P. G. Bruce, S. A. Freunberger, L. J. Hardwick and J.-M. Tarascon, *Nat. Mater.*, 2011, **11**, 19.
- 192 V. Viswanathan, J. K. Nørskov, A. Speidel, R. Scheffler, S. Gowda and A. C. Luntz, *J. Phys. Lett.*, 2013, **4**, 556–560.
- 193 B. D. McCloskey, J. M. Garcia and A. C. Luntz, *J. Phys. Lett.*, 2014, **5**, 1230–1235.
- 194 T. Shiga, Y. Hase, Y. Kato, M. Inoue and K. Takechi, *Chem. Commun.*, 2013, **49**, 9152–9154.
- 195 T. Shiga, Y. Hase, Y. Yagi, N. Takahashi and K. Takechi, *J. Phys. Lett.*, 2014, **5**, 1648–1652.
- 196 Q. Dong, X. Yao, J. Luo, X. Zhang, H. Hwang and D. Wang, *Chem. Commun.*, 2016, **52**, 13753–13756.
- 197 G. Vardar, J. G. Smith, T. Thompson, K. Inagaki, J. Naruse, H. Hiramatsu, A. E. S. Sleightholme, J. Sakamoto, D. J. Siegel and C. W. Monroe, *Chem. Mater.*, 2016, **28**, 7629–7637.
- 198 T. H. Hwang, D. S. Jung, J.-S. Kim, B. G. Kim and J. W. Choi, *Nano Lett.*, 2013, **13**, 4532–4538.
- 199 E. Ran, S. Gregory, G. Arnd, P. Alexander and A. Doron, *Adv. Mater.*, 2011, **23**, 5641–5644.
- 200 X. Ji, K. T. Lee and L. F. Nazar, *Nat. Mater.*, 2009, **8**, 500.
- 201 X. Sen, Y. Ya-Xia, G. Yu-Guo and W. Li-Jun, *Adv. Mater.*, 2014, **26**, 1261–1265.
- 202 T. Gao, M. Noked, A. J. Pearse, E. Gillette, X. Fan, Y. Zhu, C. Luo, L. Suo, M. A. Schroeder, K. Xu, S. B. Lee, G. W. Rubloff and C. Wang, *J. Am. Chem. Soc.*, 2015, **137**, 12388–12393.
- 203 A. Du, Z. Zhang, H. Qu, Z. Cui, L. Qiao, L. Wang, J. Chai, T. Lu, S. Dong, T. Dong, H. Xu, X. Zhou and G. Cui, *Energy Environ. Sci.*, 2017, **10**, 2616–2625.
- 204 Y. Diao, K. Xie, S. Xiong and X. Hong, *J. Power Sources*, 2013, **235**, 181–186.
- 205 C. Barchasz, J.-C. Leprêtre, F. Alloin and S. Patoux, *J. Power Sources*, 2012, **199**, 322–330.
- 206 Z. K. Zhirong, Z. Xiangyu, W. Di, D. Thomas, B. R. Jürgen and F. Maximilian, *Adv. Energy Mater.*, 2015, **5**, 1401155.
- 207 G. Tao, J. Xiao, H. Singyuk, F. Xiulin, L. Xiaogang, Y. Chongying, H. Fudong, W. Fei, J. Jianjun, X. Kang and W. Chunsheng, *Adv. Mater.*, 2018, **30**, 1704313.
- 208 H. S. Kim, T. S. Arthur, G. D. Allred, J. Zajicek, J. G. Newman, A. E. Rodnyansky, A. G. Oliver, W. C. Boggess and J. Muldoon, *Nat. Commun.*, 2011, **2**, 427.
- 209 L. Wanfei, C. Shuang, W. Jian, Q. Yongcai, Z. Zhaozhao, L. Hongzhen, N. Sanjay, M. Qian, X. Yan, Y. Fangmin, L. Meinan, Z. Lisha and Z. Yuegang, *Angew. Chem., Int. Ed.*, 2016, **55**, 6406–6410.
- 210 G. Tao, H. Singyuk, W. Fei, M. Zhaohui, L. Xiaogang, X. Kang and W. Chunsheng, *Angew. Chem., Int. Ed.*, 2017, **56**, 13526–13530.
- 211 X. Yu and A. Manthiram, *ACS Energy Lett.*, 2016, **1**, 431–437.
- 212 B. P. Vinayan, Z. Zhao-Karger, T. Diemant, V. S. K. Chakravadhanula, N. I. Schwarzburger, M. A. Cambaz, R. J. Behm, C. Kubel and M. Fichtner, *Nanoscale*, 2016, **8**, 3296–3306.
- 213 T. Gao, S. Hou, K. Huynh, F. Wang, N. Eidson, X. Fan, F. Han, C. Luo, M. Mao, X. Li and C. Wang, *ACS Appl. Mater. Interfaces*, 2018, **10**, 14767–14776.
- 214 S.-B. Son, T. Gao, S. P. Harvey, K. X. Steirer, A. Stokes, A. Norman, C. Wang, A. Cresce, K. Xu and C. Ban, *Nat. Chem.*, 2018, **10**, 532–539.
- 215 H. Tian, T. Gao, X. Li, X. Wang, C. Luo, X. Fan, C. Yang, L. Suo, Z. Ma, W. Han and C. Wang, *Nat. Commun.*, 2017, **8**, 14083.
- 216 G. Tao, H. Fudong, Z. Yujie, S. Liumin, L. Chao, X. Kang and W. Chunsheng, *Adv. Energy Mater.*, 2015, **5**, 1401507.
- 217 Y. Cheng, H. J. Chang, H. Dong, D. Choi, V. L. Sprenkle, J. Liu, Y. Yao and G. Li, *J. Mater. Res.*, 2016, **31**, 3125–3141.
- 218 S. Yagi, T. Ichitsubo, Y. Shirai, S. Yanai, T. Doi, K. Murase and E. Matsubara, *J. Mater. Chem. A*, 2014, **2**, 1144–1149.
- 219 W. Na, Y. Zhen-Zhong, Y. Hu-Rong, Y. Ya-Xia, G. Lin and G. Yu-Guo, *Angew. Chem., Int. Ed.*, 2015, **54**, 5757–5761.
- 220 Z. Ye, X. Junjie, H. Yanlin and L. Chilin, *Adv. Funct. Mater.*, 2015, **25**, 7300–7308.
- 221 H. D. Yoo, Y. Liang, Y. Li and Y. Yao, *ACS Appl. Mater. Interfaces*, 2015, **7**, 7001–7007.
- 222 Q. Miao, Y. NuLi, N. Wang, J. Yang, J. Wang and S.-I. Hirano, *RSC Adv.*, 2016, **6**, 3231–3234.
- 223 S. Su, Y. NuLi, Z. Huang, Q. Miao, J. Yang and J. Wang, *ACS Appl. Mater. Interfaces*, 2016, **8**, 7111–7117.
- 224 S. Xiaoqi, D. Victor and N. F. Linda, *Adv. Sci.*, 2016, **3**, 1600044.
- 225 A. Byeon, M.-Q. Zhao, C. E. Ren, J. Halim, S. Kota, P. Urbankowski, B. Anasori, M. W. Barsoum and Y. Gogotsi, *ACS Appl. Mater. Interfaces*, 2017, **9**, 4296–4300.

- 226 Y. Meng, D. Wang, Y. Wei, K. Zhu, Y. Zhao, X. Bian, F. Du, B. Liu, Y. Gao and G. Chen, *J. Power Sources*, 2017, **346**, 134–142.
- 227 C. Pei, F. Xiong, J. Sheng, Y. Yin, S. Tan, D. Wang, C. Han, Q. An and L. Mai, *ACS Appl. Mater. Interfaces*, 2017, **9**, 17060–17066.
- 228 F. Xin, G. R. Ranganathan, K. N. Ashok and Z. X. Song, *Adv. Energy Mater.*, 2017, **7**, 1700317.
- 229 Y. Cheng, Y. Shao, J.-G. Zhang, V. L. Sprenkle, J. Liu and G. Li, *Chem. Commun.*, 2014, **50**, 9644–9646.
- 230 J. Zheng, W. Deng, Z. Hu, Z. Zhuo, F. Liu, H. Chen, Y. Lin, W. Yang, K. Amine, R. Li, J. Lu and F. Pan, *ACS Energy Letters*, 2018, **3**, 65–71.
- 231 M. Cabello, R. Alcántara, F. Nacimiento, P. Lavela, M. J. Aragón and J. L. Tirado, *Electrochim. Acta*, 2017, **246**, 908–913.
- 232 Y. Li, Q. An, Y. Cheng, Y. Liang, Y. Ren, C.-J. Sun, H. Dong, Z. Tang, G. Li and Y. Yao, *Nano Energy*, 2017, **34**, 188–194.
- 233 X. Bian, Y. Gao, Q. Fu, S. Indris, Y. Ju, Y. Meng, F. Du, N. Bramnik, H. Ehrenberg and Y. Wei, *J. Mater. Chem. A*, 2017, **5**, 600–608.
- 234 H. Dong, Y. Li, Y. Liang, G. Li, C.-J. Sun, Y. Ren, Y. Lu and Y. Yao, *Chem. Commun.*, 2016, **52**, 8263–8266.
- 235 M. Walter, K. V. Kravchyk, M. Ibáñez and M. V. Kovalenko, *Chem. Mater.*, 2015, **27**, 7452–7458.
- 236 M. Cabello, F. Nacimiento, R. Alcántara, P. Lavela, G. Ortiz and J. L. Tirado, *J. Electrochem. Soc.*, 2016, **163**, A2781–A2790.
- 237 J.-H. Cho, M. Aykol, S. Kim, J.-H. Ha, C. Wolverton, K. Y. Chung, K.-B. Kim and B.-W. Cho, *J. Am. Chem. Soc.*, 2014, **136**, 16116–16119.
- 238 Y. Gofer, O. Chusid, H. Gizbar, Y. Viestfrid, H. E. Gottlieb, V. Marks and D. Aurbach, *Electrochem. Solid-State Lett.*, 2006, **9**, A257–A260.